Title
Receiver Functions and Tomography Study along the Monterey Micro-Plate and Isabella Anomaly

Author
Cox, Paul Aiken

Publication Date
2013

Peer reviewed|Thesis/dissertation

UNIVERSITY OF CALIFORNIA

Los Angeles

Receiver Functions and Tomography Study along the Monterey Micro-Plate and Isabella Anomaly

A thesis submitted in partial satisfaction

of the requirements for the degree Master of Science

in Geophysics and Space Physics

by

Paul Aiken Cox

2013

ABSTRACT OF THE THESIS

Receiver Functions and Tomography Study along the Monterey Micro-Plate and Isabella Anomaly

by

Paul Aiken Cox

Master of Science in Geophysics and Space Physics

University of California, Los Angeles, 2013

Professor Paul M. Davis, Chair

Two hypotheses on the origin of the ‘Isabella tomographic anomaly,’ which has been interpreted as either a lithospheric delamination (Ducea and Saleeby, 1998) or a remnant of the Farallon plate attached to the Monterey micro-plate (Wang et al., 2013), were tested. P-wave receiver functions and tomography based on teleseismic events recorded by 37 permanent stations

and 4 newly installed stations were used to construct a simple geometry tomographic model of the Isabella anomaly, and to test whether the Monterey micro-plate can be connected with the location of the Isabella anomaly. A rectangular block model was used to fit the arrival-time residual pattern, and the best-fit model has its top surface located at 50km below the Great Valley. The block model dips 65º toward the Sierra Nevada with 100 km thickness. Receiver functions suggest that the remnant Farallon plate is not stalled at the base of the crust beneath the Coast Ranges as has been suggested from refraction studies (Brocher et al., 1999). Instead, the Monterey micro-plate lies in the mantle. Its top and bottom surfaces can be observed as a negative-positive dipole signal in the receiver functions. Negative-positive dipole signals at 35 km observed in the Coast Ranges' receiver functions were interpreted as the P-to-S converted phases from the Monterey micro-plate. These P-to-S converted phases from the top of the oceanic crust could be traced from the Coast Ranges to the Great Valley. The depth of the top surface of the Monterey micro-plate suggested from the receiver functions is consistent with the location of the rectangular block found from tomography, supporting the hypothesis that the Isabella anomaly is a remnant of the

Farallon plate that is attached to the Monterey micro-plate. The combined results of the receiver functions and tomography study suggest that the partially subducted Monterey micro-plate extends east beyond the San Andreas fault and that the initially low angle of subduction in the west increases its dip east below the Great Valley.

The thesis of Paul Aiken Cox is approved.

Caroline Beghein

Raymond Ingersoll

Paul M. Davis, Committee Chair

University of California, Los Angeles

2013

Table of contents

List of Figures

List of Tables

Chapter1; Introduction

Isabella Anomaly

Seismology has long been the strongest tool to reveal the interior of Earth. Significant increase in seismic networks in the 1970's has led to the development of large-scale tomography studies to understand the physical processes in the lithosphere and asthenosphere (Aki, 1982). As many geographic and geologic features can be explained in terms of plate tectonics, many features in the lithosphere and asthenosphere can be tied into the theory of plate tectonics. An example from earlier studies in the western United States is the high-velocity anomaly from the subducted Farallon plate and the low-velocity anomaly from the 'slab window' above the Farallon plate (Romanowicz, 1980), as described by Dickinson and Snyder (1979). However, a high-velocity anomaly observed by a seismic station ISA near Lake Isabella in California (Raikes, 1975) had no obvious connection with any topographic feature or geologic event, and it was not explained by simple plate tectonic theory.

This high-velocity anomaly, often described as the 'Isabella anomaly', also called the southern Central Valley anomaly, the southern Great Valley

anomaly, or the south Sierra Nevada anomaly e.g., (Aki, 1982; Biasi and Humphreys, 1992; Zandt, 2003; Boyd et al., 2004; Yang and Forsyth, 2006; Schmandt and Humphreys, 2010; Obrebski et al., 2011), is located at 36.5ºN, 119.5ºW under the southern Great Valley and the southern Sierra Nevada (Wang et al., 2013) (figure 1.1).

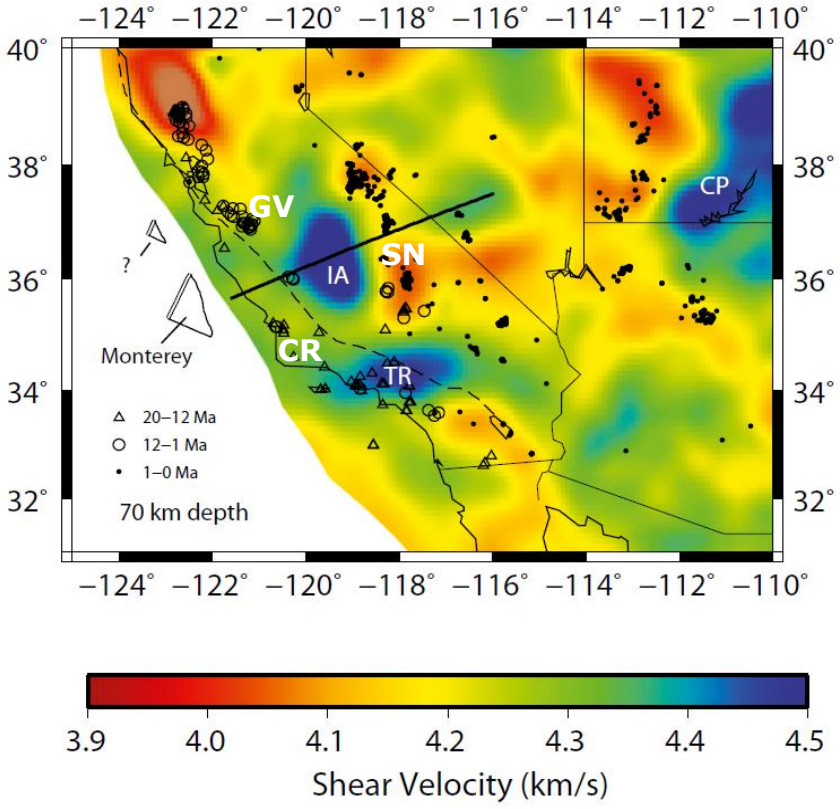

Figure 1.1: S-wave velocity anomalies in the southwestern United States at 70 km depth. IA, Isabella Anomaly; CP, Colorado Plateau; TR, Transverse Range; GV, Great Valley; SN, Sierra Nevada; CR, Coast Ranges. The small symbols indicate volcanic activity in different age ranges, but only the youngest activity is shown except near the coast. The dashed line is the San Andreas fault. From Wang et al. (2013).

Raikes (1976) discovered the anomaly as a negative (i.e., early) teleseismic P-wave residual region with -0.9 sec residual time. It was modeled as a 4 to 5% compressional velocity anomaly extending from about 100 to 200 km depth from teleseismic P-wave arrival-time inversion (Jones et al., 1994). Surface wave inversion has revealed that it is associated with a lateral velocity contrast in shear velocity at 100 km depth on the order of 6% (Wang et al., 2013). Observation of the Isabella anomaly has led to its interpretation as a drip (Jones et al., 1994) or delamination (Ducea and Saleeby, 1998) of continental lithosphere beneath the Sierra Nevada, or as a fossil slab detached from the Farallon plate (Wang et al., 2013).

Since the high-velocity anomaly in deeper structure beneath the Sierra Nevada could not be explained by simple plate tectonics, Aki (1982) interpreted the Isabella anomaly as a decoupling between the upper brittle lithosphere and the ductile substratum. The interpretation was developed to answer several questions that arose in the Sierra Nevada. One question that has been asked for a long time is what is the cause of the uplift in a region without any compressive tectonism. Over 2 km uplift relative to sea level is inferred (Huber, 1981) in regions of the Sierra Nevada without contractional

strain or large-scale volcanism, but with regional tensile stress (Lockwood and Moore, 1979). Moreover, regional Pn-wave arrival-times show Moho depth beneath the southern high Sierra to be of normal thickness of about 33 km (Jones et al., 1994), indicating there is no crustal root. Jones et al. (1994) explained the uplift and the absence of a deep crustal root by buoyant low-velocity mantle, and interpreted the Isabella anomaly as a mantle drip that caused the thinning of the mantle lithosphere and rising of the asthenosphere beneath the Sierra Nevada. Ducea and Saleeby (1998) inferred the composition of the lithosphere beneath the Sierra Nevada using deep-crustal and upper-mantle xenoliths, concluding that any crustal root that may have been present by 12 to 8 Ma has been removed, and interpreted the Isabella anomaly to be a delaminated crustal root.

In contrast, Wang et al. (2013) interpreted the anomaly as a remnant of the Farallon plate, which became attached to the Pacific plate. Since soon after 30 Ma, the long lasting Farallon-North America subduction system has been converting to the Pacific-North America transform system. Within this transition process, a ‘slab window’ has formed (Dickinson and Snyder, 1979), but detailed study of offshore magnetic anomaly patterns has revealed that

some fragments of the Farallon plate have been captured by the Pacific plate (Lonsdale, 1991; Nicholson et al., 1994). Although there is an argument that a 'slab gap' is required beneath the Coast Ranges to explain the high heat flow (Dickinson, 1997), several seismic studies have shown that the Monterey micro-plate can be traced landward from the former deformation front to at least the San Andreas fault (Brocher et al., 1999; Miller et al., 1992; ten Brink et al., 1999), and that the slab has stalled. Wang et al. (2013) argued that the slab may extend east beyond the San Andreas fault boundary, connecting to the Isabella anomaly.

The stalled slab model would be supported if we can trace the Monterey micro-plate across to the Isabella anomaly. It might then explain both the cause of the rotation of the western Transverse Ranges (Nicholson et al., 1994), and the source of water into the aseismic creeping section of the San Andreas fault near Parkfield (Pikser et al., 2012). The key to truly understand the origin of the Isabella anomaly is a more detailed study of the geometry of the anomaly, but there is a limitation as to how well the anomaly can be projected through tomography. Receiver functions, an excellent tool to complement seismic tomography, have good lateral resolution but poor

vertical resolution, and can provide information about the location of material boundaries. In 2012, new seismic stations were installed by the UCLA FlexiRamp project along the line of projection from the Monterey micro-plate to the Isabella anomaly, beginning near San Luis Obispo, through Parkfield to Fresno. In this paper, I provide additional insights, using receiver functions obtained from our four FlexiRamp stations and 37 permanent stations, as to whether the Monterey plate can be traced to the Isabella anomaly.

Geologic/Tectonic Setting

The study area includes three geographic features: the Coast Ranges, the Great Valley, and the Sierra Nevada (figure 1.1). Each of the geographic features is a result of long and complicated tectonic processes, some of which are described in figure 1.2. A good understanding of crustal structure is necessary to investigate receiver function interpretation of sub-crustal structure.

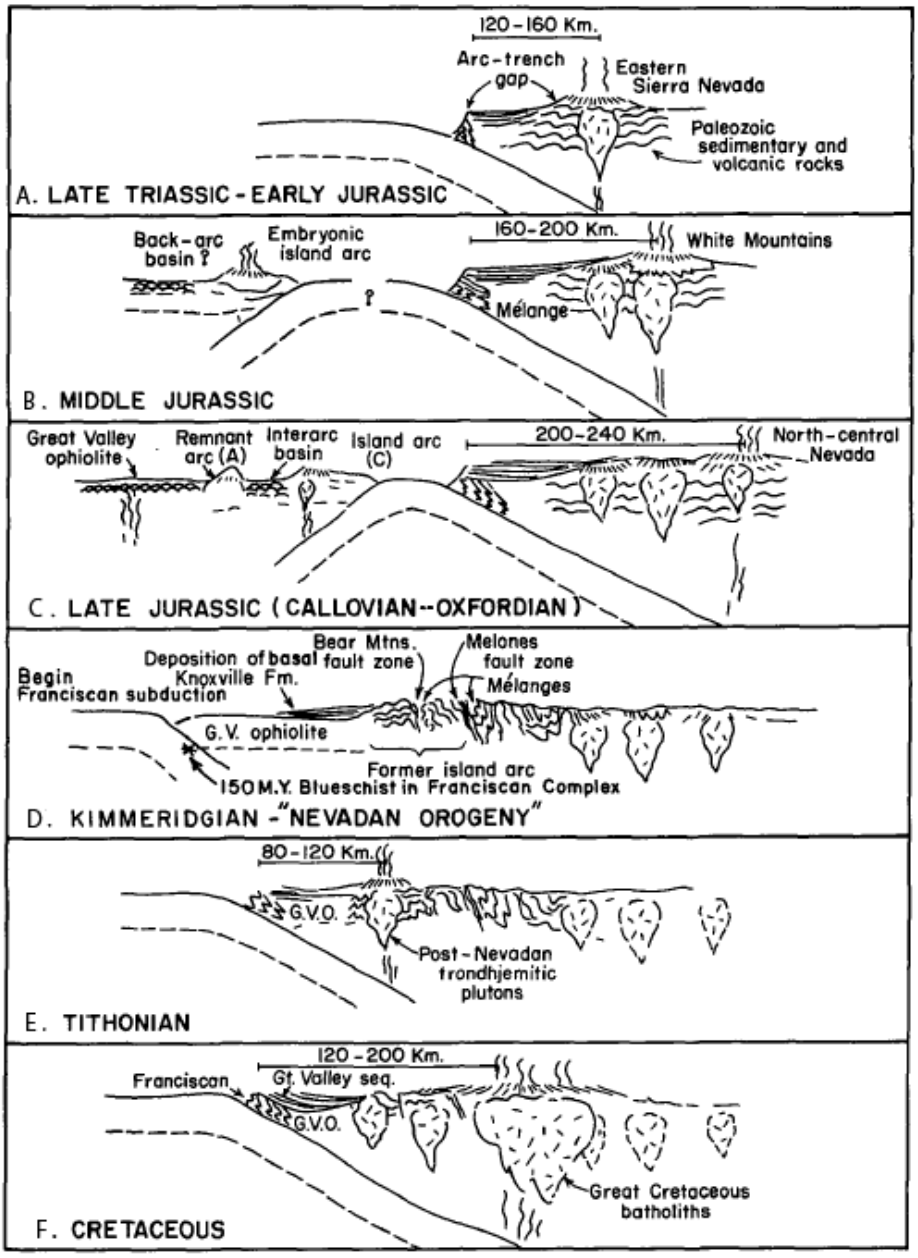

Figure 1.2: Hypothetical schematic sections showing postulated tectonic evolution of the Sierra Nevada region during Mesozoic time. G.V.O, Great Valley ophiolite. From Schweickert and Cowan (1975).

During Late Triassic time, an oceanic lithosphere plate started to subduct beneath the western edge of the North American plate (Schweickert

and Cowan, 1975) (figure 1.2(A)). Farther to the west, the oceanic lithosphere was consumed by west-dipping subduction, developing an oceanic island arc during Middle Jurassic time (Schweickert and Cowan, 1975), and the Great Valley ophiolite formed at this time from backarc spreading (figure 1.2(B)). As the oceanic island arc moved to the east, the Smartville ophiolite formed by interarc spreading (figure 1.2(C)) in Late Jurassic time (Dickinson et al., 1996).

The two opposing arc-trench systems collided face to face (figure 1.1(D)) approximately 150 Ma (Schweickert and Cowan, 1975). The Smartville ophiolite, deformed in the collision, is found in the northwestern Sierra Nevada as Jurassic meta volcanic and plutonic rocks (Beard and Day, 1987). At the same time, the Great Valley ophiolite was trapped behind the Smartville ophiolite as subduction stepped westward and Franciscan subduction initiated (figure 1.2(E)) to form a new forearc system (Ingersoll, 1982). As the Great Valley ophiolite was trapped between the new Sierran arc and the new west-facing Franciscan subduction zone, a forearc basin developed over the Great Valley ophiolite (figure 1.2(F)).

Subduction continued through the Late Jurassic to the Tertiary (Page,

1981). Offscraped and underplated trench-fill sediments, which accumulated as the Franciscan subduction complex, include blueschist representing high-pressure/low-temperature metamorphism (Ernst et al., 1970), west of the Great Valley forearc basin (Dickinson, 1970; Ingersoll, 1982). As the Farallon plate was consumed, part of the ancestral East Pacific Rise encountered North America beginning in the late Oligocene (Atwater and Molnar, 1973). The continental margin became a transform plate boundary as the two migrating triple junctions separated and the San Andreas transform plate boundary lengthened (Atwater, 1970). In the following chapters, I relate the seismic signals to these tectonic structures.

Chapter2; Receiver Functions

Introduction

Detailed information of crustal and upper-mantle material properties and their depth variation is essential for understanding lithospheric evolution. It is also critical for accurately locating earthquakes and to further understand the earthquake mechanism. Receiver functions, which combine reflection and refraction methods, have been developed over decades as a powerful tool to determine Moho depth and characteristics of material boundaries.

Phinney (1964) proposed that the ratio of vertical to horizontal component spectra from teleseismic P-waves depends on structure beneath the station, and used power spectrum analysis to identify the base of the crust. Burdick and Langston (1977) performed a similar analysis in the time-domain, identifying teleseismic P wave scattered phases to construct crustal models. Langston (1979) further investigated time-domain receiver functions in which direct P-wave arrival and the P-to-S conversion and reverberation are extracted sequentially. Times and amplitudes of each phase can then be examined (Langston 1979).

Compared with some other methods, the advantage in using receiver

functions to find discontinuity is sensitivity to material velocity change in the vertical direction. For example, wide-angle reflection and refraction methods, such as PmP and Pn waves travel-time studies, have been employed to locate the Moho, but the waves usually travel more than 100 km laterally within the crust. Uncertainty from lateral variation in crustal thickness then becomes a problem (Zhu and Kanamori, 2000). In contrast, receiver functions use near-vertical incoming waves, and are sensitive to depth variation directly beneath a station, making receiver functions a more reliable tool for finding such a discontinuity. Surface wave dispersion is another useful tool to analyze depth variation in velocity structure; long-period waves are used to study deep into mantle. But at the same time, the long-period nature of the surface wave limits resolution to accurately locate the discontinuity compared with the high resolution of receiver functions (Kind et al., 1995).

Another advantage in using receiver functions is that the waveform does not need to be estimated. Seismograms can be decomposed into source time function, instrument response, and near receiver effects. Receiver functions are used to extract the near receiver effect. Since the receiver function method uses vertical and horizontal component seismograms from

the same phase in the same event recorded by a single station for comparison, the source time function and instrument response cancel out. This simplicity is the main advantage of receiver functions.

Receiver functions have been used in many studies, including identifying depth of the Moho (e.g., Zhu and Kanamori, 2000; Yan and Clayton, 2007b), the lithosphere-asthenosphere boundary (e.g., Rychert and Shearer, 2009; Abt et al., 2010), and mantle transition zones at 410 km and 660 km (e.g., Gurrola et al., 1994). Receiver functions are also used to study geometric properties at boundaries such as dip and steps in the Moho (e.g., Yan and Clayton, 2007a), or crustal material properties, such as crustal anisotropy (e.g., Ozacar and Zandt, 2009) and Poisson's ratio (e.g., Zandt and Ammon, 1995).

Definition of Receiver Functions

A teleseismic body wave recorded on a seismogram consists of the original source function plus P-to-S converted reverberation from near surface Earth structures. Receiver functions can be obtained by isolating this seismic response of the local Earth structure beneath the seismic station from the

source effect using the deconvolution technique (Langston, 1979). Consider a case where seismic body waves consist of a direct P wave and reverberations between a free surface and an interface *h* as shown in figure 2.1, and let *Z(t)* and *R(t)* represent the vertical and radial components of motion, respectively.

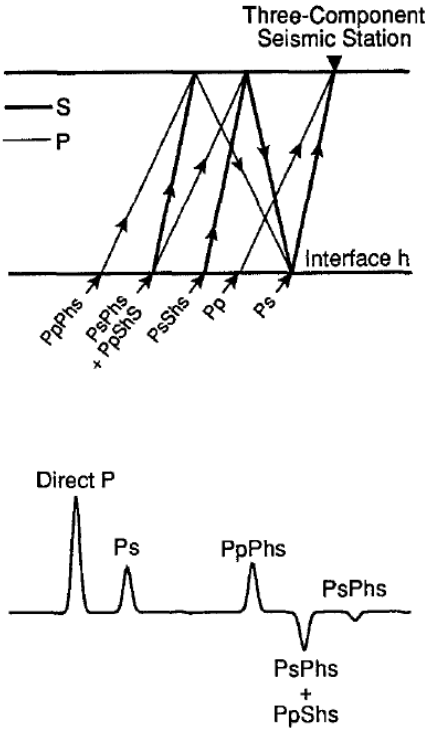

Figure 2.1: Receiver function ray diagram. (Top) Simplified ray diagram showing the major P-to-S converted phases that comprise the radial receiver function for a layer over a half-space. (Bottom) The waveform corresponding to the diagram above. Except for the first arrival, upper-case letters denote upgoing travel paths, lower-case letters denote downgoing travel paths, and h indicates reflection from the interface. From Amon (1991).

Because of the steep angle of the incoming ray, most of the energy from the direct P wave will be recorded in *Z(t)*, and P-to-S converted reverberation

from near surface Earth structure response in *R(t)*. Thus, the receiver function, *H(t)*, can be related to the radial and vertical components of motion through

$$\mathrm{R(t)} = Z(t) * H(t), \qquad (2.1)$$

where [*] represents the convolution operation. Therefore, the receiver function can be obtained by deconvolution of the vertical component from radial component motion. In the case of a homogeneous horizontal layer, the P wave can only be converted to an SV wave (vertically polarized shear wave), and will be seen in the radial component. However, the SH wave (horizontally polarized shear wave) can be recorded in the tangential component if the layer is dipping or if the layer is anisotropic. The tangential receiver function can be calculated similarly by deconvolution of the vertical component of motion from the tangential component of motion.

Deconvolution

Convolution and deconvolution operations in the frequency-domain are simply multiplication and division, respectively. After transforming *V(t)*, *R(t)* and *H(t)*

into the frequency-domain via Fourier transform, the above convolution equation becomes

$$R(w) = Z(w)H(w), \qquad (2.2)$$

and solving for the receiver functions,

$$H(w) = R(w)/Z(w). \qquad (2.3)$$

However, the deconvolution procedure is numerically unstable because signals are band-limited and contain random noise (Langston, 1979). In order to stabilize the deconvolution and to estimate the receiver functions, many methods have been developed in the last few decades, including time-domain and frequency-domain deconvolution.

Water-level deconvolution (Clayton and Wiggins, 1976) and the multitaper correlation method (Park and Levin, 2000) are examples of the frequency-domain deconvolution method. Simultaneous time-domain deconvolution (Gurrola et al., 1995) and iterative deconvolution (Ligorria and

Ammon, 1999) are examples of the time-domain deconvolution method. Deconvolution performed by spectral division becomes unstable because values in the denominator near zero value due to noise can dominate the solution. Waterlevel deconvolution deals with this issue by eliminating the low-signal portion of the seismogram by adding a constant parameter, called the waterlevel (Clayton and Wiggins, 1976). The waterlevel then becomes the minimum source amplitude, and it stabilizes the spectral division by replacing any data below the limit by the parameter. In contrast, multitaper correlation avoids numerical instabilities in spectral division by applying a filter that minimizes spectral leakage. By applying orthogonal tapers described in Thomson (1982), the multitaper method makes the spectrum smooth to down-weight the noisy portions of the spectrum.

An alternative method carries out the deconvolution in the time-domain. Gurrola et al. (1995) solve for *H(t)* by matrix inversion with an assumption that the subtraction of receiver functions and the pre-event noise from the deconvolution of the vertical and radial components results in zero amplitude. However, similar to the waterlevel method in the frequency-domain deconvolution, a stabilizing parameter called the Lagrange

multiplier μ^{-1} needs to be applied. The Lagrange multiplier weights the assumption to stabilize the solution. Iterative deconvolution, on the other hand, uses a correlation method discussed by Kikuchi and Kanamori (1982) to fit the vertical component waveform contained in the radial component seismogram to iteratively construct the time-impulse function. In each iteration, the amplitude of the vertical component waveform at the time delay calculated from the correlation method that best-fits the radial component is subtracted from the radial component. The iteration continues using the residual radial component until the misfit between the vertical component seismogram convolved with the estimated receiver functions and the radial components is insignificant.

Comparing the different deconvolution techniques, the greatest difficulty is choosing the right stabilizing factor. Depending on the selected stabilizing factors, deconvolution produces oscillatory artifact noise, making the interpretation difficult. Gurrola et al. (1995) used misfit between *V(t)*H(t)* and *R(t)* to select the best stabilizing factor; however, the *V(t)*H(t)* is invariant with respect to the oscillatory artifact noise, and the method did not solve the problem. Iterative deconvolution, on the other hand, does not need

the stabilizing factor. I found that the iterative deconvolution method was robust and calculated the cleanest receiver functions. The iterative deconvolution method is used as the main deconvolution method in this study, except for some basin stations where the waterlevel deconvolution method was easier to adjust the receiver function to reveal near surface complications.

Interpretation

A receiver function is a time-series representation of the incident P-wave, P-to-S conversions and reverberations at their arrival-times. Time and amplitude of each signal in the receiver function carry information about the subsurface structures, and the structures can be interpreted by accurate identification of the signals and by tracing of the ray path.

Figure 2.2(a) shows a simple model with 30 km thick single-layer crust. As a convention, the vertical component is directed vertically upward and the radial component is directed perpendicular to the vertical axis along the great circle connecting the epicenter and seismometer, with positive direction away from the epicenter. In figure 2.2(a), the vertical component is directed upward

and the radial component is directed to the right. When the teleseismic P-wave hits the station, the vertical component records most of the energy, but the radial component also records parts of the first arrival P-wave because of slight non-verticality of the incident ray. Figure 2.2(c) shows a synthetic seismogram that I calculated from the model; the first arrival energy can be seen in both vertical and radial component. Since the vertical component and radial component seismograms are recording the same signal, there is no time lag between the components. This common energy in the two components makes the 0 sec peak in the receiver function.

(a) (b)

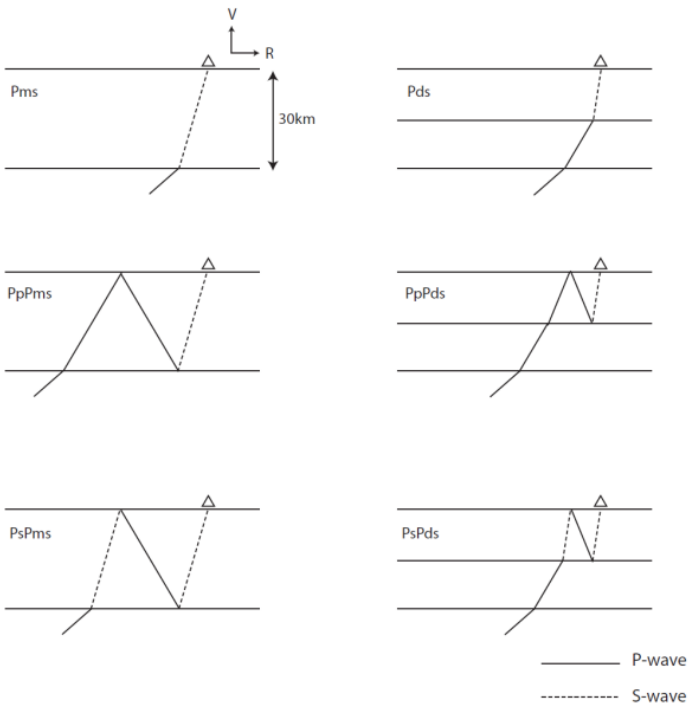

(c)

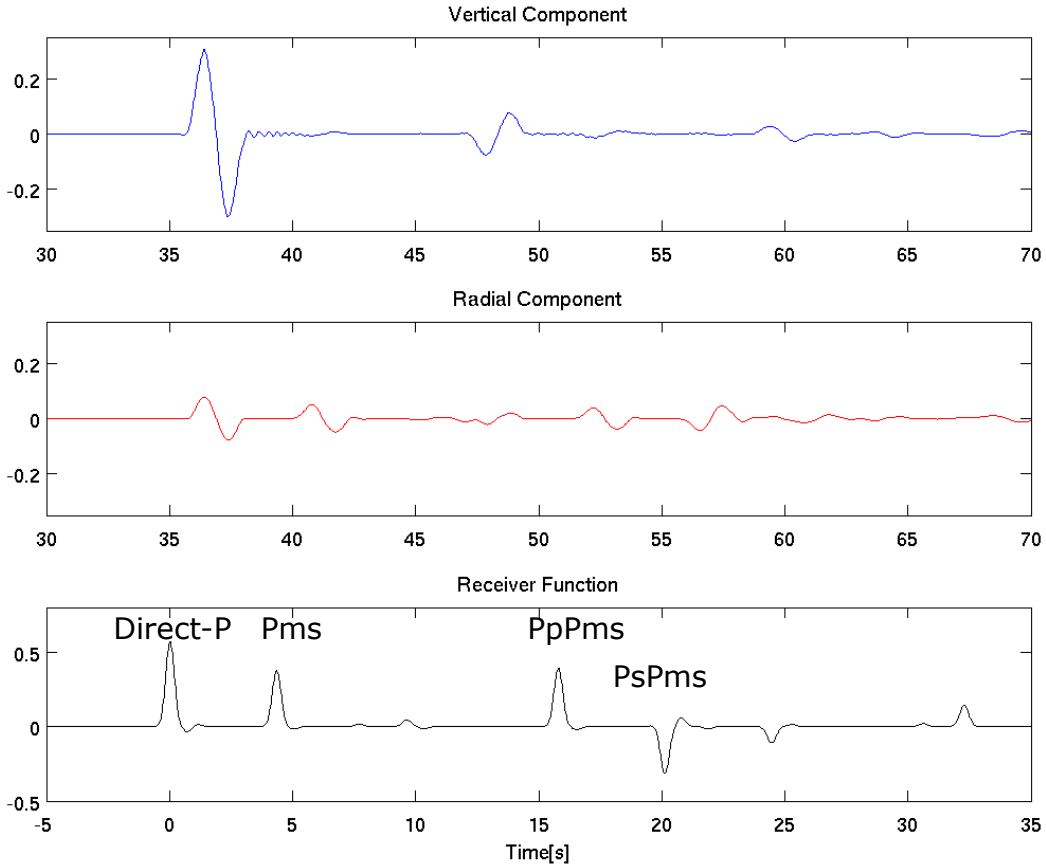

Figure 2.2: (a) Receiver function ray diagrams for a simple model with 30 km thick crustal layer over mantle. (b) Receiver function ray diagrams for two-layer crustal model over mantle. (c) Synthetic seismogram from the model in (a) for vertical component (top) and radial component (middle). The bottom plot shows a receiver function calculated from the synthetic seismogram.

The second ray that arrives at the receiver is a P-to-S converted phase from the mantle-crust boundary (Pms). At time,

$$t_{Ps} = \mathrm{h}(\sqrt{V_s^{-2} - p^2} - \sqrt{V_p^{-2} - p^2}), \qquad (2.4)$$

after the direct P-wave arrival, the Pms ray will arrive at the receiver, where *h* is the crustal thickness, *Vp* and *Vs* are the P-wave and S-wave velocities in the crust, respectively, and *p* is the ray parameter. The P-to-S converted phase can be seen as the second largest signal at time 4.4 sec in the receiver function. Signals in the receiver function following the Pms arrival are the multiples generated within the crust: PpPms and PpSms+PsPms.

Equation 2.4 can be solved for *h* if *tPs*, *p*, *Vp* and *Vp/Vs* ratio are known. *tPs* can be obtained from observing the receiver functions and the incidence angles can be calculated from the ray parameters. The receiver function is fairly insensitive to the *Vp* value, and an average crustal velocity from a study region is often used (Zhu and Kanamori, 2000). The average *Vp/Vs* ratio can be calculated by considering the arrival-time between Pms, PpPms and PpSms+PsPms phases (figure 2.2(a)). Therefore, the Moho depth can be inverted by accurately distinguishing each of the phases in the receiver functions.

In more complicated cases, upper-crust/lower-crust boundary or

low-velocity basins, can add extra signals (figure 2.2(b)), making the interpretation more difficult. Moreover, dipping interfaces or anisotropic material can transmit some of the energy as SH waves in tangential components. In the case where tangential component energy is present, dipping or anisotropic structure can be modeled by examining the azimuthal variation of the radial and tangential receiver functions (Ozacar and Zandt, 2009). Complex geologic structure requires more detailed modeling of the crust; however, accurately recognizing each of the phases created within the crust allows discovery of deeper interfaces beneath the crust.

Chapter3; Crustal Structure from Receiver Functions

Data Collection

Figure 3.1 shows the location of 37 permanent stations and 4 temporary stations used in this study. The permanent stations include the stations from the California Integrated Seismic Network (CI), the Berkeley Digital Seismograph Network (BK) and the Plate Boundary Observatory Borehole Seismic Network (PB). The 4 temporary stations are from the UCLA FlexiRamp project (GC) where they are installed along the projection of Monterey micro-plate to the Isabella anomaly. Teleseismic P-waves from a distance range 30º to 90º and teleseismic PP-waves from a distance range 60º to 160º from earthquakes with magnitude larger than 6.0 were selected from the earthquake catalog between January 2001 and January 2013 (table 3.1). The records were time windowed to 120 sec, starting 20 sec before and 100 sec after the P-wave arrival. A 0.1 to 1.0 Hz band-pass filter was applied, and the waveforms with signal-to-noise ratios higher than 3 determined by the STA/LTA method (Earle and Shearer, 1994) were used to calculate receiver functions. North component and east component seismograms were then

rotated to radial and tangential directions according to back azimuth.

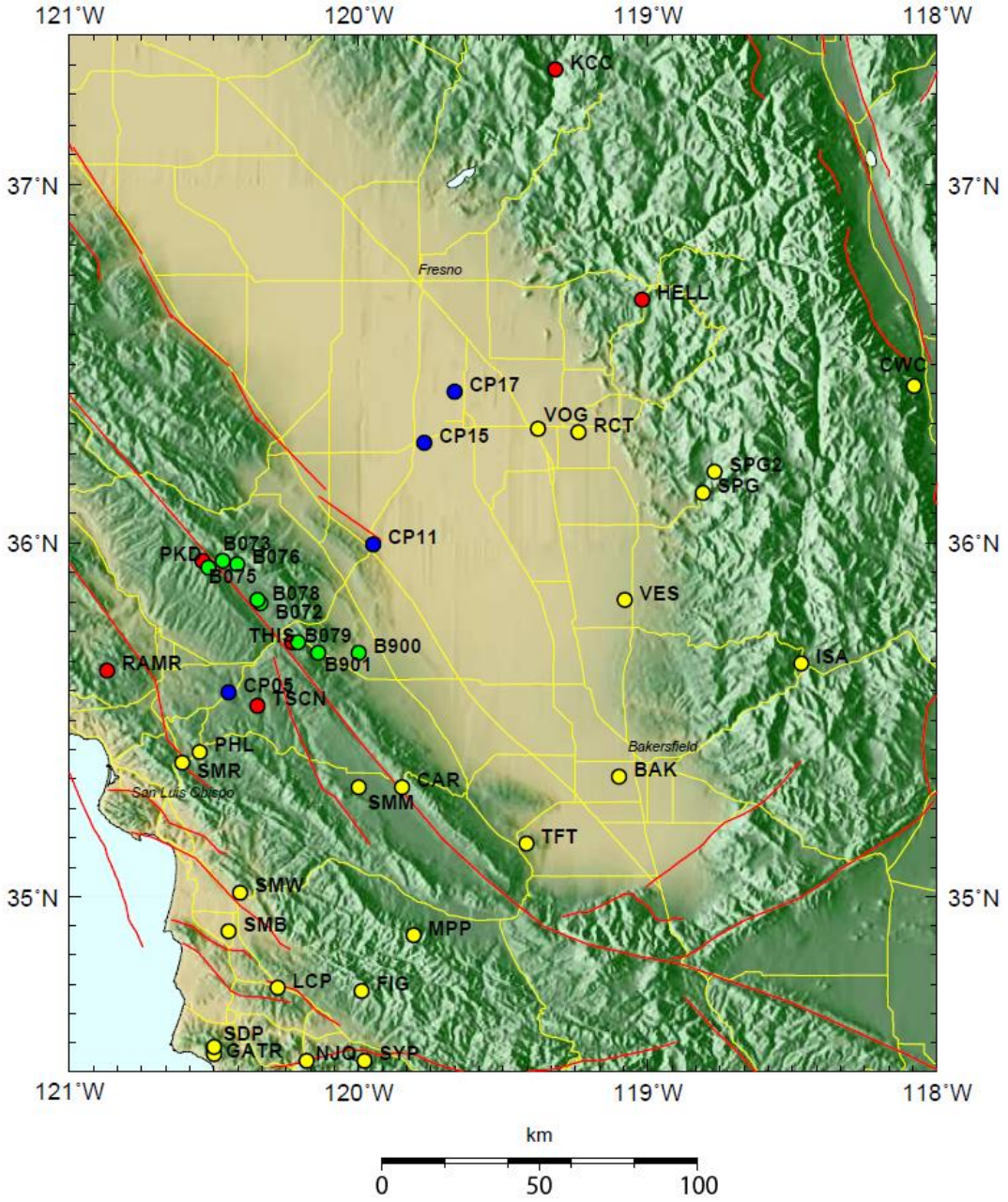

Figure 3.1: Map of the study area with seismic stations shown by circles with various colors. Yellow, CI network stations; Red, BK network stations; Green, PB network stations; Blue, GC network stations.

Receiver functions were calculated with the iterative deconvolution method as

described by Ligorria and Ammon (1999). The misfit between estimated receiver functions convolved with the vertical component seismogram and the radial component seismogram were minimized at each iteration. The Iteration was performed until the change in the misfit gets smaller than 0.01% or until the iteration was performed 400 times.

Table 3-1: Station information with date span of events used and the number of events used for each stations.

Station	Network	Latitude	Longitude	Elevation(m)	Date Span of Events used	Number of Events
SYP	CI	34.53	-119.98	1278	06/2001-01/2013	675
NJQ	CI	34.53	-120.18	219	03/2002-01/2013	609
GATR	CI	34.55	-120.50	590	09/2008-01/2013	235
SDP	CI	34.57	-120.50	631	03/2002-08/2006	199
FIG	CI	34.73	-119.99	945	09/2001-04/2013	64
LCP	CI	34.74	-120.28	199	12/2001-02/2013	588
MPP	CI	34.89	-119.81	1739	03/2002-01/2013	650
SMB	CI	34.90	-120.45	74	03/2002-07/2004	73
SMW	CI	35.01	-120.41	169	12/2008-02/2013	256
TFT	CI	35.15	-119.42	233	02/2003-01/2013	559
CAR	CI	35.31	-119.85	765	01/2007-02/2013	483
SMM	CI	35.31	-120.00	599	01/2001-01/2013	801
PHL	CI	35.41	-120.55	355	01/2001-02/2013	725
SMR	CI	35.38	-120.61	341	05/2008-02/2013	300
BAK	CI	35.34	-119.10	116	01/2001-02/2013	698
ISA	CI	35.66	-118.47	873	01/2001-02/2013	784
CWC	CI	36.44	-118.08	1596	01/2001-02/2013	665
VES	CI	35.84	-119.08	154	01/2001-02/2013	843
SPG	CI	36.14	-118.81	314	01/2001-12/2005	259
SPG2	CI	36.20	-118.77	627	12/2005-02/2013	502

RCT	CI	36.31	-119.24	107	01/2001-05/2012	806
VOG	CI	36.32	-119.38	90	06/2011-02/2013	106
RAMR	BK	35.64	-120.87	417	11/2004-02/2013	583
PKD	BK	35.95	-120.54	583	01/2001-01/2013	738
THIS	BK	35.72	-120.23	643	05/2012-04/2013	51
TSCN	BK	35.54	-120.35	477	03/2012-04/2013	45
HELL	BK	36.68	-119.02	1140	04/2005-02/2013	476
HAST	BK	36.39	-121.55	542	02/2006-02/2013	437
KCC	BK	37.32	-119.32	888	01/2001-07/2012	760
B072	PB	35.83	-120.34	398	03/2010-02/2013	259
B073	PB	35.95	-120.47	535	03/2010-02/2013	251
B075	PB	35.93	-120.52	583	03/2010-02/2013	228
B076	PB	35.94	-120.42	445	03/2010-02/2013	244
B078	PB	35.84	-120.35	387	03/2010-02/2013	253
B079	PB	35.72	-120.21	437	03/2010-02/2013	260
B900	PB	35.69	-120.00	220	03/2010-02/2013	219
B901	PB	35.69	-120.14	275	03/2010-02/2013	256
CP05	GC	35.58	-120.45	394	05/2012-04/2013	49
CP11	GC	36.00	-119.95	80	05/2012-04/2013	57
CP15	GC	36.28	-119.77	69	06/2012-04/2013	46
CP17	GC	36.42	-119.67	79	06/2012-12/2012	16

Data Analysis

The first step to analyze the receiver function is to identify the Moho converted signal (Ps arrival). Some criteria I used to identify them is (1) to look for a signal that is expected from crustal models made from previous geophysical studies (2) to look for azimuthal variation and changes from different ray parameters, and (3) to look for similarities in nearby stations.

Once signals from Moho arrivals and crustal structures were identified for stations with clean receiver functions, signals from same structure can be identified in nearby stations to expand the model regionally.

The receiver function is less sensitive to *Vp*, but strongly depends on the *Vp/Vs* ratio (Zhu and Kanamori, 2000). So the estimation of the *Vp/Vs* ratio becomes extremely important. To calculate the *Vp/Vs* ratio, I used the X-tPs method described by Helffrich and Thompson (2010), where the timing relationship between the Pms arrival and its multiples is used for the estimation.

tPs can be expressed in terms of crustal thickness as;

$$t_{Ps} = \mathrm{h}(\sqrt{V_s^{-2} - p^2} - \sqrt{V_p^{-2} - p^2}). \qquad (3.1)$$

And similarly, *tPpPs* and *tPsPs* can be expressed as;

$$t_{PpPs} = \frac{h}{V_p}(\sqrt{R^2 - p^2V_p^2} + \sqrt{1 - p^2V_p^2}) \ , \qquad (3.2)$$

$$t_{PsPs} = \frac{2h}{V_p}\sqrt{R^2 - p^2V_p^2} \ , \qquad (3.3)$$

where *R* is the *Vp/Vs* ratio. Helffrich and Thomson (2010) introduce a stacking control parameter *X* defined as the following;

$$\mathrm{X} = \frac{R^2 - p^2 V_p^2}{1 - p^2 V_p^2} \qquad (3.4)$$

tPpPs and *tPsPs* can then calculated as;

$$t_{PpPs}(X) = t_{Ps} \frac{(X^{1/2}+1)}{(X^{1/2}-1)} \qquad (3.5)$$

$$t_{PsPs}(X) = t_{Ps} \frac{2X^{1/2}}{(X^{1/2}-1)} \qquad (3.6)$$

By stacking receiver functions along a range of *X* and *tPs* as in figure 3.2, the *tPs* and *Vp/Vs* ratio can be chosen to maximize the amplitude of the sum of *tPs, tPpPs* and *tPsPs* arrivals. After the *Vp/Vs* ratio is obtained, crustal thickness can be calculated using an average crustal P-wave velocity. A typical *Vp* value for California of 6.2km/s will be a good estimate for receiver functions (Zhu and Kanamori, 2000) unless the station is located on a low-velocity basin structure.

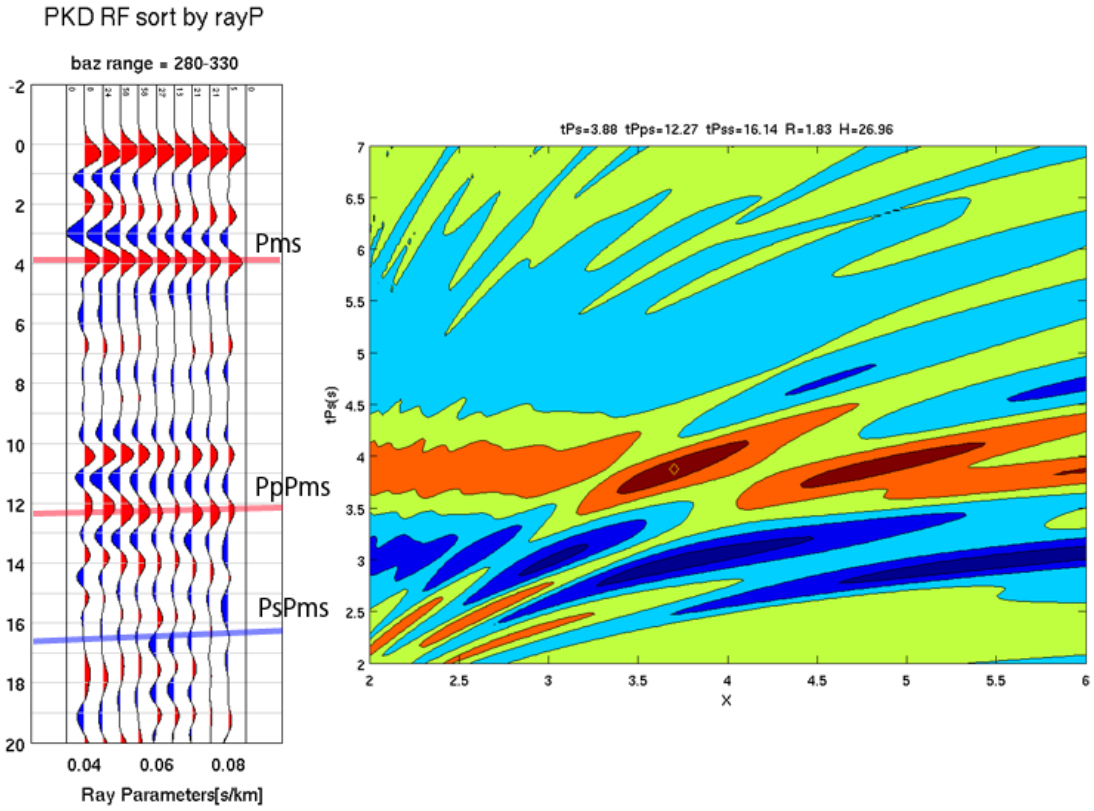

Figure 3.2: (Left) PKD station receiver functions sorted by ray parameters for back azimuth range of 280º to 330º. Signals marked by red and blue lines are Pms and its multiples calculated by the X-tPs method. (Right) X-tPs plot. Contours colored with red represents high correlation between the Pms signal and its multiples, and blue shows the low correlation contours.

Results

In this section I show my results for each geographic region starting with the Coast Ranges, then the Great Valley, and lastly the Sierra Nevada. Appendix A shows the results from all the stations: one plot of receiver functions stacked by different back azimuth, and one plot stacked by different ray parameters. Since the main event sources are located in 3 regions: central

to South America, near Fiji Islands, and Alaska, which gives back azimuths near 125º, 225º, and 305º respectively, the ray parameter stack was separately performed in the ranges 125º±25º, 225º±25º, 330º±25º to account the azimuthal difference in the subsurface structures. These three groups correspond to rays coming in sub-parallel (northeast and southwest), and at right angles to the orientation of the northwest-southeast trending geographic features in the area.

-Coast Ranges Stations (Part 1, Near the San Andreas Fault):

Station PKD

First I show results from stations in the northeast side of the Coast Ranges near the San Andreas fault, including stations PKD, THIS, CP05, TSCN, SMM, CAR, and all the PB stations as shown in figure 3.1. Receiver functions from station PKD are well-studied by Ozacar and Zandt (2009), and their results and interpretation are shown in figure 3.3 for comparison with my results. The receiver function results are in very good agreement with Ozacar and Zandt (2009), and the signal from boundary *tL1*, *tH*, and *tL2* can be identified as discussed in their paper. Both the *Vp/Vs* ratio and the crustal

thickness calculated from the X-tPs method are in good agreement with values obtained by Ozacar and Zandt (2009).

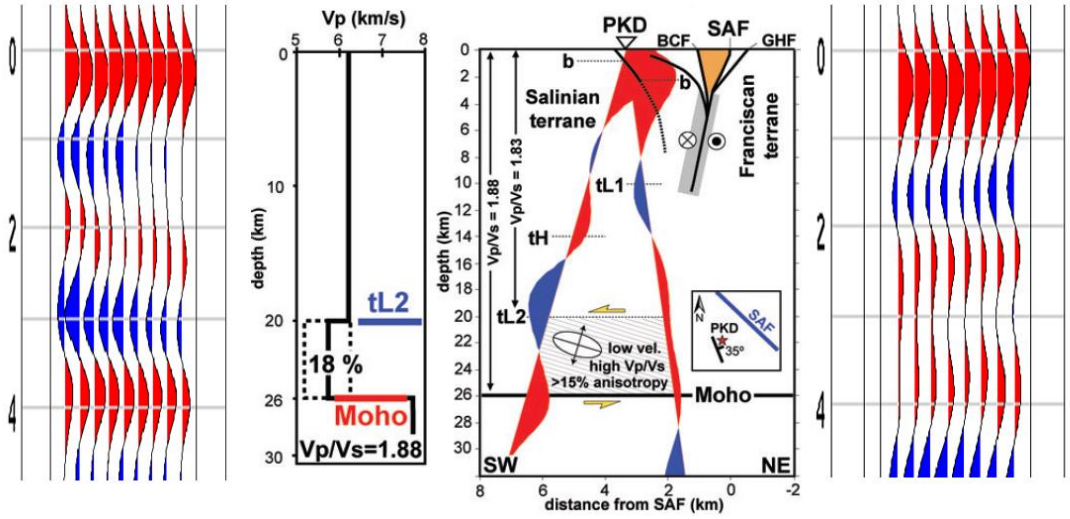

Figure 3.3: Comparison of PKD receiver functions with the result shown in (Ozacar and Zandt, 2009). The receiver function plot shown on the left and right corresponds to SW and NE receiver functions from (Ozacar and Zandt, 2009) in the center. SAF, San Andreas fault; BCF, Buzzard Canyon Fault; GHF, Gold Hill Fault; tL1, top of the low-velocity layer in the mid-crust near SAF; tH, top of the high-velocity layer in the mid-crust west of the station; tL2, top of the low-velocity layer in the lower crust.

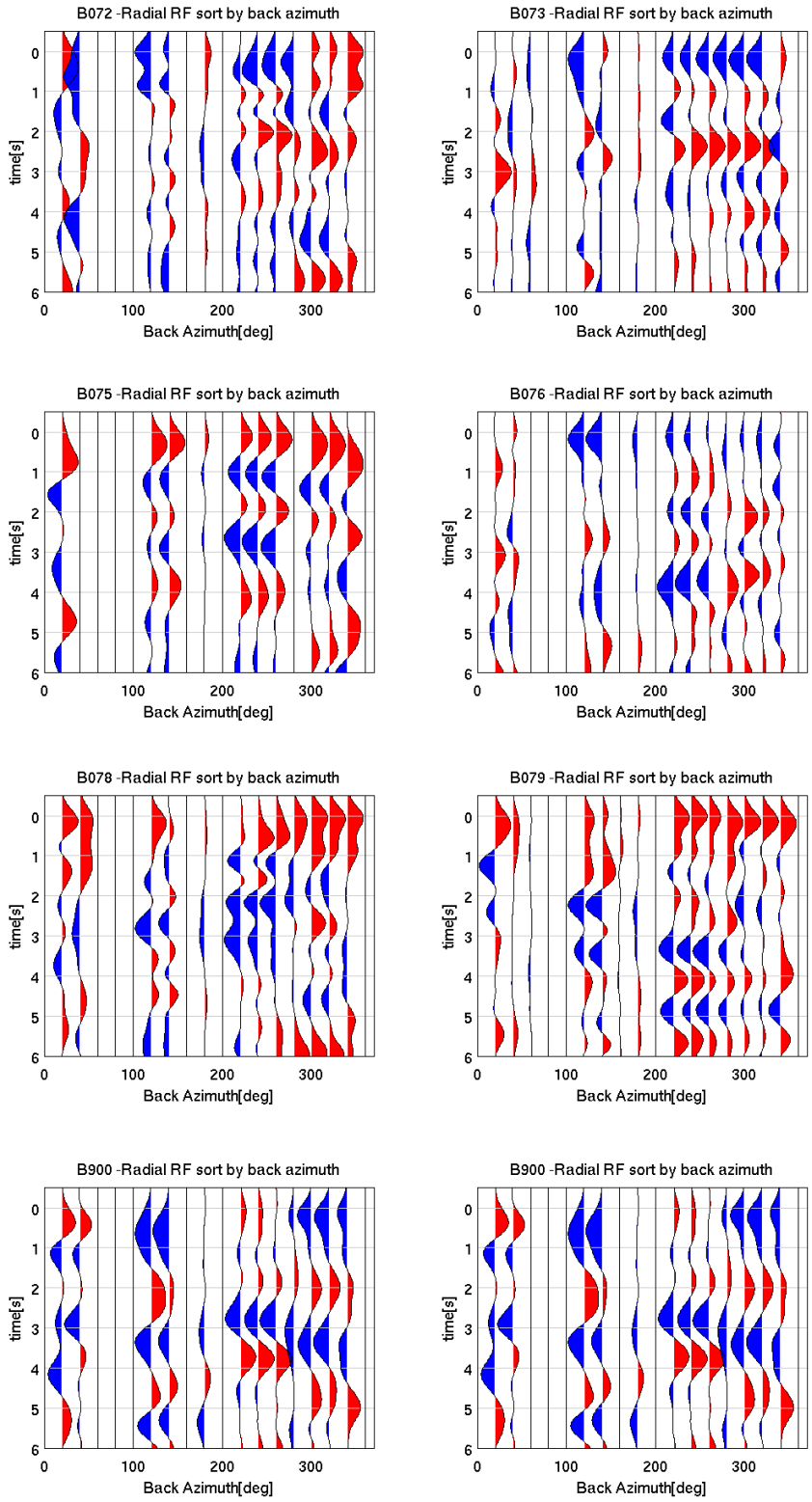

Figure 3.4: Receiver functions plot from all the borehole stations in PB network.

Borehole Stations

Figure 3.4 shows the receiver functions from borehole stations (PB), and interestingly only the half of the stations show the 0 sec peak. As mentioned in chapter 2, this 0 sec peak is a small portion of the first arrival P-wave energy that shows up in horizontal component seismograms from the non-verticality of the incident ray. The consistency of receiver functions shows that the converted signals are not contaminated by noise, but are showing geologic structures. This absence of the 0 sec peak has been observed from basin stations (Zheng et al., 2006), where complicated near-surface structure affects the early arrivals of receiver functions, but basin effects are not expected for the location for these stations. A possible cause of this complication is the depth of the stations, but theoretically the stations are not buried deep enough to change the surface boundary effects. Considering a case of a very short wavelength incident ray where the S-wave velocity is 1 km/s, the frequency range of 0.1-1.0 Hz used in this study gives the shortest wavelength of 1 km. The stations are buried 150 to 250 m below the surface, and the $\geqq$1 km wavelength is big enough that the borehole stations will not be affected by boundary effects. However, if the velocity is very low, near-surface

up-going and down-going waves may interfere to cause the complication. Table 3.2 shows the relationship between the burial depth and observed receiver functions, but no obvious relationship can be found.

Table 3-2: Station information for the borehole stations.

Station	Latitude	Longitude	Elevation(m)	Install Depth(m)	0 sec peak
B072	35.83	-120.34	398	155	No
B073	35.95	-120.47	535	236	No
B075	35.93	-120.52	583	166	Yes
B076	35.94	-120.42	445	193	No
B078	35.84	-120.35	387	175	Yes
B079	35.72	-120.21	437	175	Yes
B900	35.69	-120	220	181	Yes
B901	35.69	-120.14	275	173	No

The PB stations B075, B078, B079, and B901 give a 0 sec peak, but stations B073, B076, B072, and B900 do not give a 0 sec peak, suggesting that extra complexity affects the borehole station receiver functions. To see if these borehole stations are useful for receiver function study, I compared close-by sets of borehole stations and broadband stations in figure 3.5 (PKD with B075, and THIS with B078). Note that B075 and B078 both have a good 0 sec peak. Looking at the receiver functions from PKD for the back azimuth range of 200 to 250, signals from mid-crustal layers (tH and tL2) and Moho as discussed by Ozacar and Zandt (2009) are present at 1.9, 2.8, and 3.9 sec

respectively, and the same signals are present at 1.9, 2.7, and 4.0 sec in B075. In the receiver function plot from THIS in the azimuthal range of 100 to 150, two positive peaks can be observed before the Ps arrival, one at 1.7 sec and one at 2.8 sec.

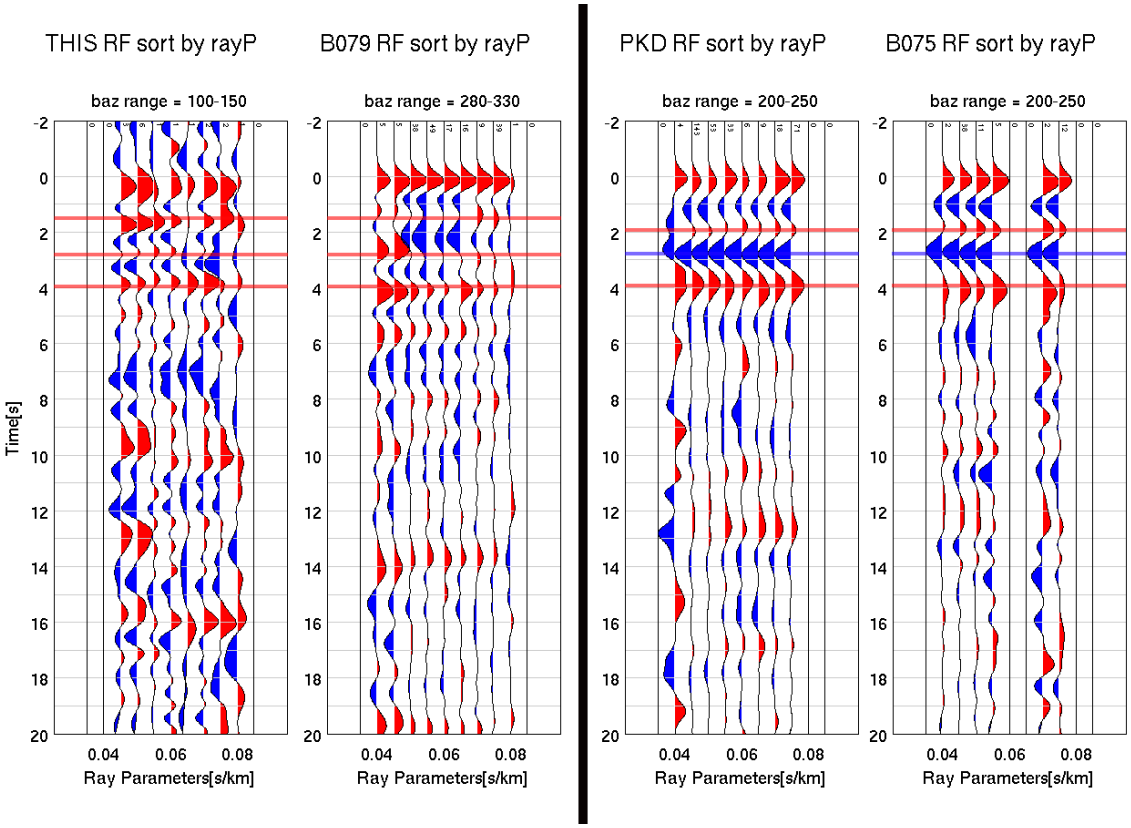

Figure 3.5: Borehole station receiver functions with 0 sec peak compared with nearby broadband stations. The red and blue lines denote the similarities in the positive and negative signals in the receiver functions.

Then the Moho arrival comes in at 3.9 sec, which is consistent with PKD. Now comparing that to B079 for the azimuthal range of 280 to 330, two positive

signals can be observed at 1.3 and 2.8 sec, and a Ps signal at 4.0 sec. These similarities suggest that the receiver functions from the borehole stations with presence of a 0 sec peak are reliable.

Now looking at the borehole stations with no 0 sec peak, B076 and B073 is close by PKD so I compared them in figure 3.6.

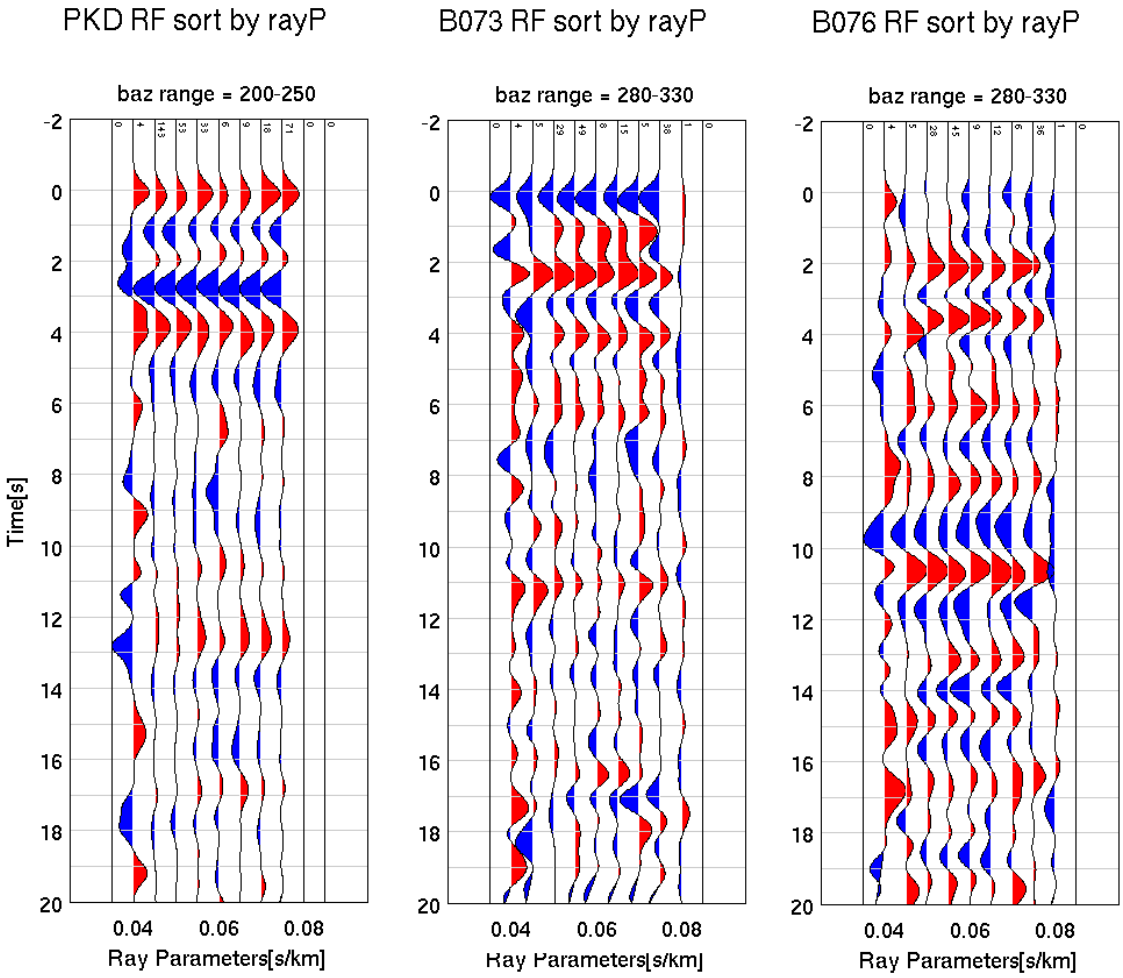

Figure 3.6: (Center-B073 and right-B076) Borehole station receiver functions with no 0 sec peak compared with (left-PKD) nearby broadband station.

Again the mid-crustal layer (*tH*, *tL2*) and Moho signals are present in PKD at 1.9, 2.8, and 3.9 sec respectively. Although first 1.5 sec of the receiver function is very different, both B073 and B076 have similar signals. B073 has very strong signal at 2.3, 3.1, and 4.0 sec that might correspond to mid-crustal layer (*tH* and *tL2*) and Moho, and B076 has a similar signal at 2.1, 2.9, and 3.7 sec. It seems as if the first couple of seconds of the receiver function are showing effects from some near surface structure that overtake the 0 sec peak, but that the later arrivals are consistent. However, the Moho arrival is weak or does not appear in some azimuthal ranges for B073 and B076 (appendix A). Detailed comparison with other stations is necessary for these stations to be used to infer crustal structure.

Between the Coast and the San Andreas Fault

CP05 and TSCN are located ~20 km southwest of the San Andreas fault, and it is an important location to connect observations at stations near the coast to those of the stations near the San Andreas fault; however, as it is shown in Appendix A, both CP05 and TSCN give very noisy receiver functions. A very small 0 sec peak is present at TSCN and none can be observed at CP05.

Both the stations have a strong signal near 1.0 sec, and CP05 shows weak energy coming-in near 3.3 sec that might correspond to a Moho arrival, but it is not present at TSCN. In fact, there is no positive signal from 3 to 6 sec at TSCN, the time range for which Ps arrival is expected. It might be that the steep contrast across the Crust-Mantle boundary is absent at this location due to volcanic activity, or that the Moho is dipping in a direction to make a weak Ps converted phase. Dickinson (1997) compiled locations of post-mid-Miocene volcanic fields, but the locations of these stations are outside the volcanic field suggesting that clear Moho should exist. Both the stations are newly installed and not enough data is available at this point to check from the azimuthal variation whether the Moho is dipping. I cannot explain this complication for these two stations and so I do not use stations CP05 and TSCN in this study.

-Coast Ranges Stations (Part 2, Near the Coast):

San Luis Obispo

From the stations by the coast, three stations near San Luis Obispo, RAMR, PHL and SMR (Figure 3.1), have the clearest Ps arrival. Similar to station PKD, all three stations are located on the Salinian block, and similarities in receiver functions are expected. Consistent signal near 3 sec is observed in all three stations from different back azimuth ranges (appendix A), and the signal was interpreted as the Moho Ps arrival. Looking at PHL and SMR (the receiver functions from RAMR gets very oscillatory after the Ps arrival and it is very difficult to identify multiples), there are two signals that could be interpreted to be a Pps arrival. Figure 3.7 shows the receiver functions from the station PHL, and the two candidates for the multiples can be seen from the corresponding X-tPs plot.

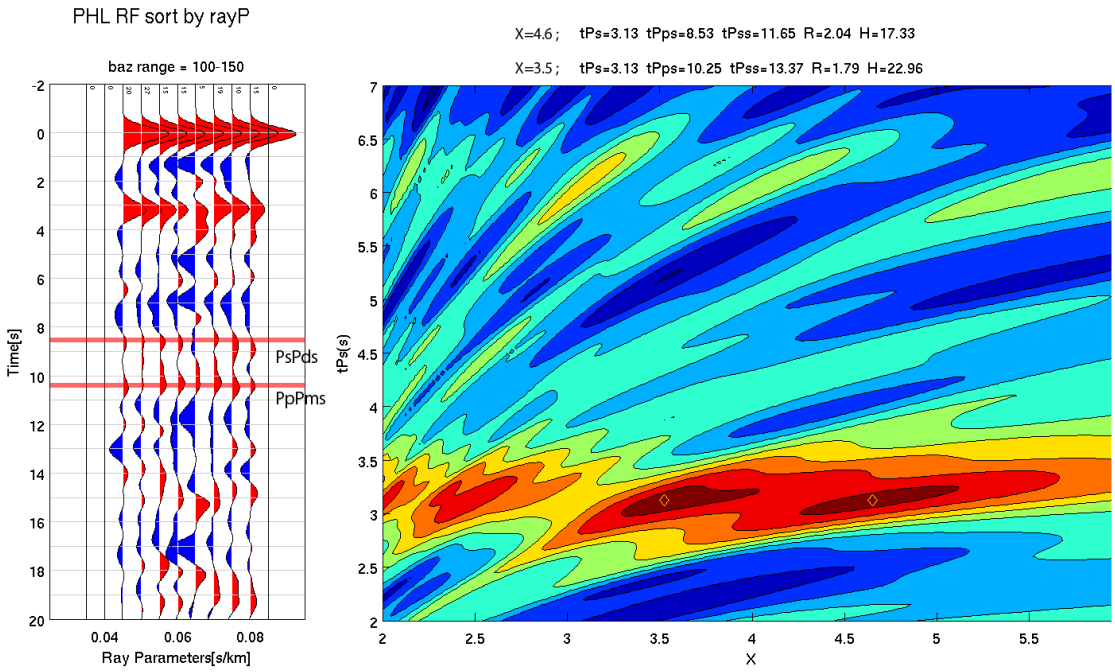

Figure 3.7: (Left) Receiver functions from station PHL sorted by ray parameters for back azimuth range of 100º to 150º. Red lines denote the multiples from P-to-S converted phases at different boundaries. (Right) X-tPs plot. Two dark red peaks show two candidates for the PpPms signal, and the data above the contour plot show corresponding crustal structures calculated from the two peak values. R, Vp/Vs ratio; H, crustal thickness (km).

A positive signal at 8.5 sec gives the maxima at the higher (4.6) X value and a positive signal at 10.3 sec gives the maxima at the lower (3.5) X value. 10.3 sec for the PpPms arrival-time results in 23 km thick crust, and this value is favored here from the comparison with other geophysical studies (Trehu and Wheeler, 1987; Miller et al., 1992) whereas the PpPms arrival-time of 8.5 sec results in an unexpectedly shallow Moho.

The positive signal at 8.5 sec was interpreted as evidence for a low-velocity zone at the base of the crust. The signal is so clear and consistent that it is unlikely to be noise, but it arrives too early to be a Moho PpPms arrival and too late to be a mid-crustal PpPds arrival. However, a low-velocity layer will switch the polarities (*from Ps(+), PpPs(+), PsPs(-) into Ps(-), PpPs(-), PsPs(+)*). Therefore I interpret the positive 8.5 sec signal as a mid-crustal PsPds arrival associate with the top of a low-velocity zone in the crust. A low-velocity layer at the base of the crust observed in PKD receiver functions has been interpreted as a serpentinite or fluid filled schist layer (Ozacar and Zandt, 2009). The receiver function result from these near-coast stations suggests that the low-velocity layer continues from the coast to the plate boundary at the San Andreas fault.

Santa Maria Basin

At the south of the three stations of the previous section, stations LCP and SMB are located in Santa Maria basin, which is a Neogene pull-apart basin that was later affected by compressional tectonics (Isaacs et al., 1992; Trehu, 1991). Figure 3.8 shows the receiver functions from these two stations, and

the complication from the basin structure can be observed.

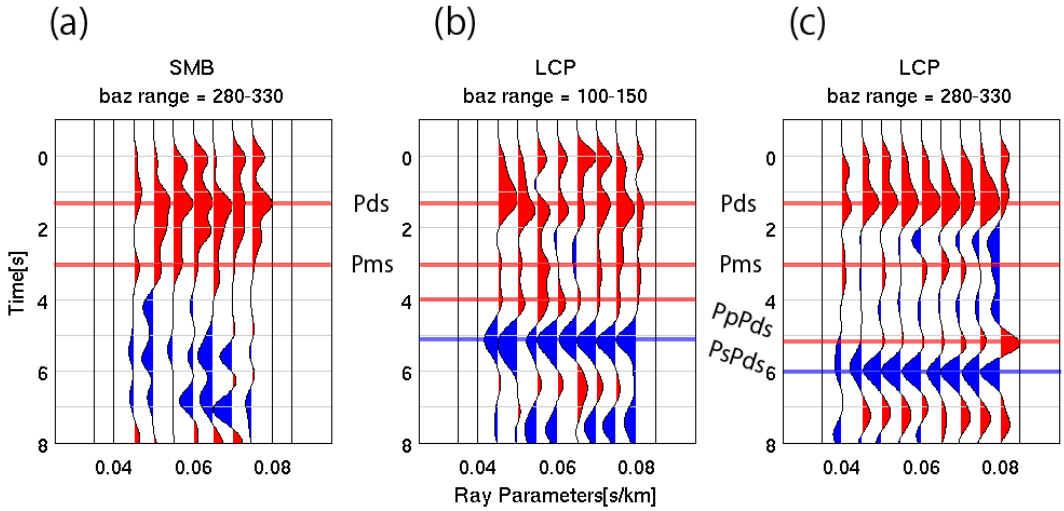

Figure 3.8: Santa Maria Basin receiver functions sorted by ray parameter for (a) station SMB with back azimuth range of 280º to 330º, and for (b,c) station LCP with back azimuth range of 100º to 150º and 280º to 330º. Red and blue lines denote the similarities in the positive and negative signals in the receiver functions. Labels between the plots show the interpretation for the each signal.

The stations are located above a 3-5 km thick basin according to a Santa Maria basin depth contour map (Crawford 1971), and the strong positive signal near 1.0 to 1.5 sec was interpreted as a P-to-S converted phase from the base of the basin. Figure 3.8 (b,c) shows receiver functions from LCP for the back azimuth range of 100 to 150 and 280 to 330. Looking at the receiver functions from 100 to 150 back azimuth, four positive signals near 0, 1.2, 3.0, and 4.0 sec, and a strong negative signal from 5.0 sec can be observed. In the receiver

functions from 280 to 330 back azimuth, the 0, 1.2, and 3.0 sec signals are still present but the strong negative signal from 5.0 sec seems to be shifted +1.0 sec along with the 4.0 sec positive signal. This set of positive and negative signals were interpreted as multiples of the basin Pds signal; PpPds and PsPds respectively, and the positive signal from 3.0 sec was interpreted as a Ps wave from the Moho. Since the multiples have to travel a longer distance, they are more sensitive to lateral depth variation, and this shift in the basin PpPds and PsPds signals represents dip in the base of the basin. The direct P-to-S converted signals at 1.2 and 3.0 sec, on the other hand, are less sensitive to the depth variation, and they are present in both of the back azimuthal ranges without any shifts.

Now, comparing the observation from the LCP with SMB (figure 3.8 (a,b)), the strong positive signal near 1.2 sec seen in LCP is also present in SMB, but no consistent basin multiples can be observed. However, a small but consistent positive signal is present at 3.0 sec and direct P-to-S converted phases from both basin and Moho are observed at both stations. As for inverting this arrival-time information into crustal thickness, using the average crustal velocity of 6.2 km/s used for other stations is misleading

because of the low-velocity basin structure (Pelkum and Ben-Zion, 2012). So basin thickness information becomes important. However, although the clearly observable basin multiples are seen in the LCP receiver functions, to calculate the average basin *Vp/Vs* ratio becomes very difficult because of the dip in the base of the basin. Multiples in a dipping structure travel through a longer distance laterally, and the ray path is more complicated (MacKenzie et al., 2010). Since the change in velocity becomes larger near the surface of the basin, the *Vp/Vs* ratio obtained from basin multiples may not represent a correct average value for the ray path which the Ps phase traveled through. So we use a 2-layer model comprised of a typical deep basin structure (Zuleta 2012) (*Vp/Vs* = 2.0 and *Vp* = 3.3 km/s) and a typical ctustal structure (*Vp/Vs* = 1.73 and *Vp* = 6.2). Then the receiver functions observed at LCP and SMB give a basin thickness of 4.3 km and 2.4km respectively, and the crustal thickness of ~20 km.

Other Stations in the Coast Ranges

Stations SMW, SDP, and GATR are located around the Santa Maria basin. They all have a Pms arrival between 3.1 and 3.6 sec, and the average

Moho depth is calculated to be 26 km. The crustal thickness at the southern part of the Coast Ranges station is thicker compared to RAMR, PHL and SMR which are located towards the north. Moho beneath the Santa Maria basin is an exception where the smallest crustal thickness in the study area is observed. Stations SYP, FIG and MPP are located inland from the Santa Maria basin, and the average Moho Ps arrival is 4 sec. The corresponding Moho depth is 29 km, and is shows that a higher Moho depth gradient can be seen in the south.

-Great Valley Stations:

The southern part of the Great Valley is called the San Joaquin Valley, and 8 stations are located there. Cenozoic strata and Cretaceous Great Valley sequence lies over mafic basement, where the basement is dipping towards the west. At the front of the Diablo Range, the basin depth reaches up to 15 km (Wentworth and Zoback, 1990; Walter, 1990). A basin thickness contour map and a refraction profile (shot point 9 to 12 is shown in the contour map with a solid triangle mark) from the San Joaquin Valley are shown on figure 3.9. The depth and velocity information taken from the map were used to interpret the receiver functions. Since only stations CP11, CP15, CP17, VOG, RCT, and VES lie in the basin, the interpretation is focused on these stations.

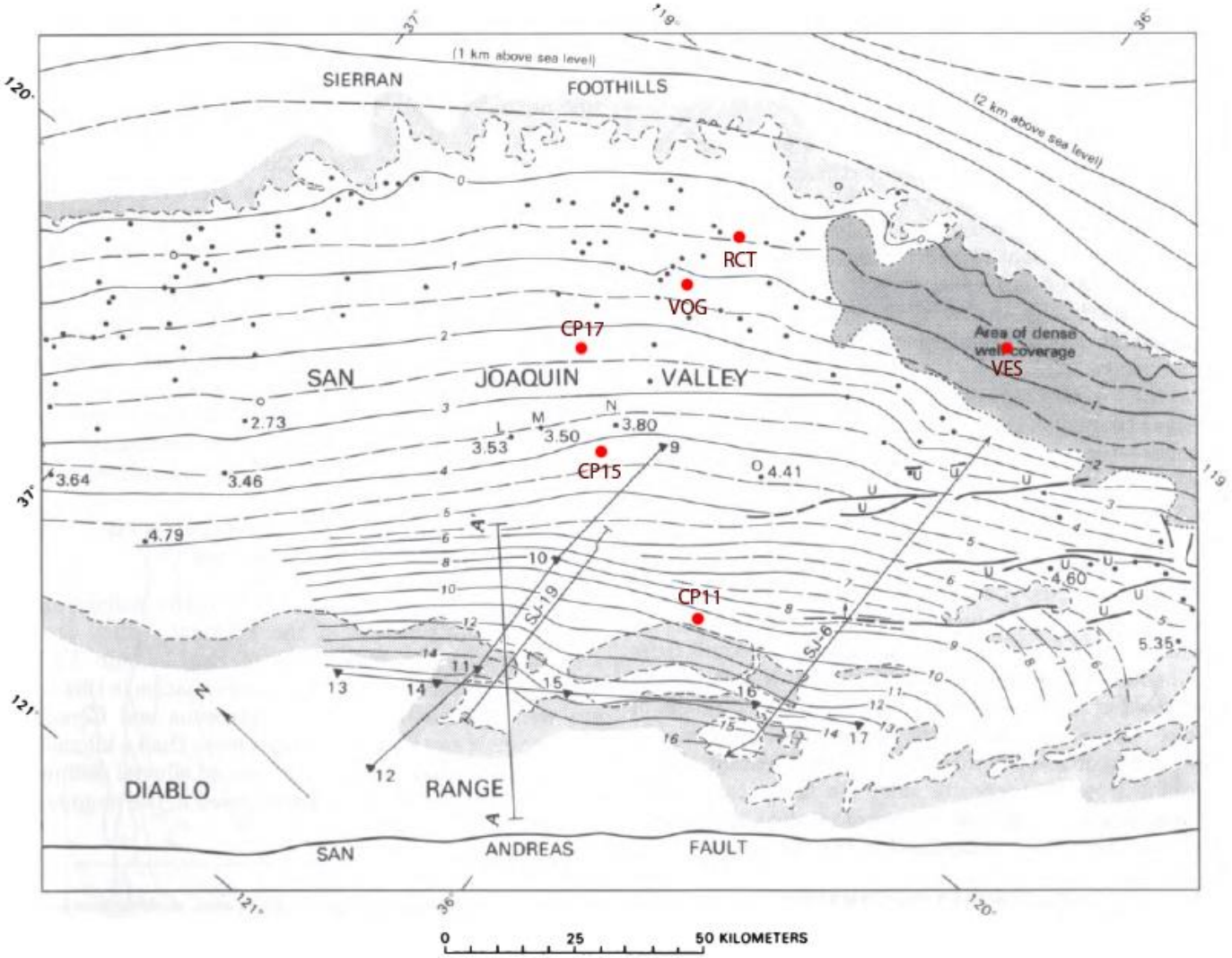

Figure 3.9: Surface configuration of Great Valley basement with station locations. Contours (in kilometers below sea level; long-dashed line, 500m) drawn from depth to crystalline rock in wells and from seismic reflection and refraction profiles. Modified from Wentworth and Zoback (1990).

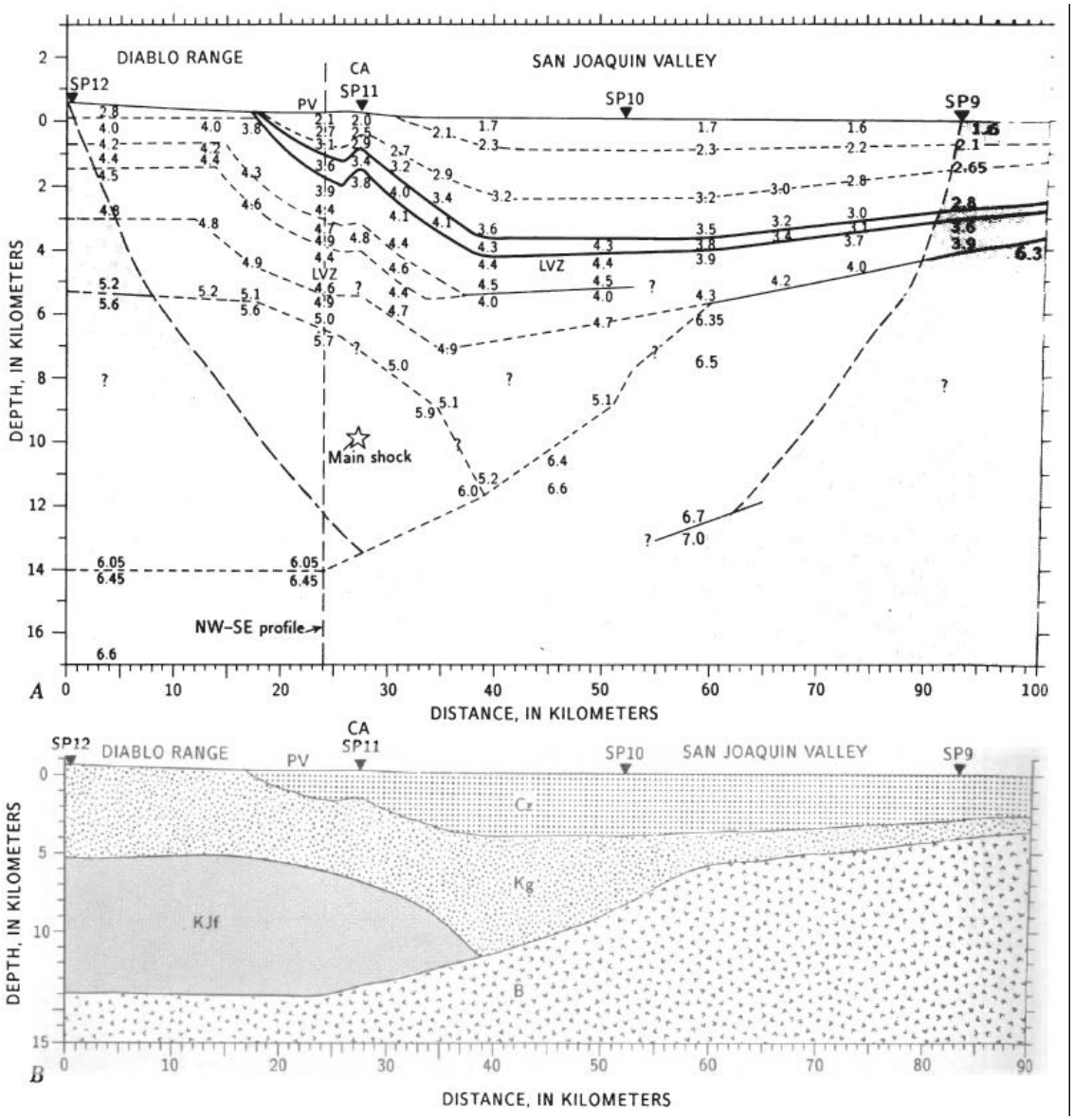

Figure 3.10: East-west refraction profile from shot point 9 to 12 shown in figure 3.9. (Top) LVZ, low-velocity zone; PV, Pleasant Valley syncline. Heavy solid lines, geologic contact constrained by well data; light solid line, velocity boundary constrained by reversing refraction data; dashed line, velocity boundary inferred from unreversed refraction data; question marks, extrapolated velocities. (Bottom) Model cross section showing geologic stratigraphic interpretation of velocity structure. B, basement; Cz, Cenozoic strata; Kg, Cretaceous Great Valley sequence; KJf, Jurassic and Cretaceous Franciscan assemblage. From Walter (1990).

Figures 3.11 shows the receiver functions from the above stations. The observed pattern in the receiver functions can be separated into three groups categorized by the basin depth below the stations. Station VOG, RCT, and VES are located in a shallow part of the basin with basin thickness below 1.5 km. Receiver functions from this group contain strong early arrivals, and they all have significant negative signal between 2 to 4 sec. Station CP15 and CP17 are located on a medium depth region of the basin with thickness between 2 to 5 km.

Interestingly, these stations have simpler receiver functions compared with those from shallow basin stations. Lastly, station CP11 is located on a deep part of the basin with basin thickness over 5 km. As shown in the reflection profile (figure 3.10), the dip of the basement increases abruptly on the west side of the 5km depth contour line, and CP11 is located on this steeply dipping basement. The receiver functions are very noisy and it is difficult to find consistent signals.

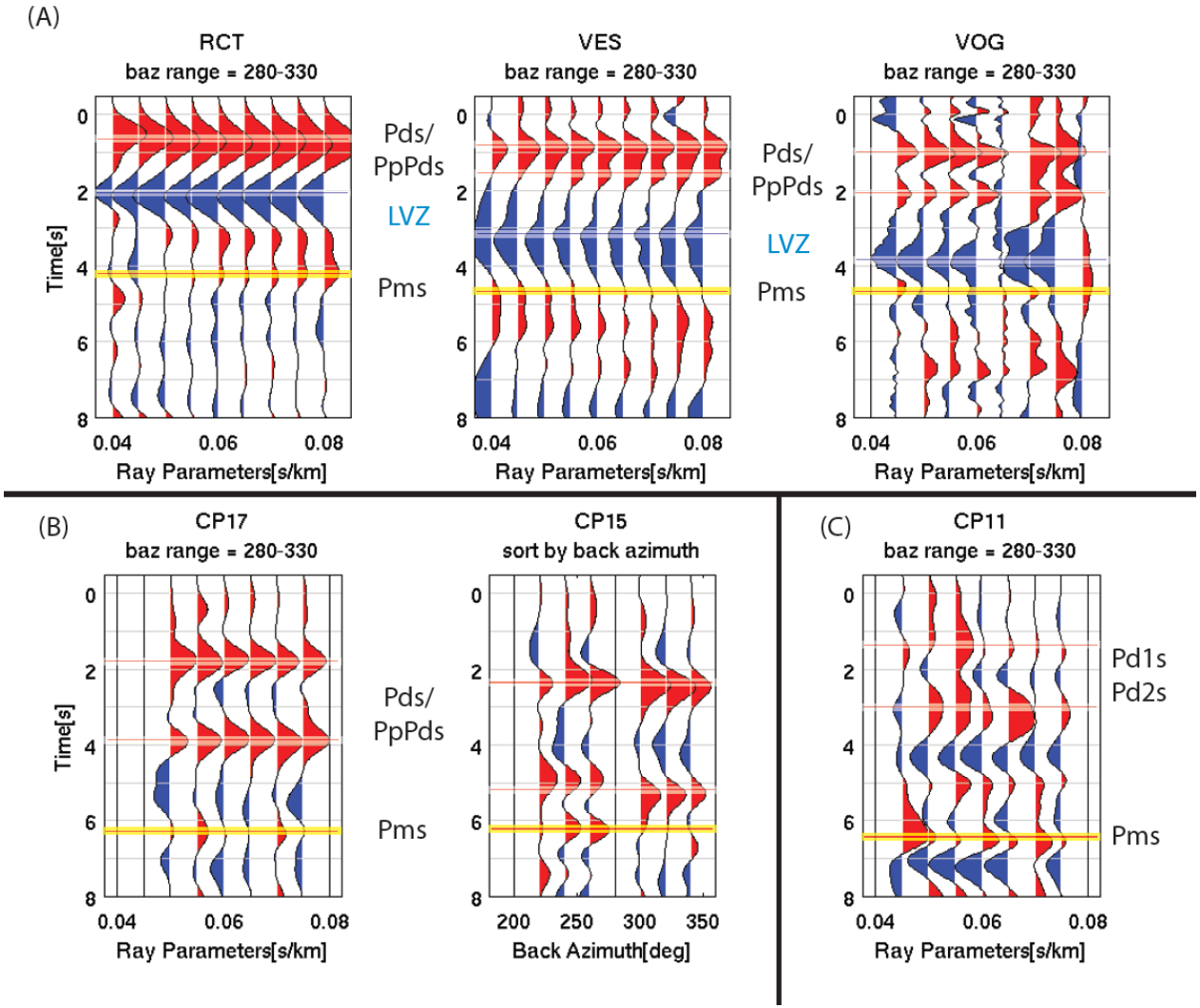

Figure 3.11
Great Valley receiver functions for stations located at
(A) shallow depth part of the basin,
(B) medium depth part of the basin and
(C) deepest part of the basin.

A common feature of all these receiver functions is that they all are missing the 0 sec peak (figure 3.11). This pattern is often observed in deep basin receiver functions (Zheng et al., 2006), and I interpreted this absence of P-wave energy in the horizontal component seismograms as an effect from the near surface slow-velocity sedimentary layers. The slow-velocity sedimentary layer will cause incident teleseismic P-waves to reach the surface almost vertically, leaving only a small amount of energy in the horizontal direction. Moreover, the smooth velocity change in the basin causes the seismic P-waves to penetrate the slower layers without significant conversion, so that the only observable signals in the receiver functions are the P-to-S converted phase at the base of the basin and multiples. Therefore the first strong signal observed between 0.5 and 3 sec in each basin station was interpreted as P-to-S converted phase from the basin/basement boundary except for station CP11. To construct the basin structures, average basin Vp/Vs ratios were calculated using the information from figure 3.9, the basin Ps arrival-time and the arrival-time of the basin Ps multiples.

Figure 3.11(A) shows the receiver functions from the shallow basin stations. The basin Ps arrivals for RCT, VES and VOG are 0.51, 0.81 and 0.92

sec respectively, and the order of delayed arrival-times is consistent with the thickening of the basin (figure 3.9). Receiver functions from RCT have smaller amplitude but broader signals, whereas VES and VOG have many narrow signals. The basin below RCT is the shallowest of the three stations, and the time differences between the basin Ps and its multiples are small. Therefore the signals appear as one broad signal at RCT, whereas the basin Ps and multiples can be distinguished at VES and VOG. A negative signal from basin PpSs arrival can be observed, but a stronger negative signal comes in after the PpSs arrival. The stronger negative signal suggests that there exists a low-velocity zone below the crystalline rock. Although the energy is small compared with the basin arrivals, the Moho Ps arrival can be observed near 4.2 sec in each station.

We next examine receiver functions at the stations from the medium depth part of the basin. Figure 3.11(B) shows the receiver functions from CP15 and CP 17. The receiver functions are simpler compared with the ones from the shallow part of the basin, and are dominated by two strong positive signals with 2-3 sec separation. The first signal corresponds to the basin Ps arrival, and the second to the basin PpPs arrival. No significant negative arrival

can be observed as in the receiver functions in the shallow part of the basin, and the low-velocity zone seems not to exist at this location. The positive signal after the basin Pps near 6.2 sec was interpreted as the Moho Ps arrival. The crustal thickness was calculated to be near 32-33 km at this area.

Lastly, the receiver functions from CP 11 are shown in figure 3.11(C). The noise of the receiver functions may be related to the steepness of the dipping basement. The first positive signal arrives at 1.4 sec, and the arrival is earlier compared with the receiver functions from the shallower part of the basin. The refraction profile (figure 3.10) shows increase in the velocity difference between the Cenozoic strata and the Cretaceous Great Valley sequence for the part of the basin deeper than 5 km, and this boundary maybe contributing to the first arrival in the CP11 receiver functions. The positive signal at 1.4 and 3.1 sec corresponds to P-to-S converted phase from mid-basin and basement respectively. It is difficult to model the multiples at this steeply dipping basin, but there is a repeatable signal coming in at 6.3 sec which corresponds to the Moho arrival from CP15 and CP17. The crustal thickness below CP11 is calculated to be near 35 km.

-Sierra Nevada Stations:

Receiver functions in the Sierra Nevada region have already been studied in detail by Frassetto et al. (2011), so they are briefly discussed in this section. Out of six Sierra Nevada stations, five of them are located in the western Sierra Nevada. Stations ISA, SPG, and SPG2 are located at the south end of the western Sierra Nevada (figure 3.1), and they all have strong Moho Ps arrivals at 4.8 to 5.2 sec (figure 3.12). The *Vp/Vs* ratio calculated from the X-tPs method gives a value between 1.74 and 1.77, and the corresponding Moho thickness is between 40 and 42 km. Station CWC at the eastern Sierra Nevada has a clear Moho Ps arrival at 3.8 sec, and the crustal thickness is calculated to be 30 km. Crustal thickness at the eastern Sierra Nevada is more than 10 km shallower than thickness in the west, and this observation is consistent with a previous receiver function study (Frassetto et al. 2011).

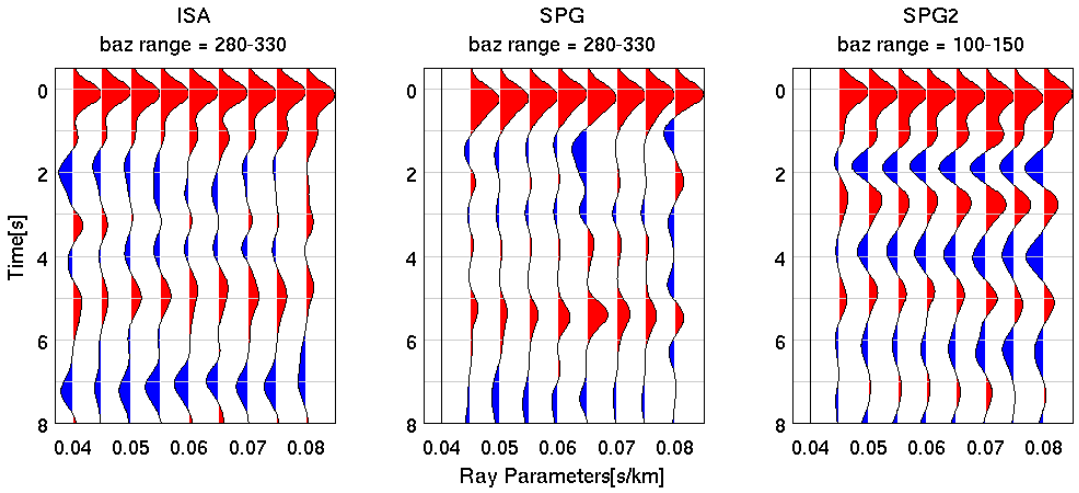

Figure 3.12: Sierra Nevada receiver functions from station ISA, SPG and SPG2. All of them have clear Moho P-to-S converted phase near 5 sec.

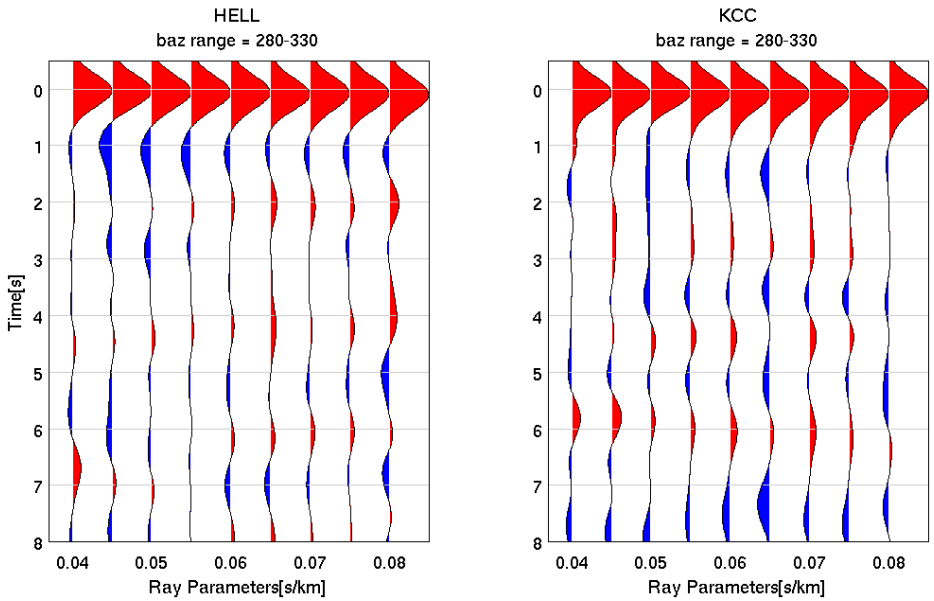

Figure 3.13: Sierra Nevada receiver functions from station HELL and KCC. These stations have almost no radial component energy converted from vertical component energy.

At the north of station SPG2, receiver functions from both KCC and

HELL show almost zero reflected and refracted energy (figure 3.13). Moho Ps arrival at these stations is almost invisible, and this zone of week Moho or "Moho hole" has been discussed as evidence that downwelling lithospheric mantle caused the Isabella anomaly (Zandt et al., 2004; Frassetto et al., 2011). However, Wang et al. (2013) argue that the region of the weak Moho is not confined to the vicinity of the Isabella anomaly, but extends along the entire western Sierra Nevada.

The summary of the observations for stations with recognizable Pms signal is shown in table 3.3.

Table 3-3: Interpreted Pms arrival-time and calculated Vp/Vs ratio and Moho depth for each station. (*) These stations have no clear Pms multiples for calculating Vp/Vs ratio, and the Vp/Vs ratio was estimated from nearby station.

Station	tPs(sec)	Vp/Vs	Moho depth(km)
PKD	3.9	1.85	26.9
B072(*)	3.6	1.85	24.6
B073	4.1	1.84	28.3
B075(*)	3.9	1.85	26.0
B076	3.5	1.89	22.7
B078(*)	3.8	1.85	25.7
B079	4.1	1.77	30.6
THIS	3.8	1.75	29.3
CAR	3.4	1.70	28.5
RAMR	3.2	1.78	23.8
PHL	3.0	1.73	23.9
SMR	3.4	1.90	21.7
SMW	3.6	1.75	27.7
SMB	3.3	1.93	20.4
LCP	3.0	1.89	19.3
SDP	3.2	1.72	25.3
GATR	3.4	1.76	25.9
MPP	3.9	1.72	31.2
FIG	3.8	1.72	30.5
SYP	4.1	1.87	27.2

Station	tPs(sec)	Vp/Vs	Moho depth(km)
CP11	6.4	2.05	35.1
CP15	6.1	2.09	32.1
CP17	6.3	2.08	33.3
VOG	4.3	1.91	27.1
RCT	4.3	1.95	26.0
VES	4.4	1.94	26.8
BAK	4.1	1.80	29.6
ISA	5.0	1.70	41.2
SPG	5.4	1.70	44.7
SPG2	5.0	1.66	43.2
CWC	3.8	1.70	31.3

Chapter4; Crustal Structure Model

From the observations shown in chapter 3, characteristics of the receiver functions can be subdivided into four categories by region; Coast Ranges, western San Joaquin Valley, eastern San Joaquin Valley, and Sierra Nevada. Figure 4.1 shows three samples of receiver functions for each category and their interpretation.

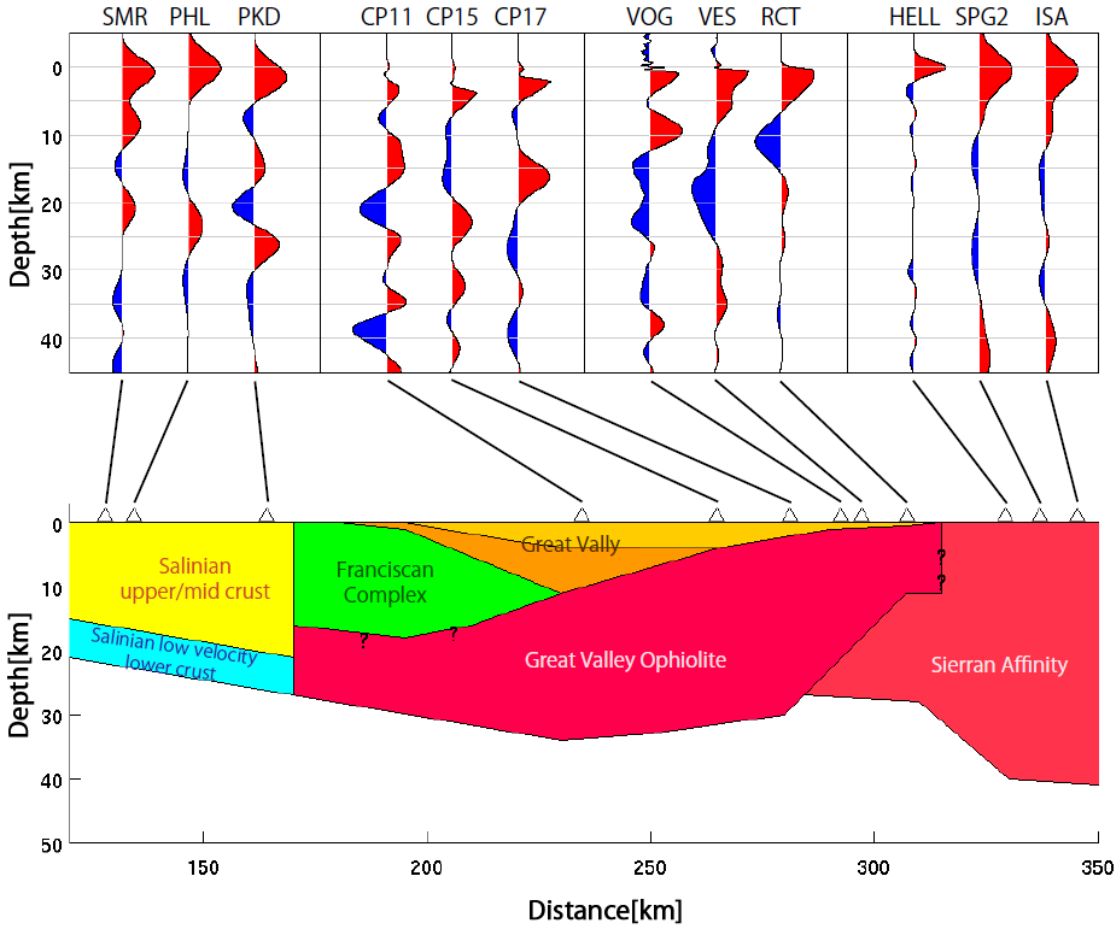

Figure 4.1: (Top) Three receiver functions each for Coast Ranges, western San Joaquin Valley, eastern San Joaquin Valley, and Sierra Nevada. (Bottom) Crustal model interpreted from the receiver functions.

At the Coast Ranges the Moho depth varies from 20 to 28 km, and it is generally deepening towards the east. They typically are associated with an upper crust layer, mid-crust layer, and a lower crust layer that is characterized as a low-velocity zone. The low-velocity layer at the base of the crust has been observed in data from a seismic reflection and refraction study (Trehu and Wheeler, 1987) and receiver function study (Ozacar and Zandt, 2009). The observations have been interpreted as sedimentary materials from subducted slab or a serpentinite layer. Some other reflection and refraction studies have observed a high-velocity oceanic crust layer at the base of the crust beneath the coast, and there has been discussion whether the high-velocity lower crust can be traced land-wards (Brocher et al., 1999; Miller et al., 1992). The high-velocity layer at the base of the crust has been interpreted as a stalled Farallon slab, suggesting that the Monterey micro-plate is continuous landward (Miller et al., 1992), but a relatively deep Moho from their crustal structure and the basal high-velocity layer from their interpretation is in disagreement with the receiver function result. The stalled slab model is expected if the Isabella anomaly originated from Monterey micro-plate; however the possibility that the slab is still attached to the Monterey

micro-plate but is detached from the base of continental crust is considered in the later discussion.

Receiver functions from western San Joaquin Valley have characteristics of one or two layers of thick sediments over a crystalline basal rock. Station CP15 and CP17 can be modeled by one sedimentary layer but CP11, which is located west of CP15, requires two sedimentary layers. The boundary at which basin can be modeled by one and two sedimentary layers corresponds to a location where Cretaceous Great Valley sequence below Cenozoic strata rapidly increases its thickness, and so the receiver functions are consistent with the basin structure. An average crustal thickness for this region is about 33 km, and the Moho depth seems to be thickening at a near constant rate from the Coast Ranges to western San Joaquin Valley. Receiver functions from Eastern San Joaquin Valley, on the other hand, resulted in more complicated signals with an early arriving large negative signal. This large negative signal in the eastern San Joaquin Valley was interpreted as a signal from low-velocity lower crust. Borehole data show 1.5 km thick low-velocity sedimentary layer over high-velocity crystalline rock (Wentworth and Zoback, 1990), and that is similar to the western San Joaquin Valley. Thus

the crustal model is comprised of 1-2 km of sediments overlying crystalline basement with a low-velocity layer at the base of the crust.

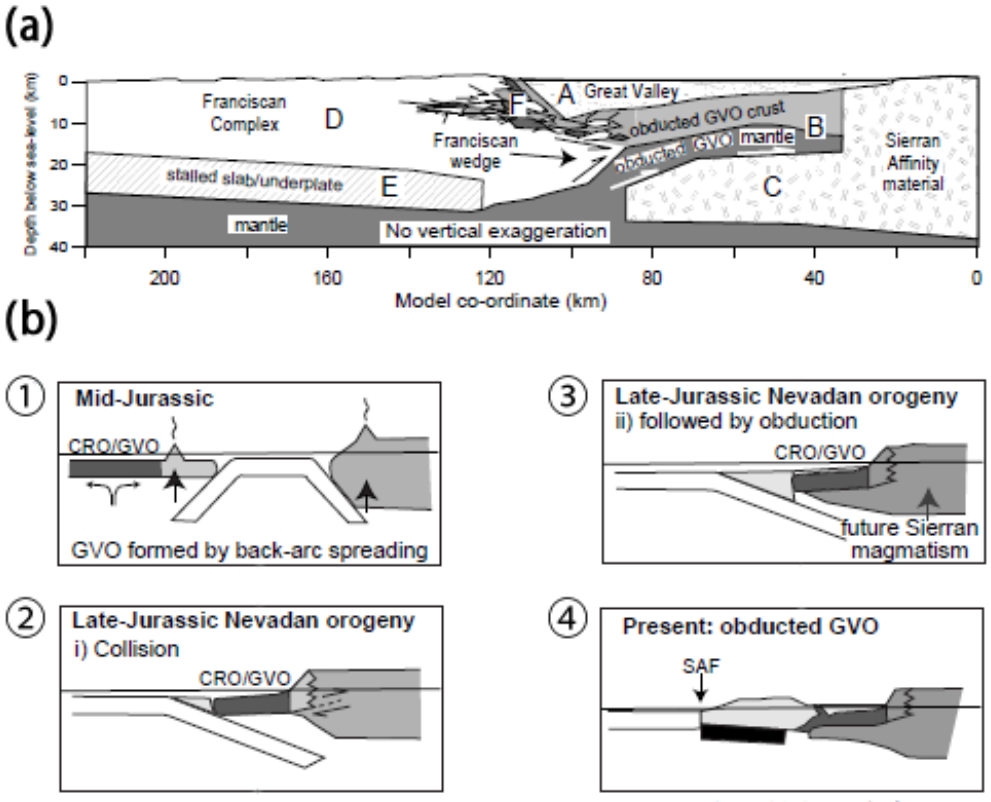

Figure 4.2: (a) Crustal structure of northern Great Valley interpreted from seismic refraction and gravity data. GVO, Great Valley ophiolite. (b) Tectonic development of the western margin of North America. CRO, Coast Range ophiolite. From Godfrey et at. (1997).

Figure 4.2(a) shows northern Great Valley crustal structure interpreted from seismic refraction and gravity data (Godfrey et al., 1997). In their interpretation, the western part of the Great Valley has a thick sedimentary layer over Great Valley Ophiolite and the eastern part of the

Great Valley has the Ophiolite on top of the rocks of Sierran affinity. As mentioned in chapter 1, Great Valley Ophiolite is a remnant of oceanic crust from Mid Jurassic back-arc spreading that collided into the western margin of North America (figure 4.2(b)), and the low-velocity layer observed below the Great Valley Ophiolite has been interpreted as a result of the Ophiolite thrusting over the rocks of the Sierran affinity. Figure 4.3 shows a cross section interpreted from a gravity profile across the southern San Joaquin Valley (Griscom and Jachens, 1990), and a similar low-velocity layer is modeled below the Great Valley Ophiolite at the eastern side of the valley. The receiver function result from this study provides additional evidence from seismic data that such a crustal structure similar to the northern Great Valley is present in the southern Great Valley. Receiver function results show that Moho depth at the eastern Great Valley suddenly gets very shallow. This transition into shallow Moho corresponds to the location where the Great Valley Ophiolite thrusts over the low-velocity layer.

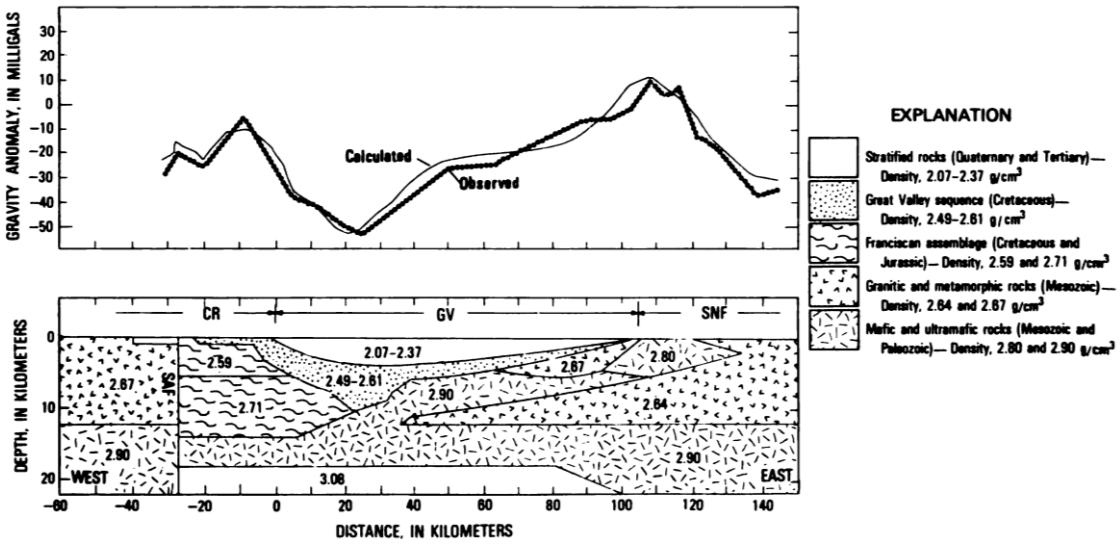

Figure 4.3: Cross section interpretation from gravity profile at San Joaquin Valley. From Griscom and Jachens (1990). CR, Coast Ranges. GV, Great Valley. SNF, Sierra Nevada foothills.

In the Sierra Nevada region, the crustal thickness increases again, with maximum thickness over 43 km. No P-to-S converted phase could be observed from stations in the northwestern Sierra Nevada, and the crustal thickness for that area could not be constrained.

Chapter5; Tomographic and Receiver Function Analysis of the Isabella Anomaly

Isabella Anomaly and Tomography

As mentioned in Chapter 2 the existence of the Isabella high-velocity anomaly is well known. Here I use tomography and mantle receiver function arrivals to test whether it could have the shape and velocity contrast of a stalled slab. A simple tomography model was made in order to image the Isabella anomaly with the newly installed FlexiRamp and permanent stations. The tau-p method for calculating travel-time (Buland and Chapman, 1983) was used in the residual time calculation to subtract the theoretical travel-times from observed times. Then I calculated the residual time difference between all the stations and one reference station. Station B075 of the permanent borehole network was chosen as the reference station. The deconvolution technique used in the receiver function study was applied to find the residual time differences. The timing of the maximum value of the resulting function from deconvolution of the vertical component of the

reference station seismogram from the vertical component of the target station seismogram represents the residual time difference of the two stations. Calculated arrival-time residuals were then separated into categories of ray parameter and back azimuth groups. Residual times greater than 1.2 times the standard deviation in each group were eliminated to account for noisy data in the deconvolution.

Figure 5.1 shows the results from the station PHL and RCT, where the arrival-time residuals are plotted against back azimuth. Each color represents different ray parameters where red, green, magenta, and blue correspond to the ray parameters of 0.04-0.08 s/km in increasing order. The lower the ray parameter the steeper the incident angle of the ray, so the red color data represent the steepest incident rays. Station PHL represents a typical result from near the coast stations, and the average arrival-time differences from different ray parameter and back azimuth ranges do not get larger than ±0.17 sec. Also, there are no recognizable variations in the arrival-time difference with different ray parameters and back azimuth implying that there is no tomographic anomaly beneath the region.

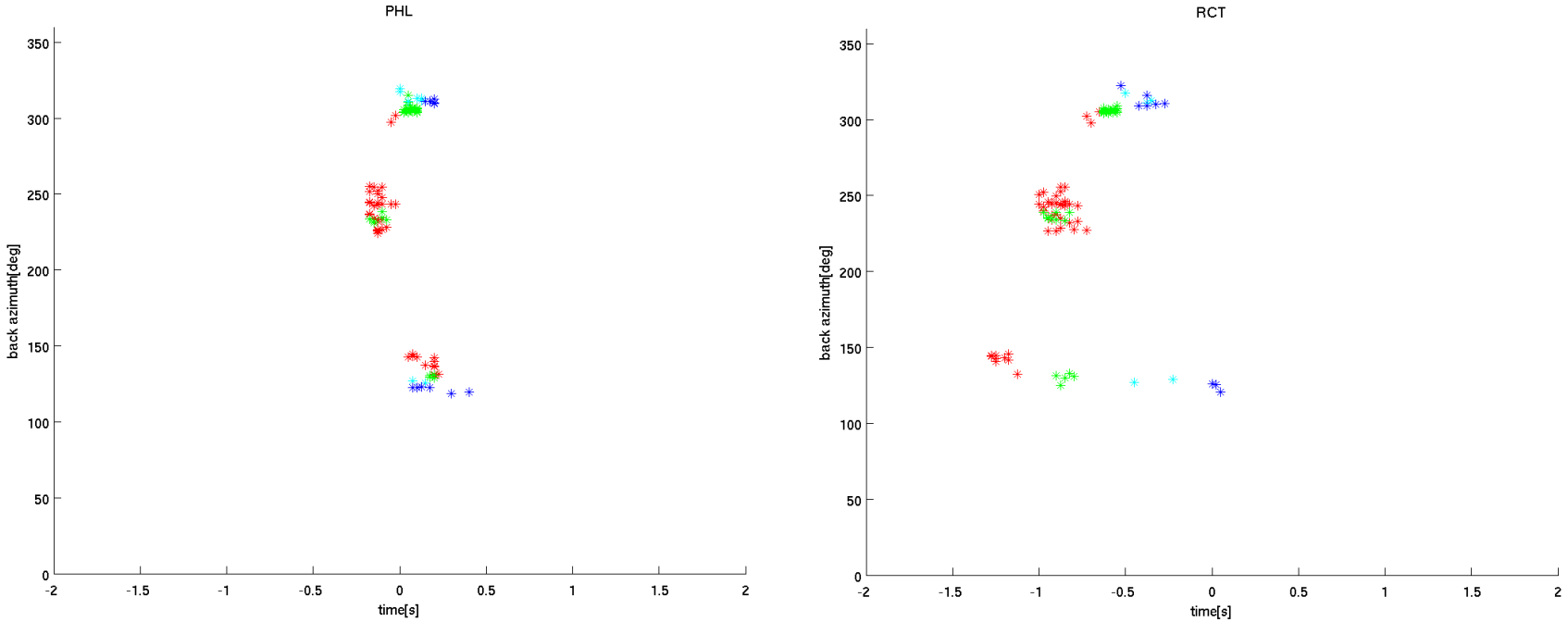

Figure 5.1: Difference in arrival time residuals from different back azimuths and ray parameters for station PHL and RCT. Y axis corresponds to difference in back azimuth and difference in color represents change in ray parameters. Red, 0.04-0.05 s/km; Green, 0.05-0.06 s/km; Magenta, 0.06-0.07 s/km; Blue,

Therefore the result from the plot suggests that crustal and sub-crustal structure near the coast (PHL) is similar to that near the San Andreas fault (B075). In contrast, station RCT is located over where the Isabella anomaly has been observed (Wang et al., 2013), and the plot shows a very different behavior compared with that of station PHL. The average arrival-time residual is -0.6 sec, and it is a lot earlier compared with other stations. Moreover, a clear pattern can be seen in arrival-time variation for the rays coming-in from back azimuths of 100º to 150º, where the steeply incoming rays (red) with small angles of incidence arrive faster than incoming rays (blue) with large angle of incidence.

Tomography residual maps are shown in figure 5.2 to visualize the relative arrival-times. Here, an average residual time for each ray parameter and back azimuth group is plotted separately in ten maps. A color scale is shown at the bottom where blue and red colors represent earlier and later arrivals relative to station B075. The stations are irregularly located so the data interpolation is not an accurate representation of the area; however, a strong negative arrival-time (blue) anomaly between the Great Valley and Sierra Nevada caused by the Isabella anomaly is clearly present. Interestingly

the negative arrival-time anomaly is strongest in the Great Valley where a positive anomaly was expected from the slow-velocity sedimentary basin, and it reveals the strength of the negative arrival anomaly from the Isabella anomaly deeper in the mantle.

A pattern can be seen in the tomography plots by comparing a range of back azimuth groups for different ray parameters. Looking at the tomography plot for 100º-150º back azimuth group, the center of the negative arrival anomaly shifts away to the opposite direction of the incident ray (northwest) with increasing ray parameters (figure 5.2). The same thing happens for other groups. With increasing ray parameters, the center of the anomaly shifts away to northeast for the 200º-250º back azimuth group and to southeast for the 280º-330º back azimuth group.

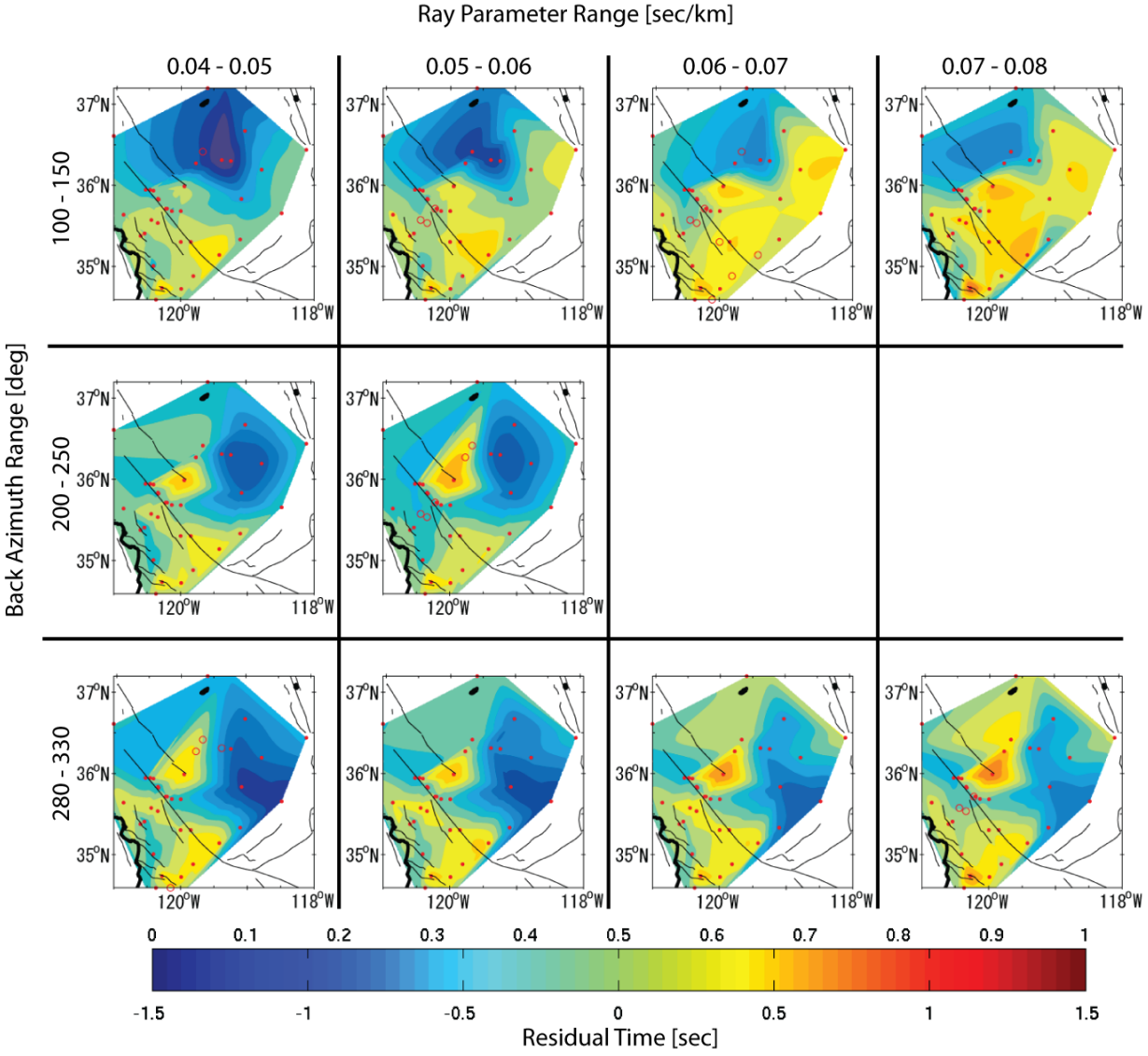

Figure 5.2: Contour maps of arrival time residual. Ten different contour maps show the result from different ranges of ray parameter and back azimuth. Station locations are plotted as red dots (red open circles are used for stations with no data for particular ranges). Coast of California is shown in thick black line, and faults are plotted as thin black lines.

The difference in the ray parameters represents the change in the incident angle; however, the difference in their ray path is too small within the crust to cause this large shift, confirming that the anomaly is located in the mantle. The locations of the anomaly for the steepest incident ray (the lowest ray parameter) from different back azimuth groups are nearly the same, and the "shifting away" of the anomaly can be seen with increasing ray parameter for each back azimuth group. This implies that the center of the anomaly is below the common anomaly location inferred from the low ray parameter tomography maps.

In order to model the location and the shape of the Isabella anomaly, a dipping rectangular block model was constructed to replicate the observed residual time pattern. The model consists of two parts, a deep mantle structure and a shallow structure. The deep structure model is constrained by a rectangular block, and it is adjusted to explain the residual time variation observed from different ray parameter and back azimuth groups. Then the shallow structure was used to model residual times as station time-term that do not vary from differences in ray parameter and back azimuth. A rectangular block was chosen for the deep model because a laterally long geometry is

required to generate the strength of the observed anomaly. Station RCT, for example, has residual time larger than -1.3 sec (figure 5.1). If the P-wave velocity in the Isabella anomaly is about 5% faster than the surrounding mantle (Jones et al., 1994; Raikes 1976), the -1.3 sec residuals observed in station RCT requires the rays to penetrate over 200 km through the anomaly. Therefore a dipping rectangular block is chosen for its simplicity in geometry and for its flexibility in both horizontal and vertical dimensions and to test the slab hypothesis.

The model residuals were compared with the data using least squares inversion, where the best-fitting model was obtained by minimizing the sum of squares *ssq* between the relative travel-time from data *RTd(st,rp,bz)* and the relative travel-time from the model *RTm(st,rp,bz)*. The equation can be written as the following;

$$\mathrm{ssq} = \sum(RTd(st,rp,bz) - RTm(st,rp,bz))^2 \quad . \qquad (5.1)$$

Here, the *st* stands for stations, *rp* stands for ray parameter range, and *bz* stands for back azimuth range. Out of 41 stations, one station was

used as a reference and 3 stations did not have data to compare with the reference station, so the size of the *st* is 37. Ray parameters were separated into 4 ranges: 0.04-0.05 s/km, 0.05-0.06 s/km, 0.06-0.07s/km, 0.07-0.08 s/km. Then the back azimuth was separated into 3 ranges: 100-150º, 200-250º, 280-330º. Therefore *st*, *rp* and *bz* each represents 37, 3 and 4 rows of vector, and *RTd* and *RTm* is both 37 by 3 by 4 matrix. The residual time for the model was calculated as the following;

$$RTm(st, rp, bz) = dTrec(st, rp, bz) + dTst(st) \quad . \qquad (5.2)$$

dTst(st) is the station time-term associated with the shallow crustal structure that does not depend on *rp* or *bz*. *dTrec(st,rp,bz)* is the time difference term caused by the deep structure. The goal is to find the location and geometry of the rectangular block that best satisfies the variation of *RTd*. It was obtained by back tracing the rays to see the difference in the travel-time within and without the block, where the location and geometry property of the block was controlled by 9 parameters [Latitude, Longitude, Length, Thickness, Dip, Strike, Depth-1, Depth-2, and Velocity] as shown in figure 5.3.

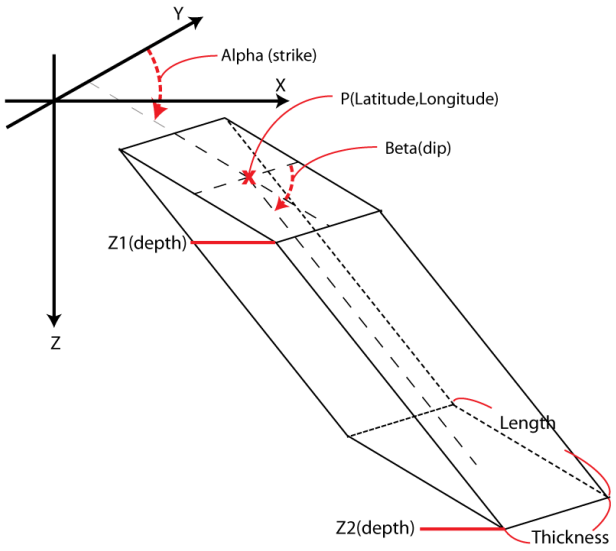

Figure 5.3: Rectangular block model showing the geometric parameters.

Table 5.1 shows the result. The rectangular block (figure 5.3) extends from 49 km to 460 km depth, and the location of the top surface of the block corresponds to 10~20 km below the Moho. The 98 km thick block is dipping (Beta) 64º towards northeast, and the strike (Alpha) direction corresponds to the strike of the Coast and the Sierra Nevada.

Table 5-1: Model parameter result after least squares inversion and its standard deviation. Z2 was not constrained well because of the lack of station coverage towards the east.

P1(Latitude)	P2(Longitude)	Length(km)	Thickness(km)	
35.84±0.02	-119.61±0.03	136±3	98±2	
Z1(km)	Z2(km)	Alpha(degree)	Beta(degree)	Vp (%)
49±1	460	138.8±0.7	63.7±0.5	4.5±0.2

Isabella Anomaly and Receiver Functions

If the high-velocity contrast observed in the Isabella anomaly is due to a subducted fossil slab, a possible source of the high-velocity anomaly is a combination of dehydration and cooler temperatures of oceanic lithosphere (Wang et al., 2013). In such a case, the shallower part of the subducted slab with smaller temperature contrasts cannot be easily recognized in the tomography as it will not generate *RTd(st,rp,bz)*. However, receiver functions which can detect layer contrasts such as oceanic crust may resolve the contrast. In order to test the hypothesis of Wang et al. (2013), receiver functions were used to test whether the Monterey micro-plate can be connected with the location of the Isabella anomaly obtained in the tomography data.

Identifying a subducted slab using receiver functions requires a structural knowledge of whether the slab is a high-velocity zone or a low-velocity zone. Seismic reflection studies have been used to infer a high-velocity layer at the lower crust near San Luis Obispo, suggesting that the partially subducted Monterey micro-plate has been coupled to the Pacific plate (Miller et al., 1992; Brocher et al., 1999; ten Brink et al., 1999). My

receiver function study (Chapter 4) instead shows a low-velocity layer at the lower crust near the San Andreas fault also seen by Ozacar and Zandt (2010), suggesting that the slab is not coupled to the Pacific plate at that location. Receiver functions from the Coast Ranges stations closer to the coast (PHL, SMR, RAMR) are in agreement with the result shown by Ozacar and Zandt (2010), and I interpreted this as evidence that the subducted Monterey micro-plate is not attached to the Salinian block of the Pacific plate.

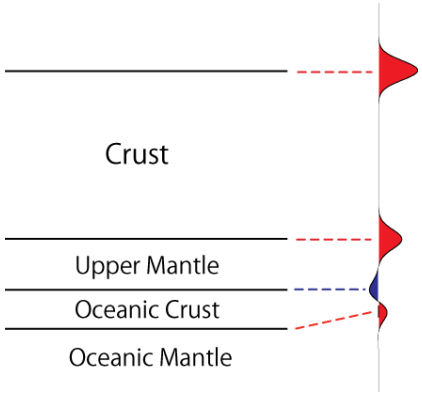

Figure 5.4: (Left) Model of Monterey micro-plate (oceanic crust and oceanic mantle) beneath the Continental crust. (right) Synthetic receiver functions showing a negative-positive dipole signal that would be generated by oceanic crust below the Moho.

Figure 5.4 shows the model where Monterey micro-plate is detached from Salinian block. Here, the Monterey oceanic crust is overlain by the Salinian block mantle and underlain by the Monterey micro-plate mantle. A negative signal from the top of Oceanic crust and a positive signal from the bottom of the Oceanic crust are expected in the receiver functions (figure 5.4) because the Oceanic crust is a low-velocity layer between high-velocity mantle materials. Therefore a negative-positive dipole signal is expected to be seen underneath the Moho (Campos et al., 2008) below the Salinian block. If the subducted Monterey micro-plate connects to the Isabella anomaly east of the San Andreas fault, the negative-positive dipole signal is expected to align in receiver functions plot, tracing the subducted slab down to the Isabella anomaly.

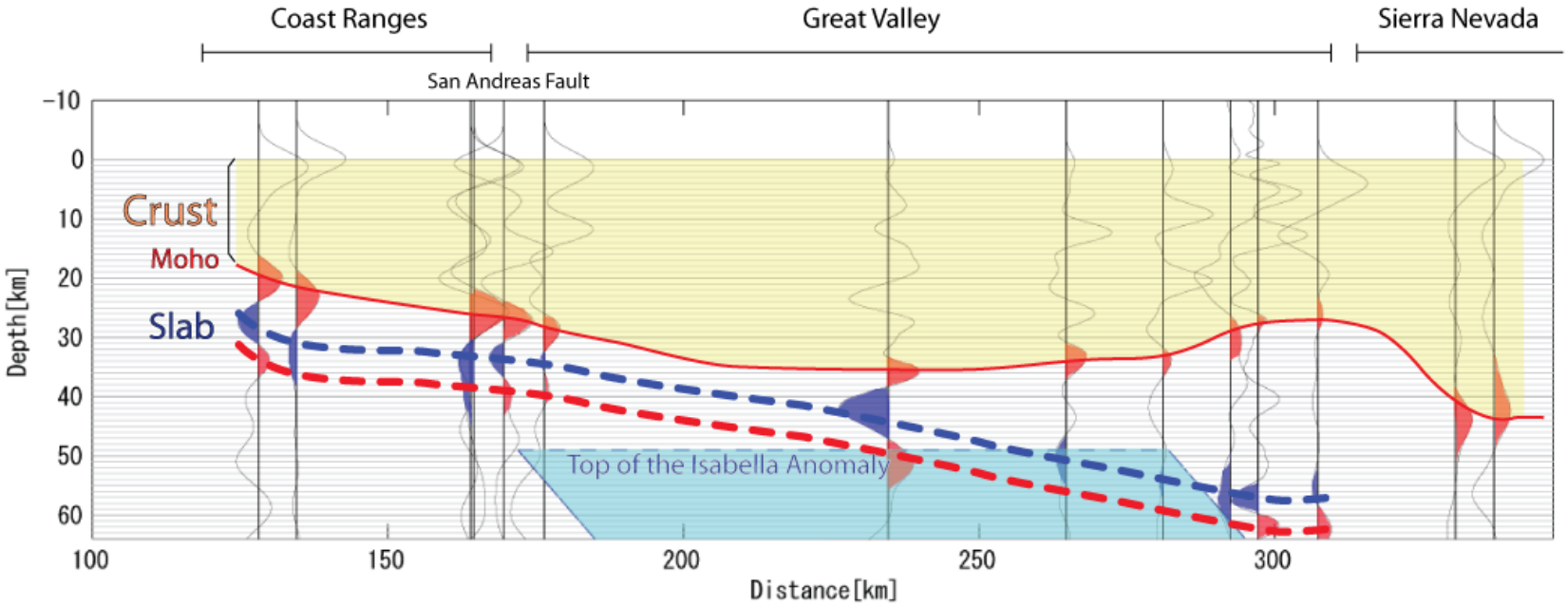

Figure 5.5: Interpretation of the sub-crustal structure from the receiver functions. The receiver functions are transformed from time-domain to depth-domain using crustal structure for each location (table 3.3) and an average mantle velocity structure. Moho boundary is marked as a red line. Interpretation of receiver function signal from the top of the Monterey fossil slab is marked by blue and red dashed line. The blue block below the slab is the result from the tomography (table 5.1).

Figure 5.5 shows the sub-crustal structure interpreted from receiver functions. Receiver functions are now transformed into the depth-domain, and the rectangular box model of the Isabella anomaly from the above tomography study is superposed over the receiver function plot. In order to plot the receiver functions in the depth-domain, an average crustal structure for individual stations described in table 3.3 and a uniform mantle structure were used. The red line going through a positive signal in each receiver function shows the base of the crust as described in the previous chapter. Just below the Moho, a negative signal can be observed, and it is marked by a blue dotted line. The blue line is gently dipping toward the east, and it is continuous from the coast to the top of the Isabella anomaly. This negative signal is interpreted as a P-to-S converted phase from the subducted oceanic crust of the Monterey micro-plate. Many of the negative signals are followed by an 8 to 10 km deeper positive signal making it a negative-positive dipole. The distance between the negative and positive signals corresponds to the thickness of Oceanic crust; however, not all the stations were able to resolve the signal down to these depths.

The location of the fossil slab interpreted from the receiver functions

lies 10 to 20 km below the Moho, and the top surface of the rectangular block model from the tomography matches the depth of the dipole signals in the receiver functions result (figure 5.5). The combined results of the receiver functions and tomography study suggests that the origin of the Isabella anomaly is a remnant of the Farallon plate, where the receiver functions define the western portion of a gently dipping slab, and the tomography defines the eastern portion of a steeply dipping slab.

The tomography model takes into account the western near-horizontal part of the slab which is absorbed into the time-terms of equation 5.2. Because it provides no lateral contrast, there is no azimuthal and ray parameter variation in the residual times and so its effect along with shallow basin structures are absorbed by the time-terms.

Chapter6; Conclusion

The origin of the Isabella tomographic anomaly has been interpreted as either a lithospheric delamination or a remnant of the Farallon plate attached to the Monterey micro-plate. The hypotheses were tested by constructing a tomographic model using newly installed stations and by tracing the partially subducted Monterey micro-plate with P-wave receiver functions.

A rectangular block tomographic model inverted to fit the Isabella anomaly dips 65º toward the northeast from 50 km depth with 100 km thickness, and the strike direction corresponds to the orientation of the Coast and the Sierra Nevada. Receiver functions detected P-to-S converted phases from the top of the oceanic crust below the Moho, and it could be traced down from the Coast Ranges to the Great Valley. P-to-S converted phases from the bottom of the Oceanic crust were expected to produce dipole signals, but not all the stations could detect them. However, for the ones detected the dipole signal resulted with the Oceanic crust thickness of 8 to 10 km.

Figure 6.1 shows the summary interpretation for the crustal and sub-crustal structures. The partially subducted Monterey micro-plate is located

near 30 km depth below the Coast Ranges and 50 km depth below the east Great Valley. Then the gently dipping slab abruptly increases its dip to near 65º beneath the Great Valley. For a young plate such as the Monterey micro-plate, lithospheric thickness is expected to be 50-70 km. The 100km thickness I find may be due to the over-simplified model.

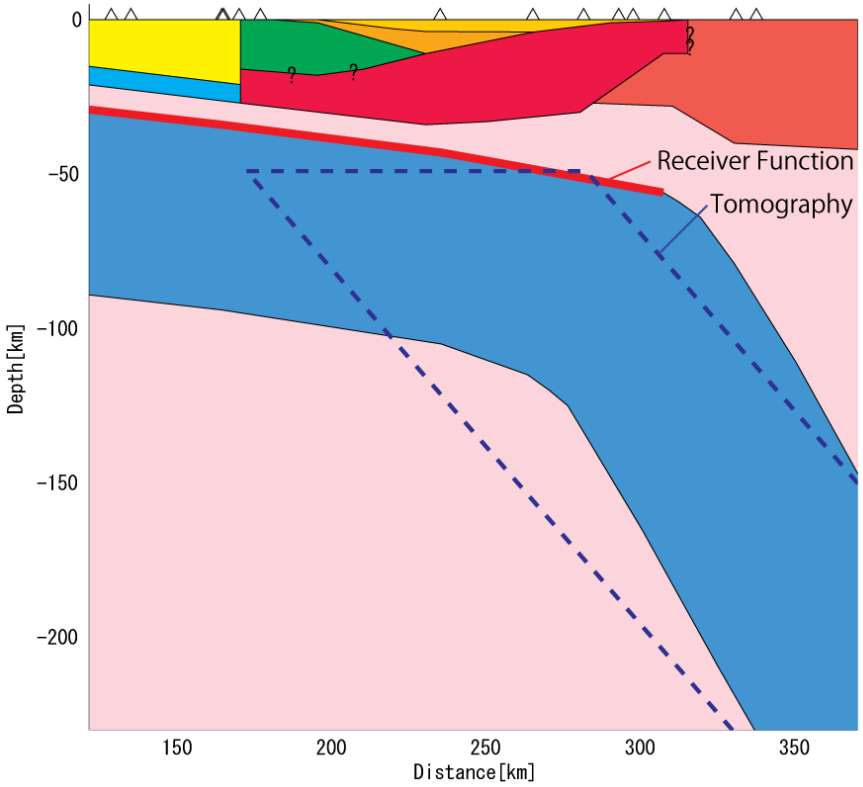

Figure 6.1: Cross section showing the summary of the interpretation. The red bold line is the Oceanic crust of the Monterey micro-plate interpreted from the receiver functions. The blue dotted line is the rectangular box model from the tomography inversion of the Isabella anomaly. Crustal structure is shown in figure 4.1, mantle material is shown in light pink and the 100 km thick blue slab is the interpretation of the Monterey fossil slab.

The depth of the Oceanic crust traced from the Coast Ranges matches the depth of the top surface of the rectangular box tomographic model below the Great Valley, and the results are consistent. The combined results of the receiver functions and tomography study suggests that the origin of the Isabella anomaly is a remnant of the Farallon plate, and that the initially low angle of subduction of the Farallon plate in the west increases its dip below the Great Valley to the east.

Appendix A

Gathers of receiver functions

The following are gathers of receiver functions. For each station, the top three plots shows receiver functions sort by ray parameter for three back azimuth ranges, and the bottom plot shows receiver functions sort by back azimuth. The location of the stations is shown in figure 3.1.

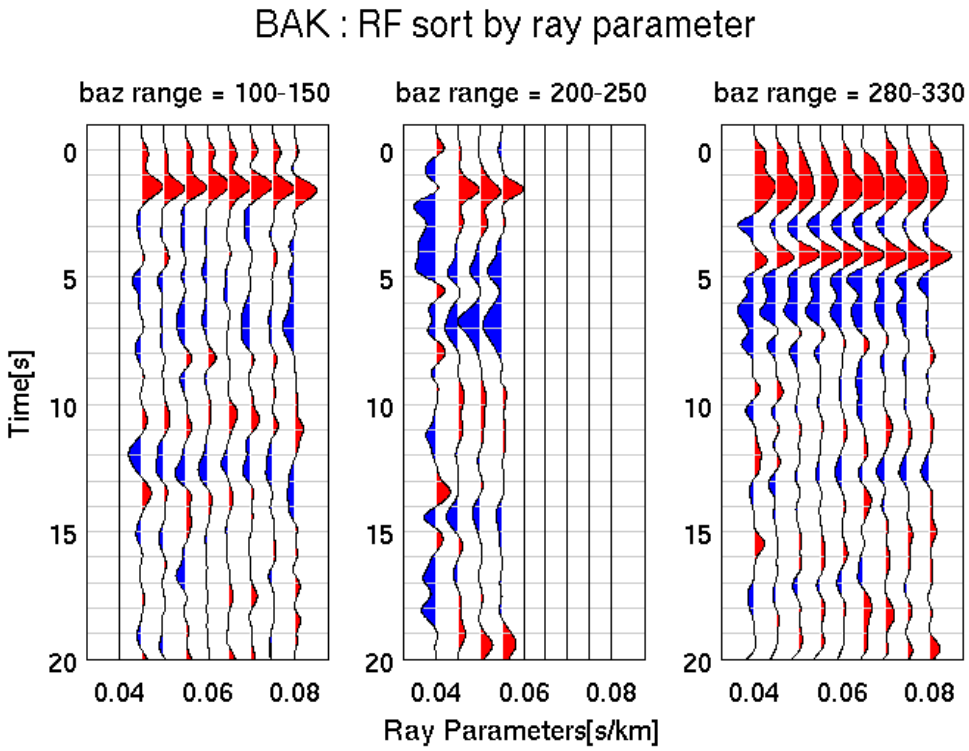
BAK : RF sort by ray parameter
baz range = 100-150
baz range = 200-250
baz range = 280-330
Time[s]
0
5
10
15
20
0.04
0.06
0.08
Ray Parameters[s/km]

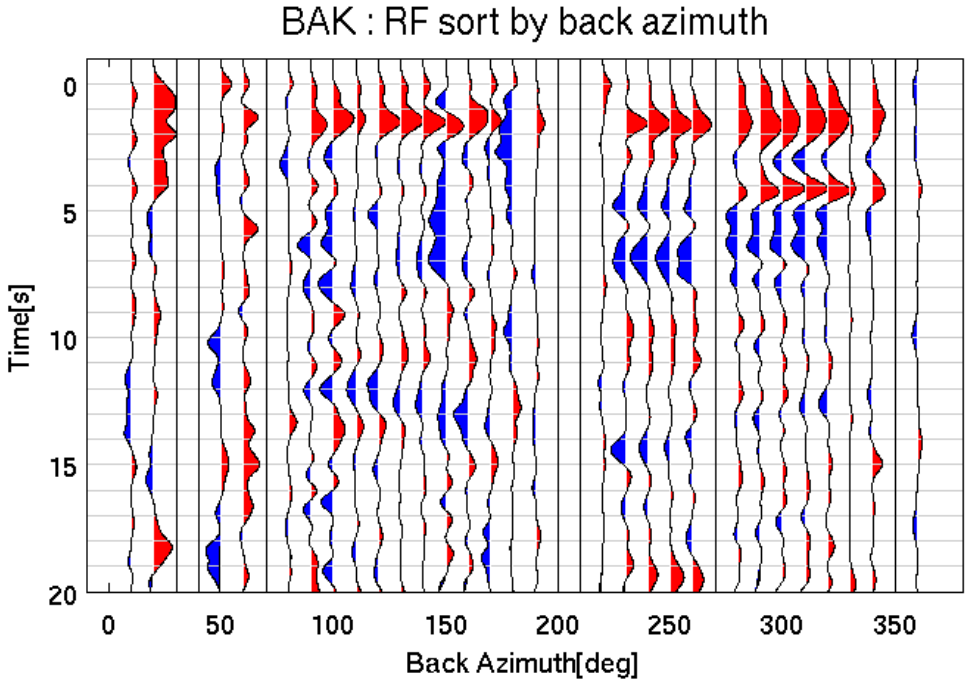
BAK : RF sort by back azimuth
Time[s]
0
5
10
15
20
0
50
100
150
200
250
300
350
Back Azimuth[deg]

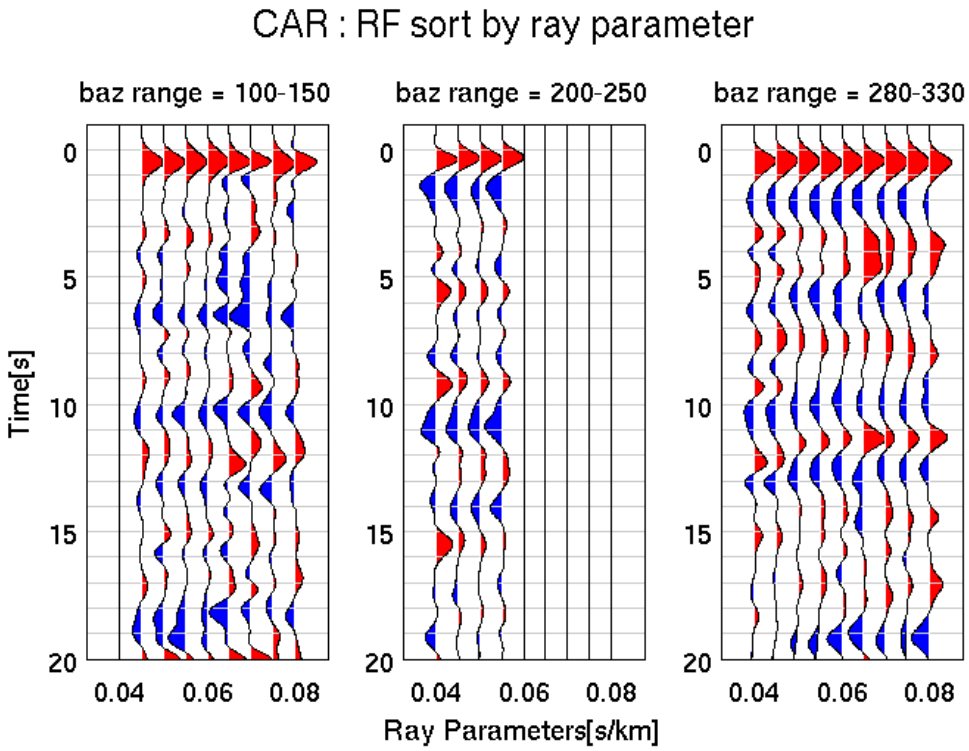
CAR : RF sort by ray parameter
baz range = 100-150
baz range = 200-250
baz range = 280-330
Time[s]
0
5
10
15
20
0.04
0.06
0.08
Ray Parameters[s/km]

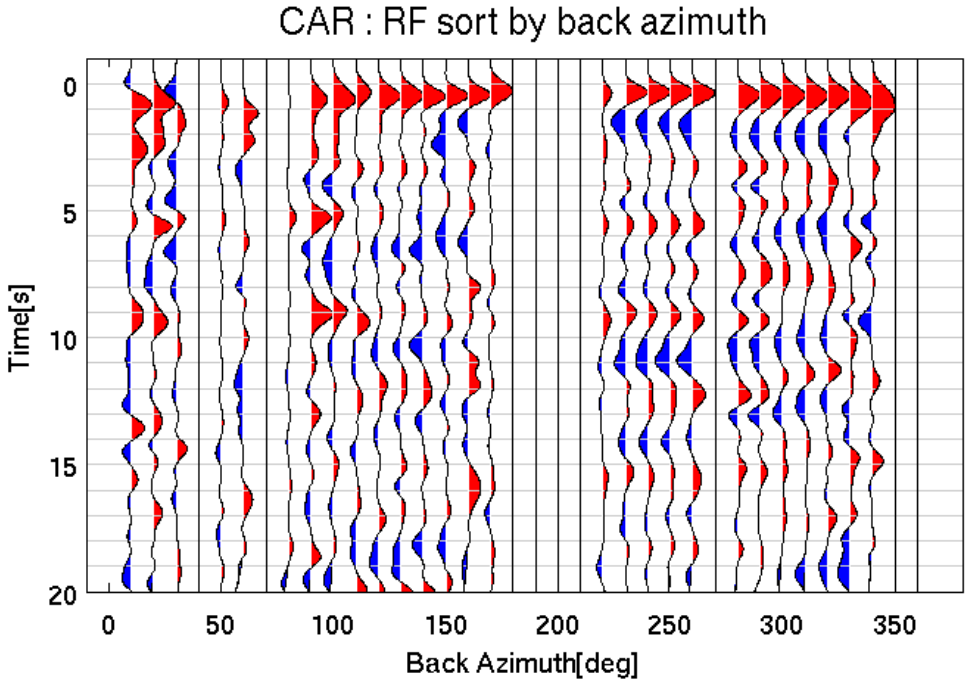
CAR : RF sort by back azimuth
Time[s]
0
5
10
15
20
0
50
100
150
200
250
300
350
Back Azimuth[deg]

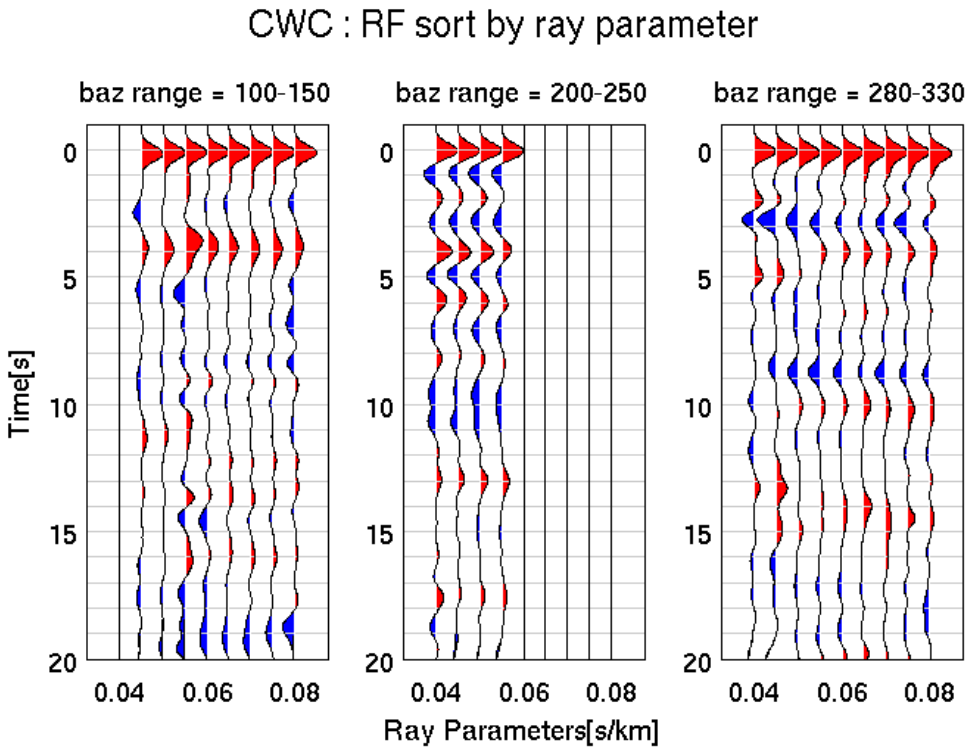
CWC : RF sort by ray parameter
baz range = 100-150
baz range = 200-250
baz range = 280-330
Time[s]
0
5
10
15
20
0.04
0.06
0.08
Ray Parameters[s/km]

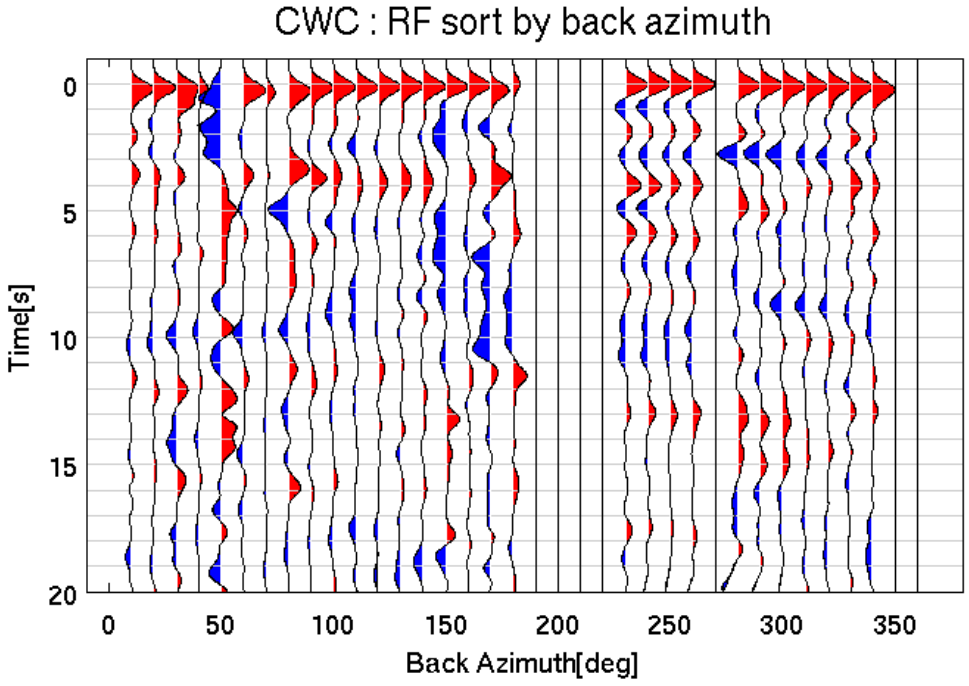
CWC : RF sort by back azimuth
Time[s]
0
5
10
15
20
0
50
100
150
200
250
300
350
Back Azimuth[deg]

FIG : RF sort by ray parameter

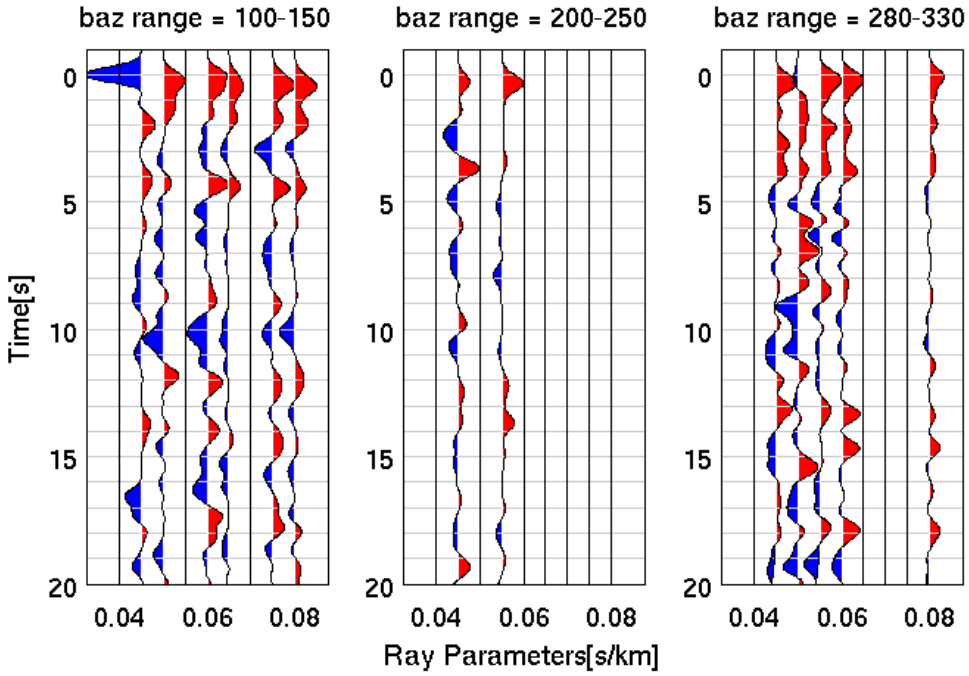

FIG : RF sort by back azimuth

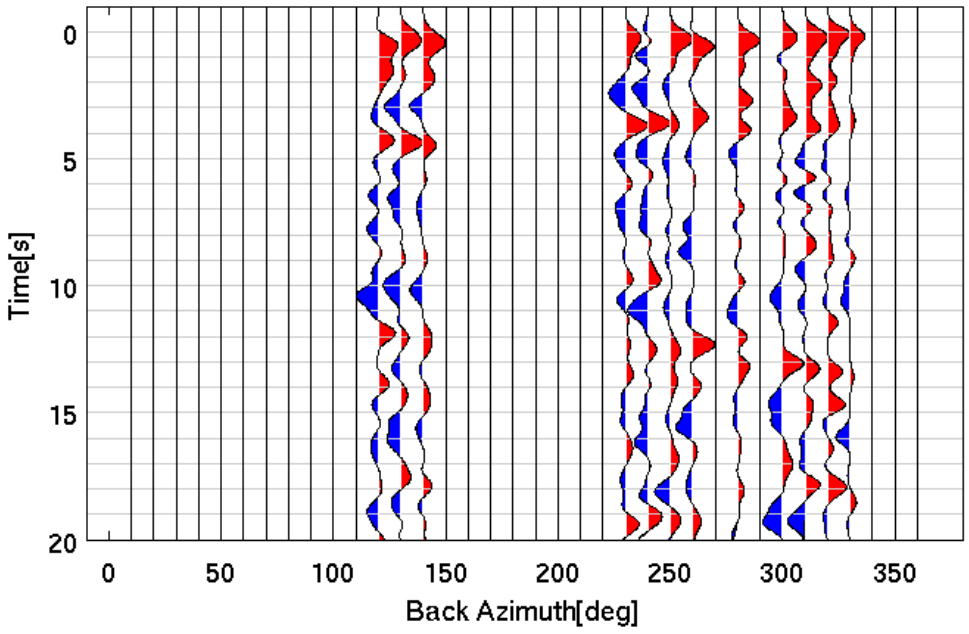

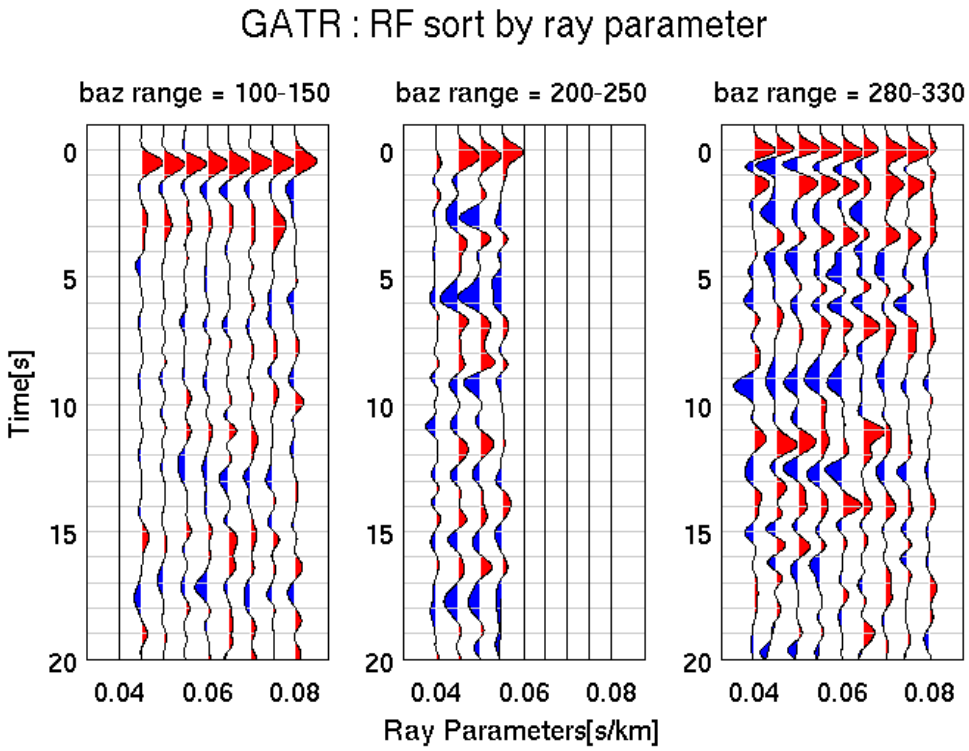
GATR : RF sort by ray parameter
baz range = 100-150
baz range = 200-250
baz range = 280-330
Time[s]
0
5
10
15
20
0.04
0.06
0.08
Ray Parameters[s/km]

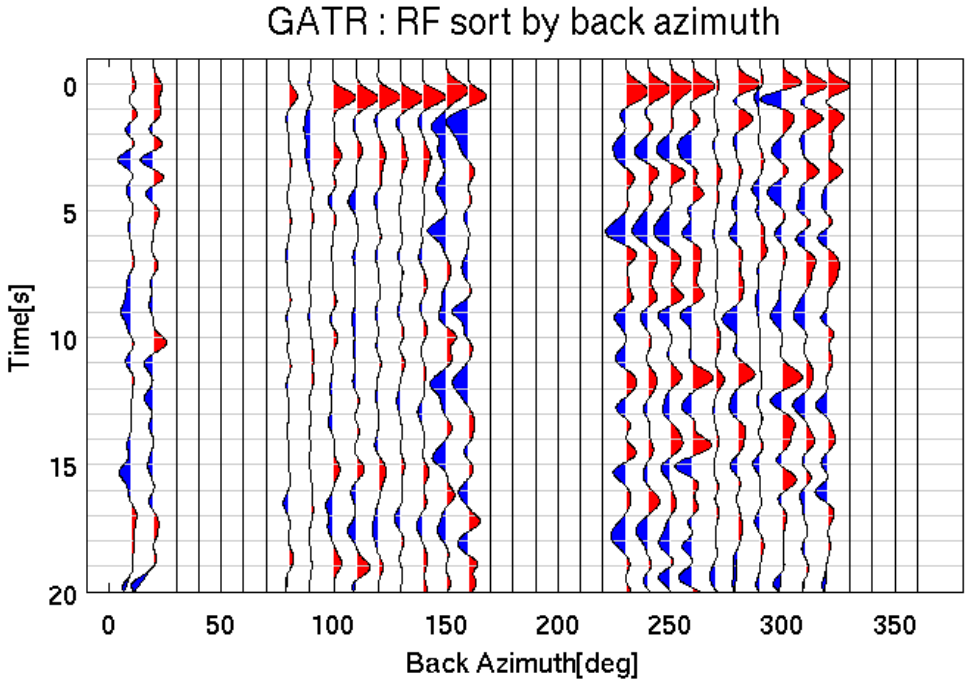
GATR : RF sort by back azimuth
Time[s]
0
5
10
15
20
0
50
100
150
200
250
300
350
Back Azimuth[deg]

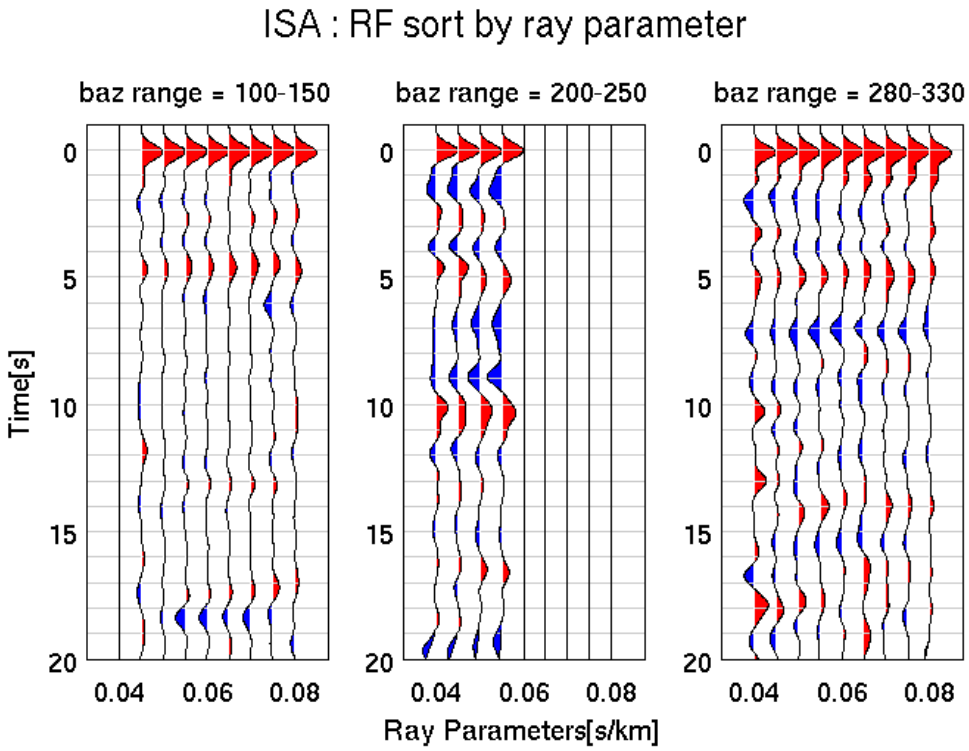
ISA : RF sort by ray parameter
baz range = 100-150
baz range = 200-250
baz range = 280-330
Time[s]
0
5
10
15
20
0.04
0.06
0.08
Ray Parameters[s/km]

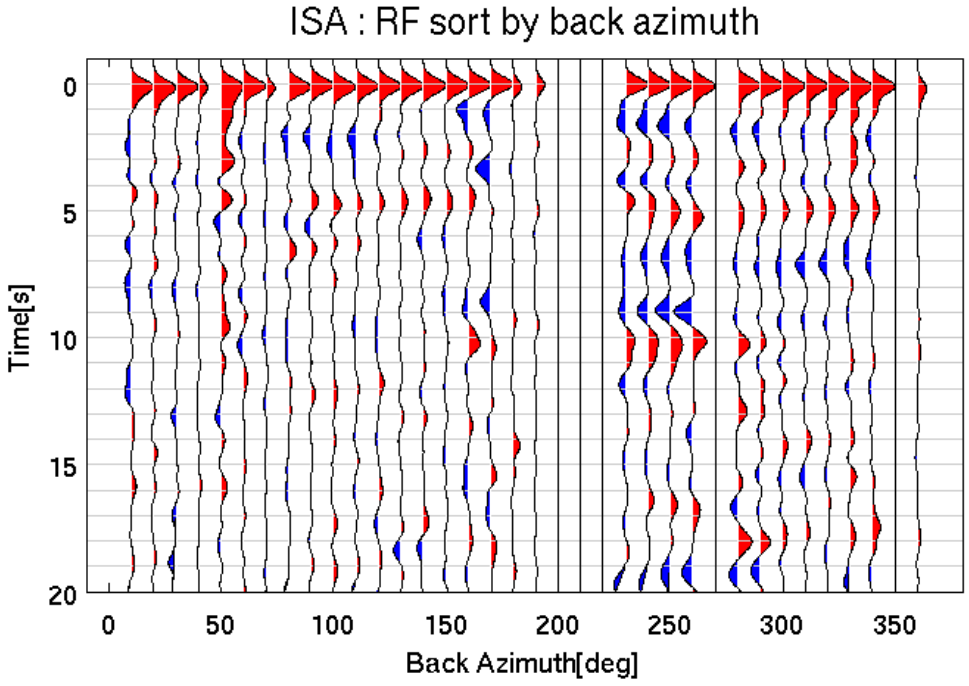
ISA : RF sort by back azimuth
Time[s]
0
5
10
15
20
0
50
100
150
200
250
300
350
Back Azimuth[deg]

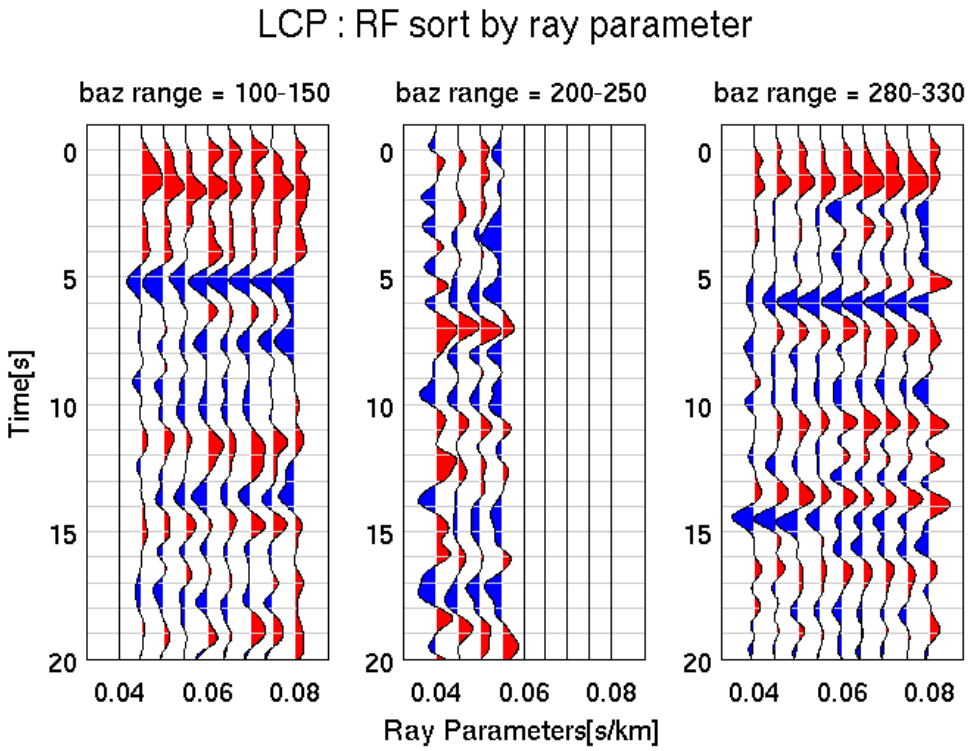
LCP : RF sort by ray parameter
baz range = 100-150
baz range = 200-250
baz range = 280-330
Time[s]
0
5
10
15
20
0.04
0.06
0.08
Ray Parameters[s/km]

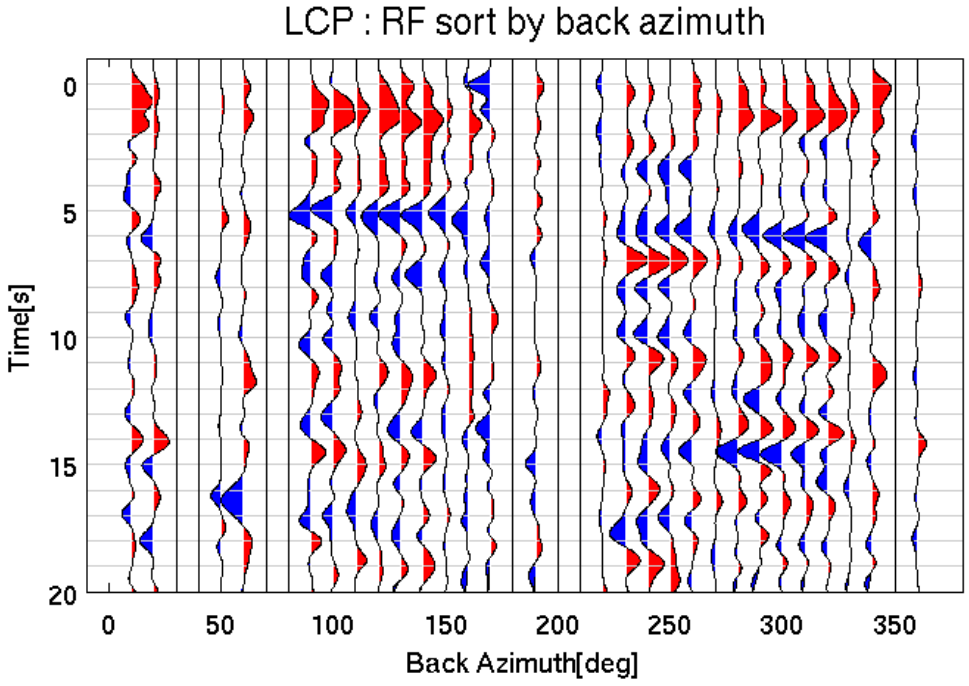
LCP : RF sort by back azimuth
Time[s]
0
5
10
15
20
0
50
100
150
200
250
300
350
Back Azimuth[deg]

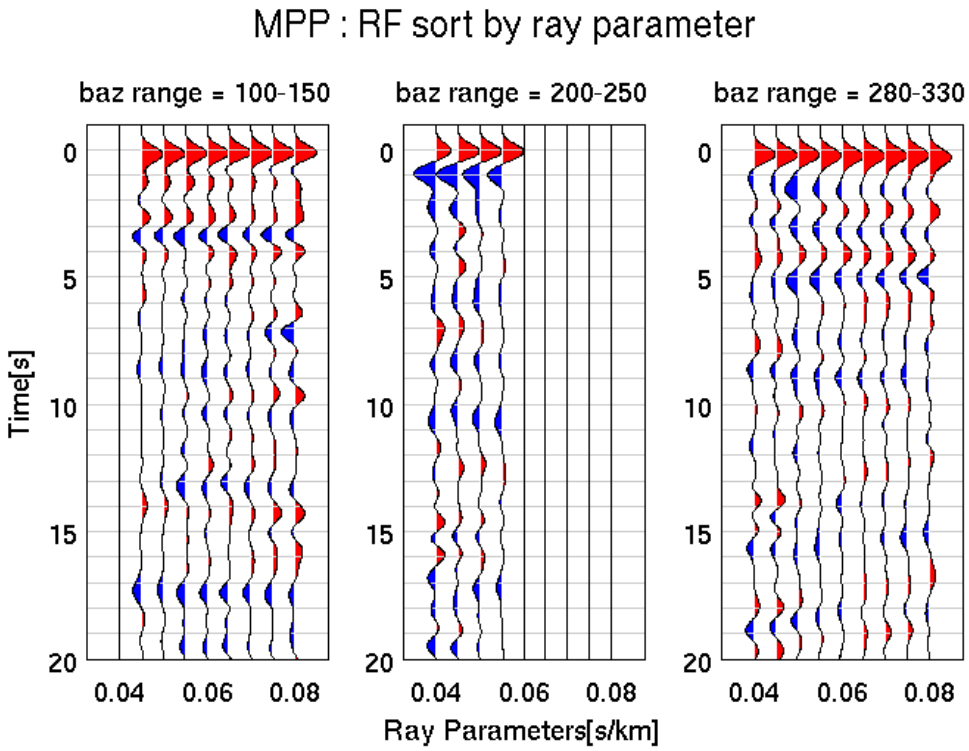
MPP : RF sort by ray parameter
baz range = 100-150
baz range = 200-250
baz range = 280-330
Time[s]
0
5
10
15
20
0.04
0.06
0.08
Ray Parameters[s/km]

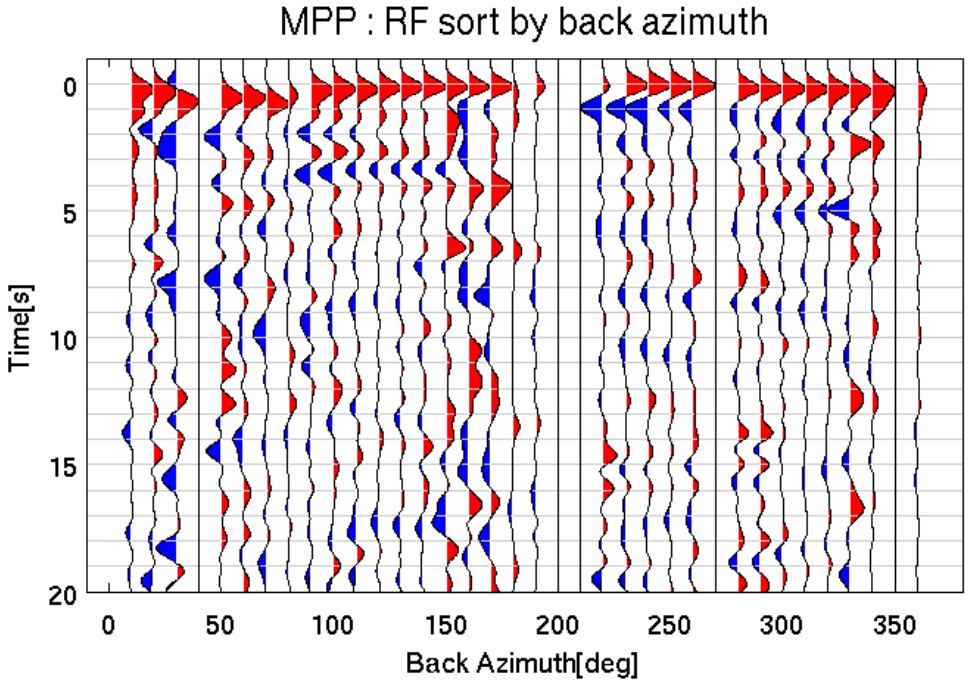
MPP : RF sort by back azimuth
Time[s]
0
5
10
15
20
0
50
100
150
200
250
300
350
Back Azimuth[deg]

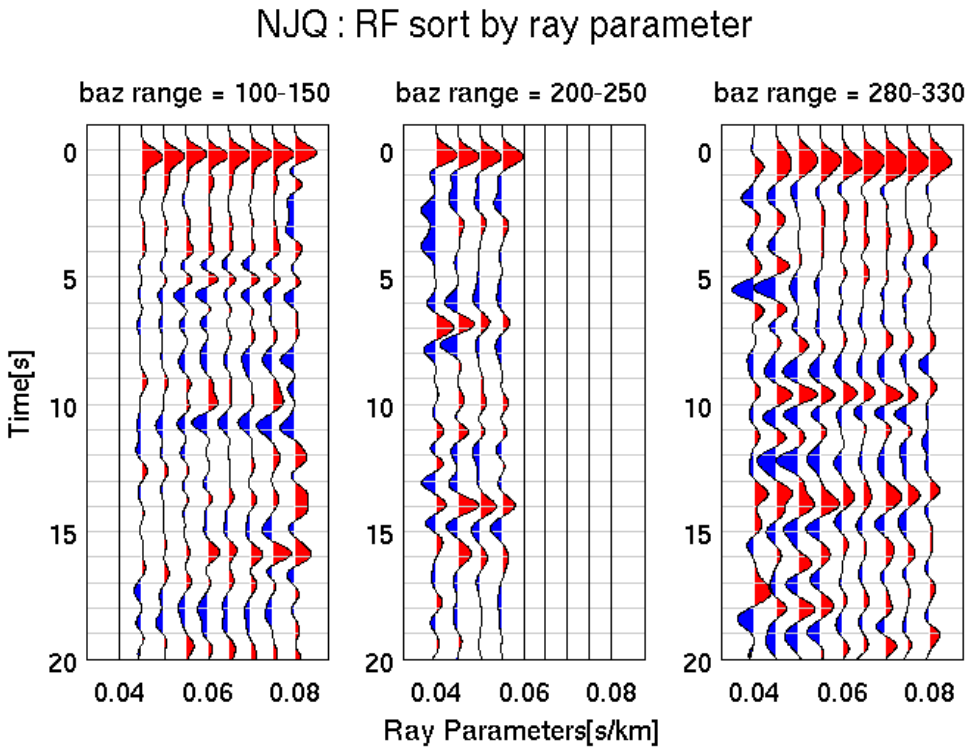
NJQ : RF sort by ray parameter
baz range = 100-150
baz range = 200-250
baz range = 280-330
Time[s]
0
5
10
15
20
0.04
0.06
0.08
Ray Parameters[s/km]

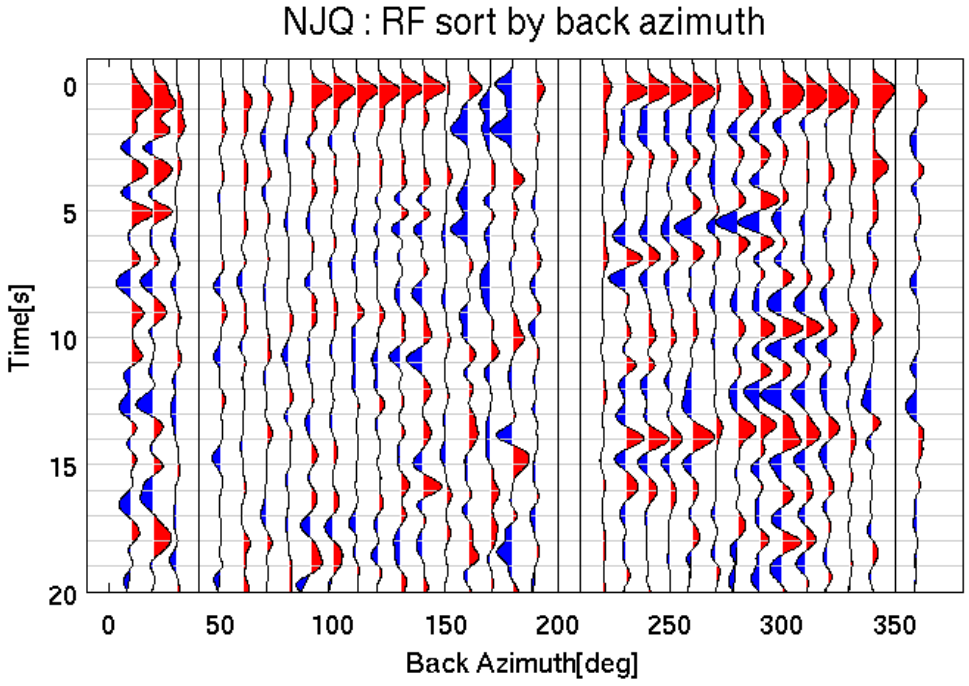
NJQ : RF sort by back azimuth
Time[s]
0
5
10
15
20
0
50
100
150
200
250
300
350
Back Azimuth[deg]

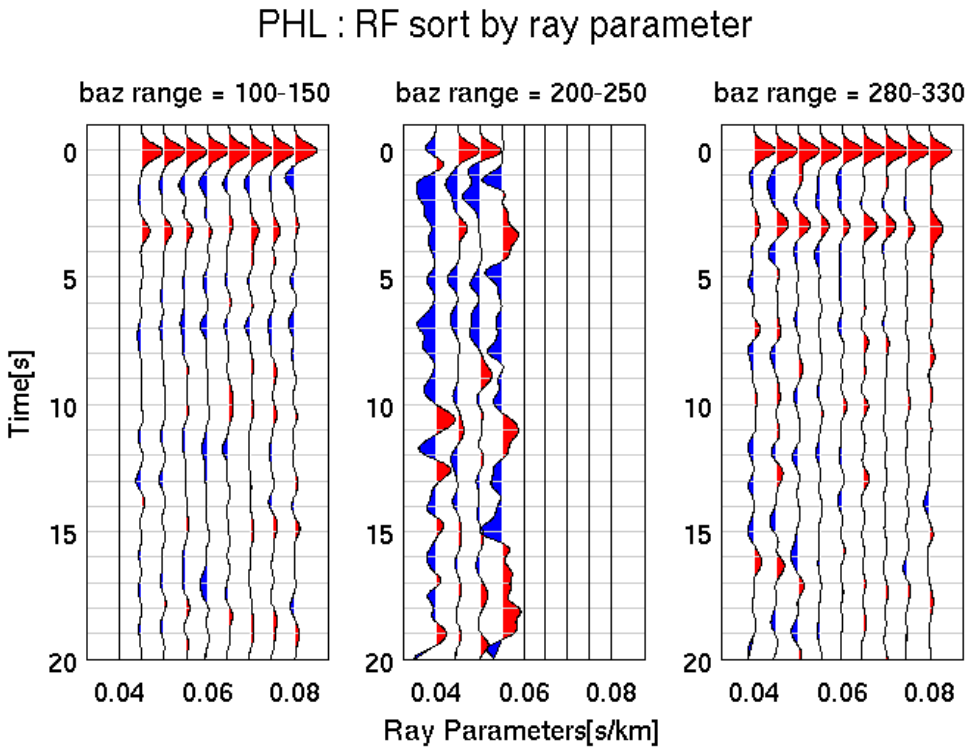
PHL : RF sort by ray parameter
baz range = 100-150
baz range = 200-250
baz range = 280-330
Time[s]
0
5
10
15
20
0.04
0.06
0.08
Ray Parameters[s/km]

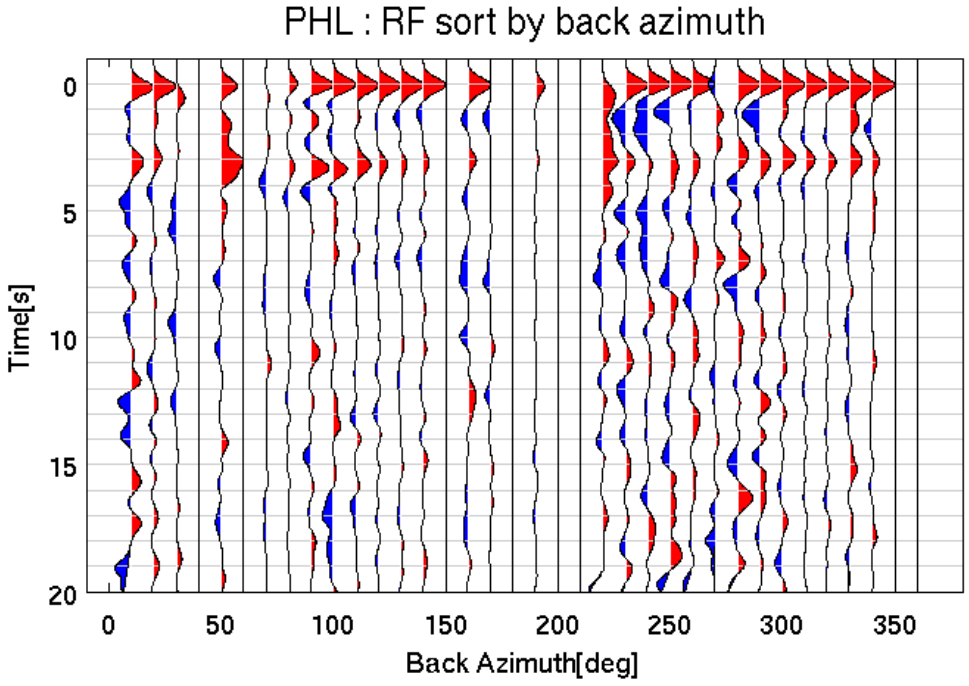
PHL : RF sort by back azimuth
Time[s]
0
5
10
15
20
0
50
100
150
200
250
300
350
Back Azimuth[deg]

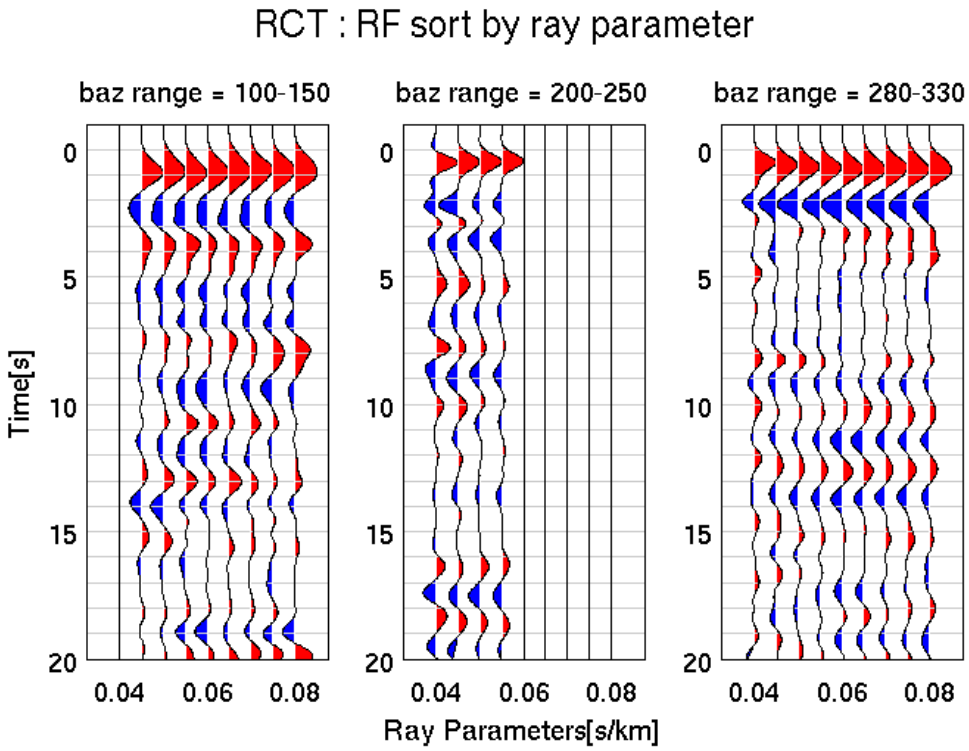
RCT : RF sort by ray parameter
baz range = 100-150
baz range = 200-250
baz range = 280-330
Time[s]
0
5
10
15
20
0.04
0.06
0.08
Ray Parameters[s/km]

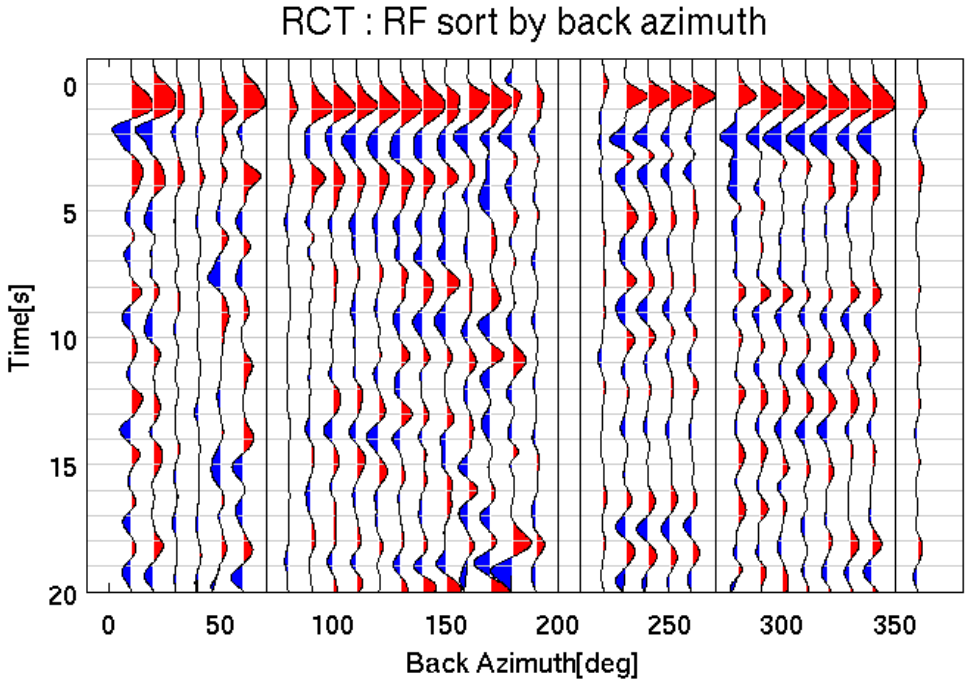
RCT : RF sort by back azimuth
Time[s]
0
5
10
15
20
0
50
100
150
200
250
300
350
Back Azimuth[deg]

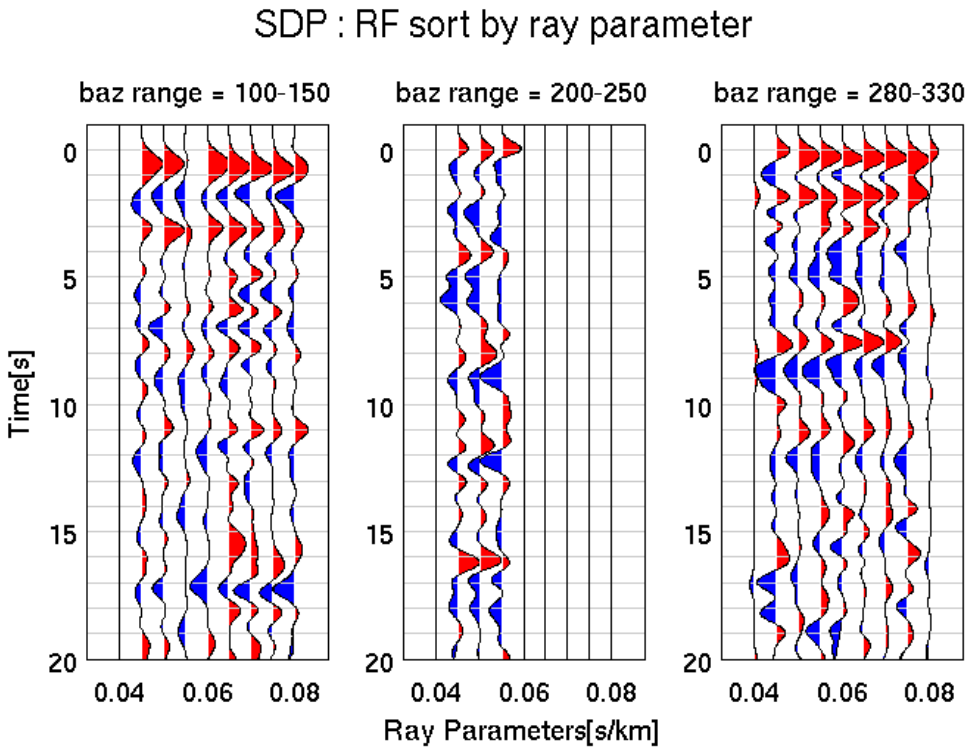
SDP : RF sort by ray parameter
baz range = 100-150
baz range = 200-250
baz range = 280-330
Time[s]
0
5
10
15
20
0.04
0.06
0.08
Ray Parameters[s/km]

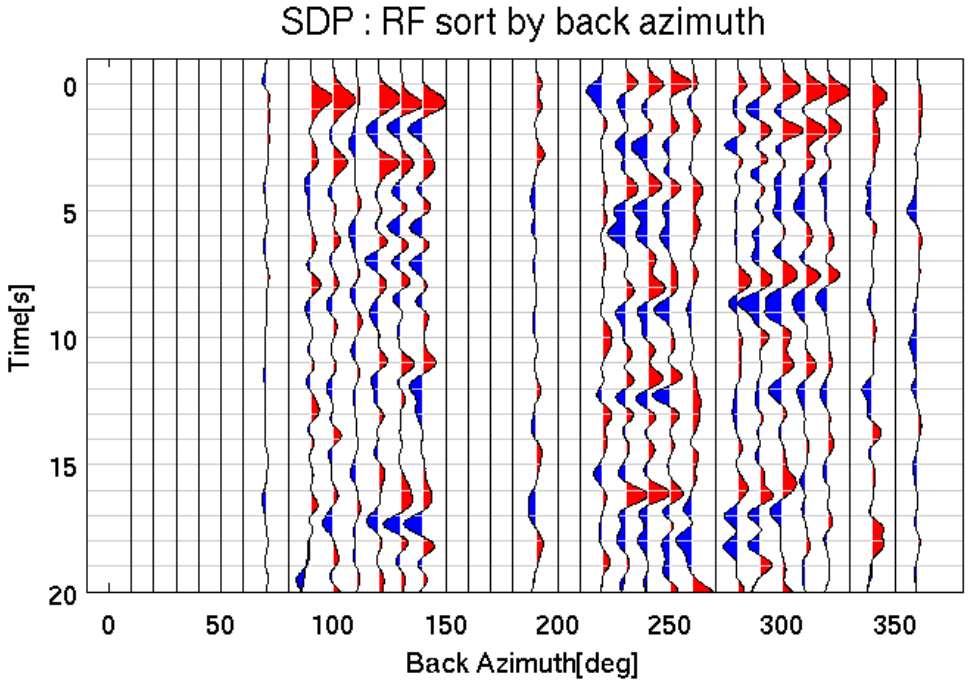
SDP : RF sort by back azimuth
Time[s]
0
5
10
15
20
0
50
100
150
200
250
300
350
Back Azimuth[deg]

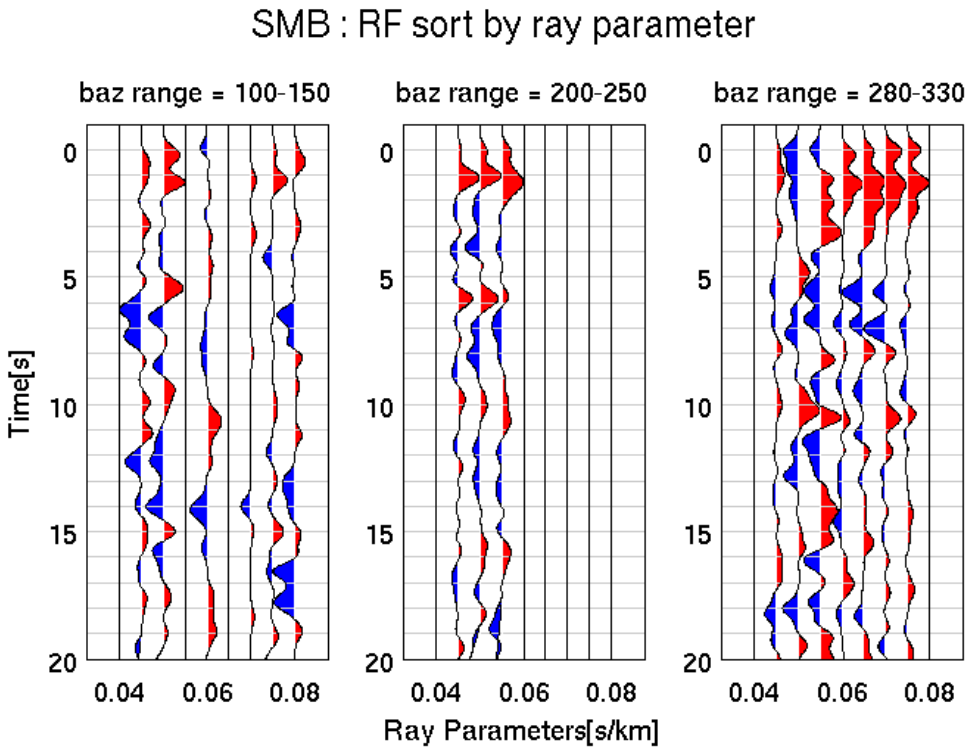
SMB : RF sort by ray parameter
baz range = 100-150
baz range = 200-250
baz range = 280-330
Time[s]
0
5
10
15
20
0.04
0.06
0.08
Ray Parameters[s/km]

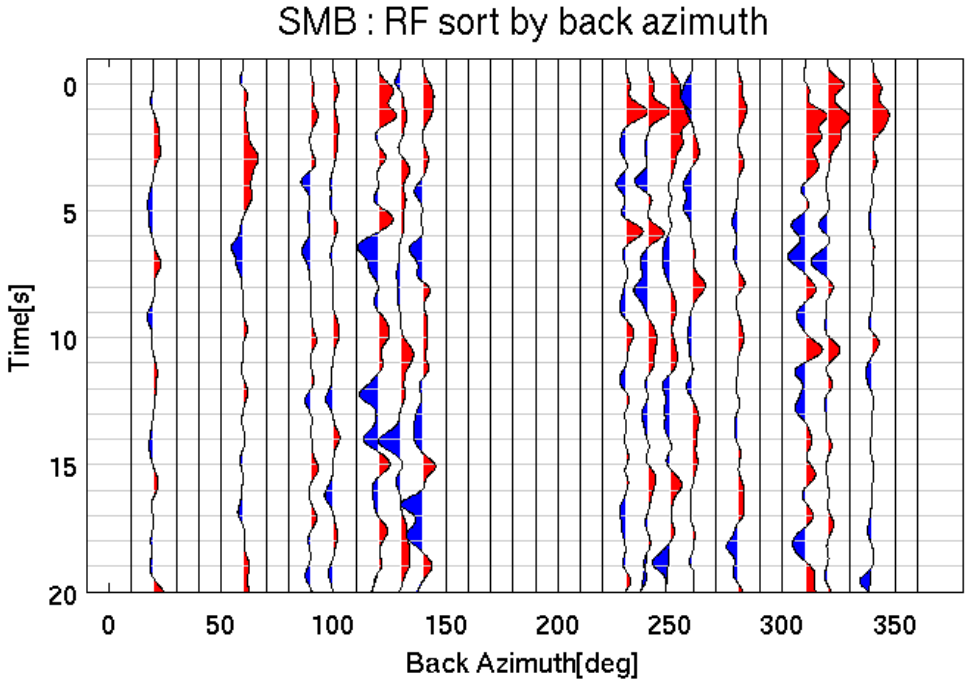
SMB : RF sort by back azimuth
Time[s]
0
5
10
15
20
0
50
100
150
200
250
300
350
Back Azimuth[deg]

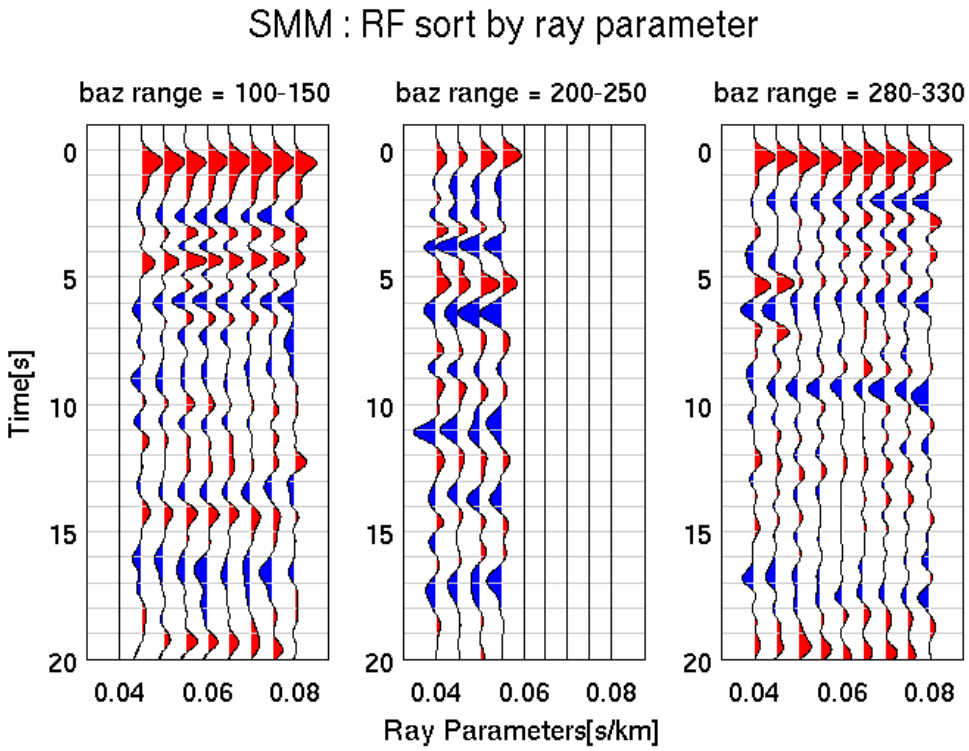
SMM : RF sort by ray parameter
baz range = 100-150
baz range = 200-250
baz range = 280-330
Time[s]
0
5
10
15
20
0.04
0.06
0.08
Ray Parameters[s/km]

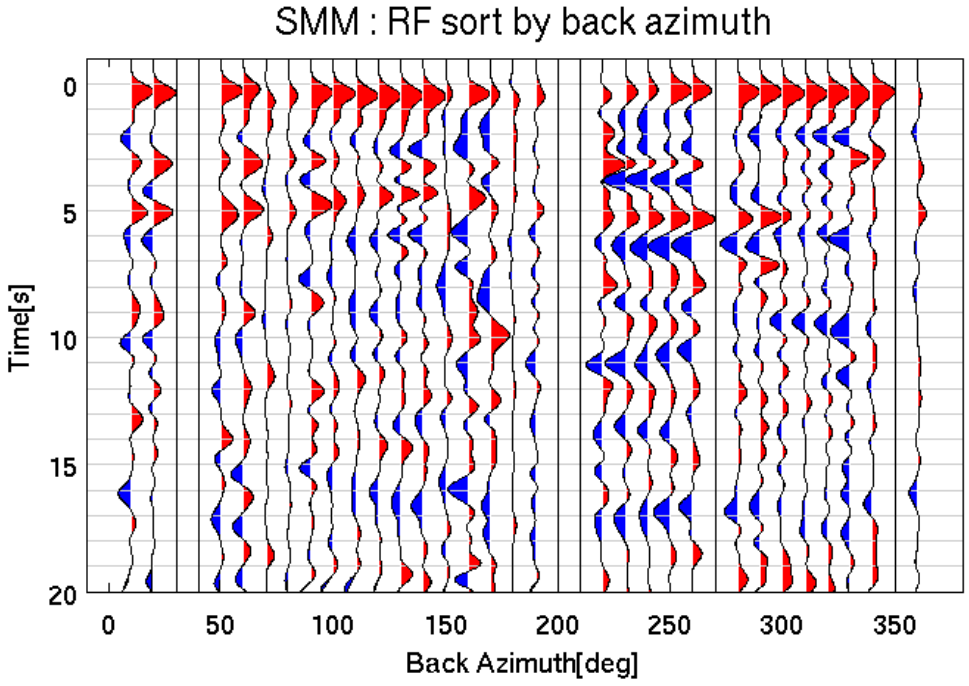
SMM : RF sort by back azimuth
Time[s]
0
5
10
15
20
0
50
100
150
200
250
300
350
Back Azimuth[deg]

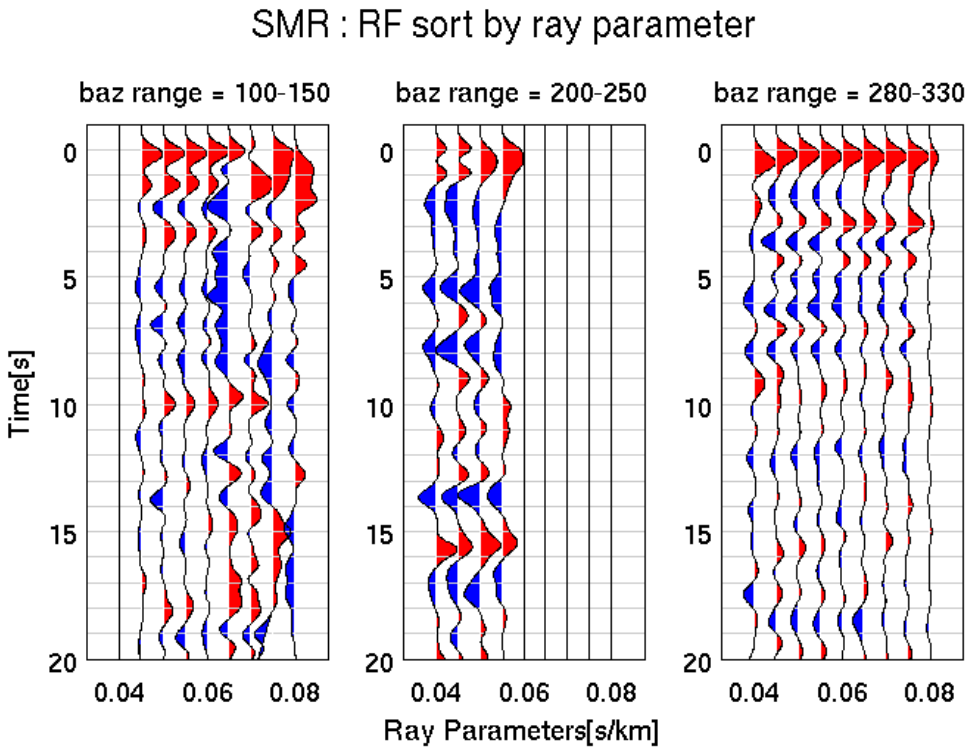
SMR : RF sort by ray parameter
baz range = 100-150
baz range = 200-250
baz range = 280-330
Time[s]
0
5
10
15
20
0.04
0.06
0.08
Ray Parameters[s/km]

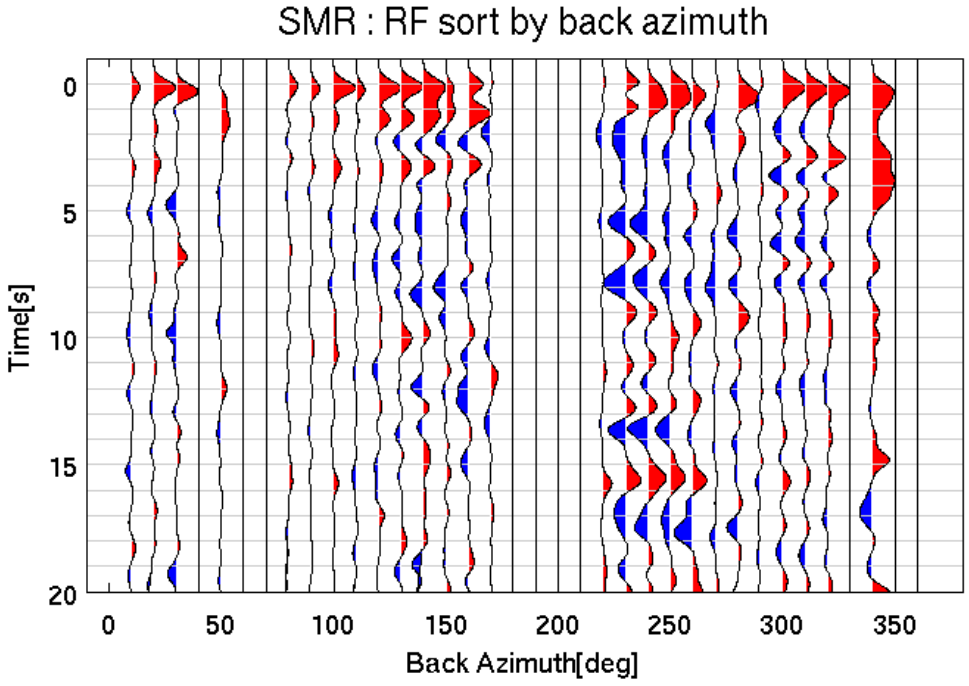
SMR : RF sort by back azimuth
Time[s]
0
5
10
15
20
0
50
100
150
200
250
300
350
Back Azimuth[deg]

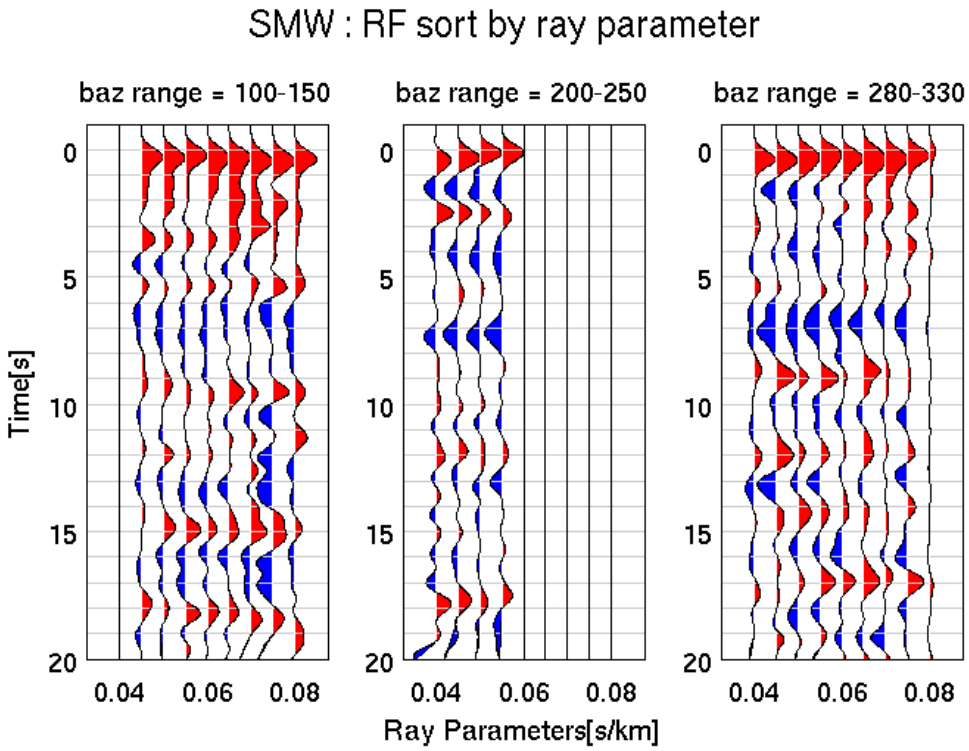
SMW : RF sort by ray parameter
baz range = 100-150
baz range = 200-250
baz range = 280-330
Time[s]
0
5
10
15
20
0.04
0.06
0.08
Ray Parameters[s/km]

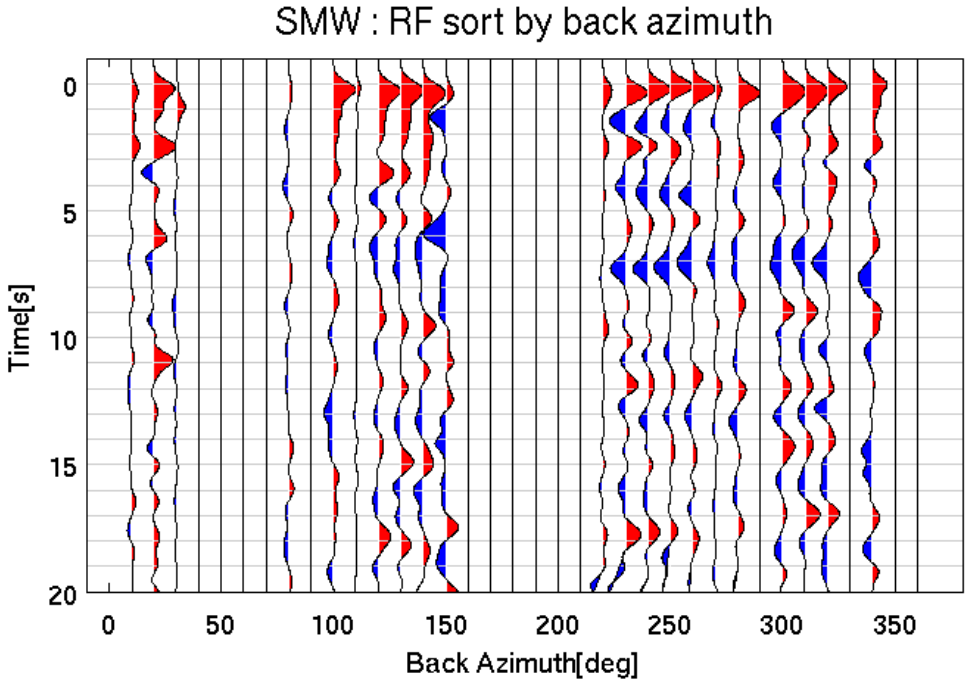
SMW : RF sort by back azimuth
Time[s]
0
5
10
15
20
0
50
100
150
200
250
300
350
Back Azimuth[deg]

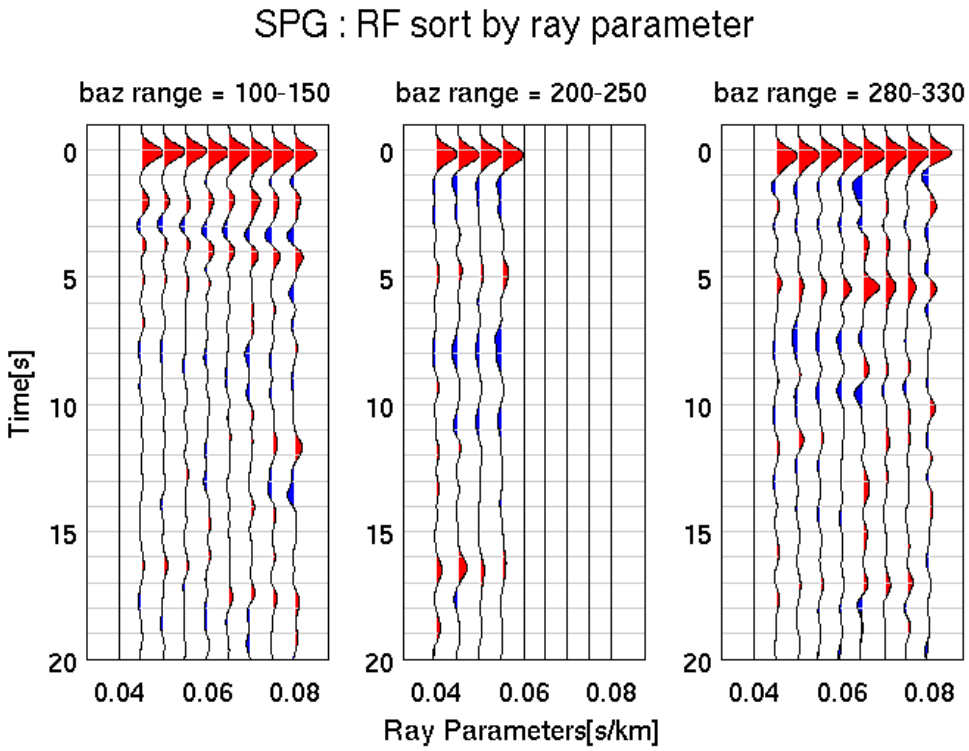
SPG : RF sort by ray parameter
baz range = 100-150
baz range = 200-250
baz range = 280-330
Time[s]
0
5
10
15
20
0.04
0.06
0.08
Ray Parameters[s/km]

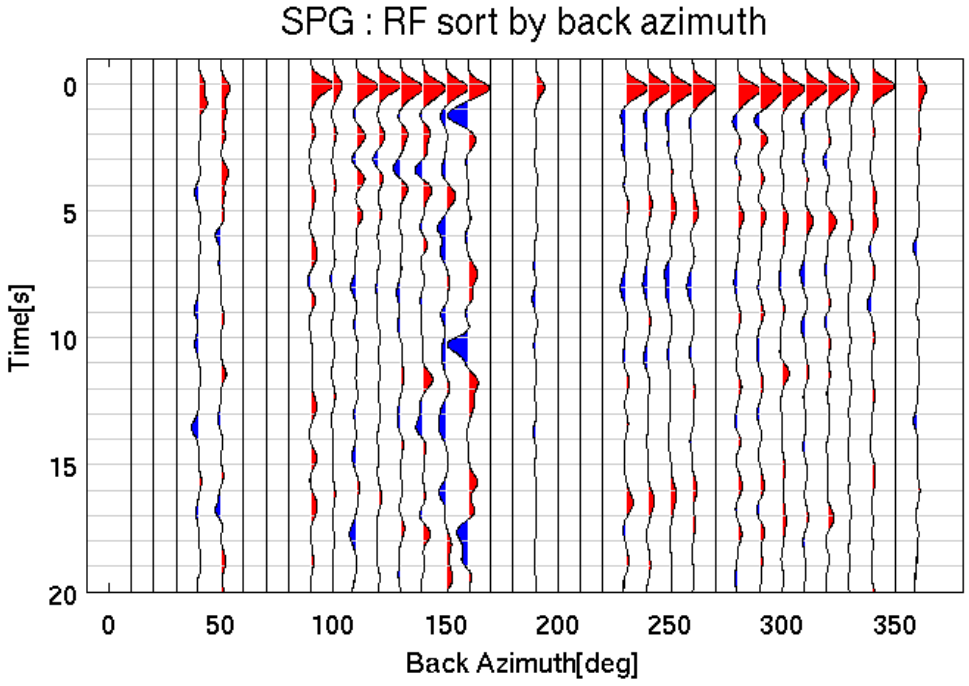
SPG : RF sort by back azimuth
Time[s]
0
5
10
15
20
0
50
100
150
200
250
300
350
Back Azimuth[deg]

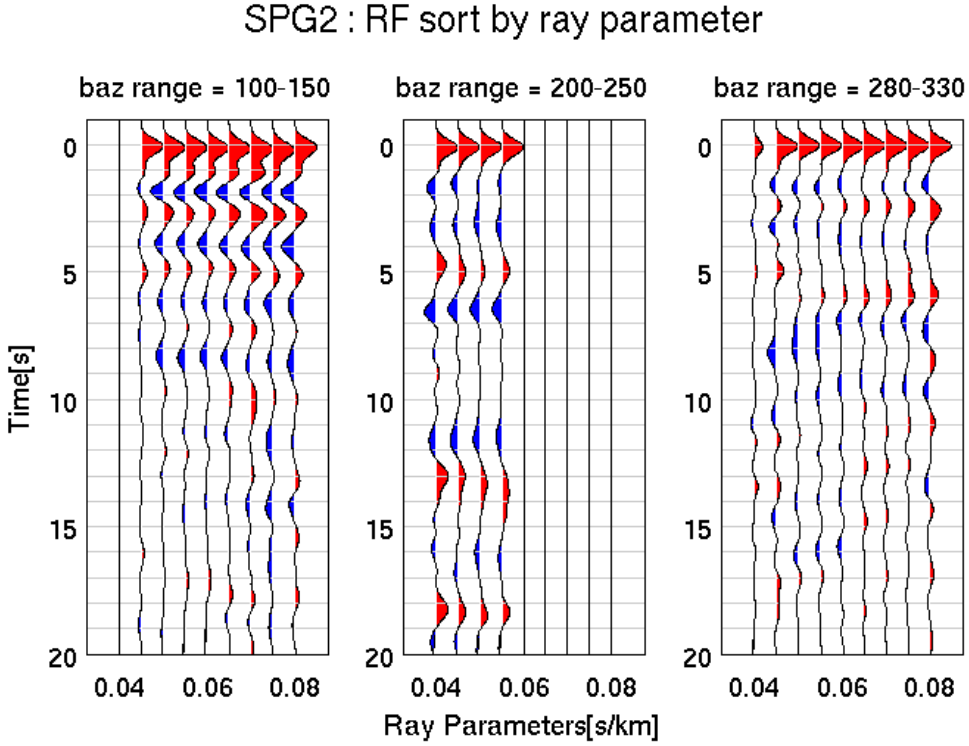
SPG2 : RF sort by ray parameter
baz range = 100-150
baz range = 200-250
baz range = 280-330
Time[s]
0
5
10
15
20
0.04
0.06
0.08
Ray Parameters[s/km]

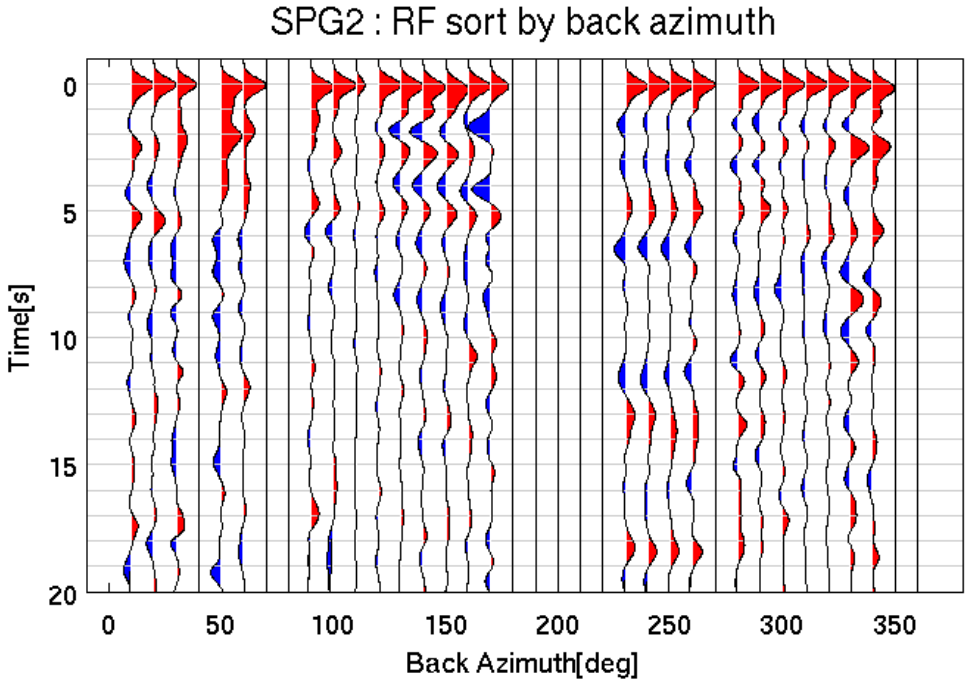
SPG2 : RF sort by back azimuth
Time[s]
0
5
10
15
20
0
50
100
150
200
250
300
350
Back Azimuth[deg]

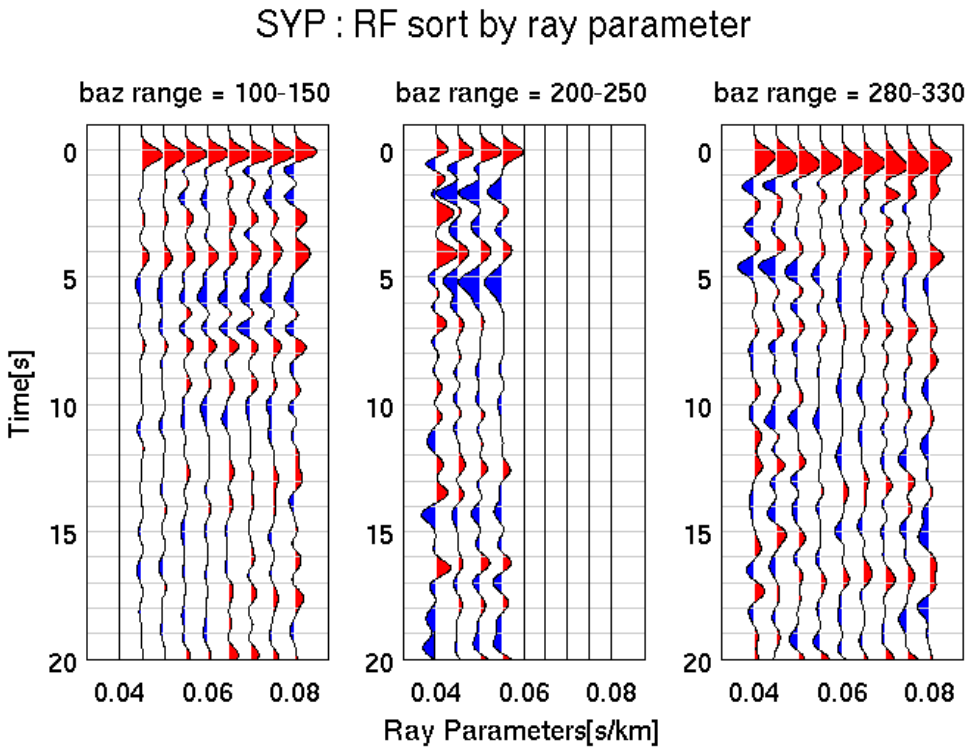
SYP : RF sort by ray parameter
baz range = 100-150
baz range = 200-250
baz range = 280-330
Time[s]
0
5
10
15
20
0.04
0.06
0.08
Ray Parameters[s/km]

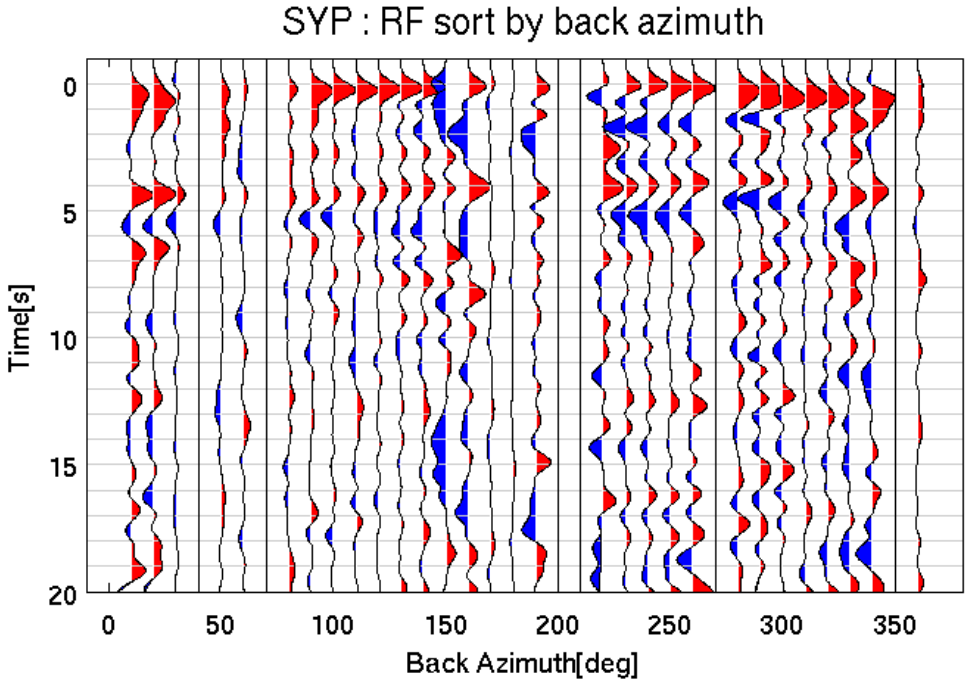
SYP : RF sort by back azimuth
Time[s]
0
5
10
15
20
0
50
100
150
200
250
300
350
Back Azimuth[deg]

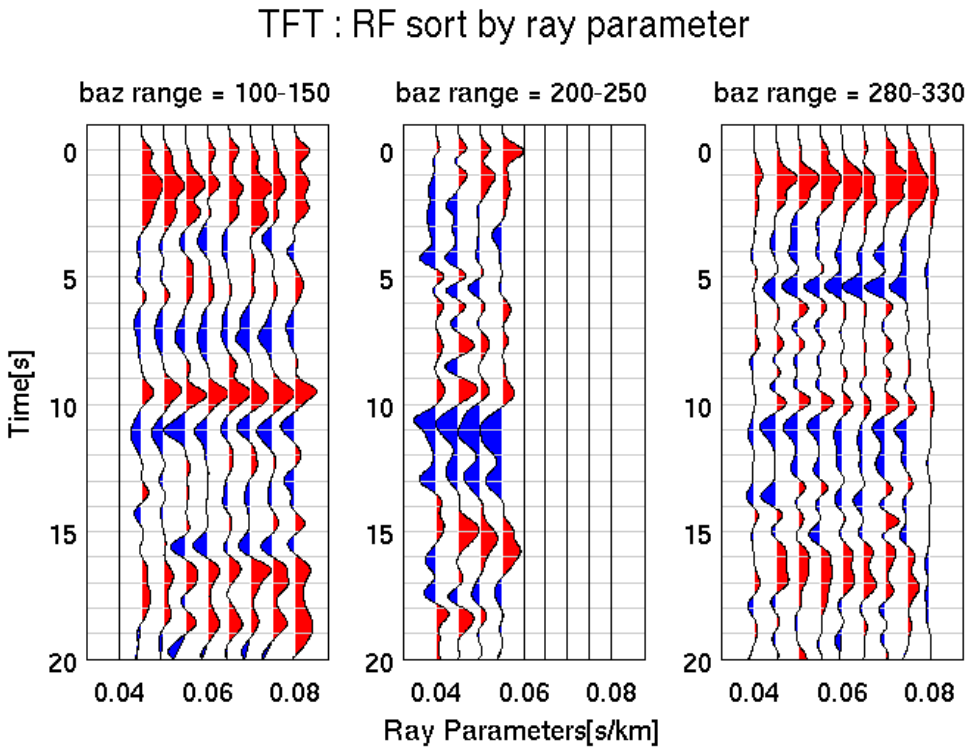
TFT : RF sort by ray parameter
baz range = 100-150
baz range = 200-250
baz range = 280-330
Time[s]
0
5
10
15
20
0.04
0.06
0.08
Ray Parameters[s/km]

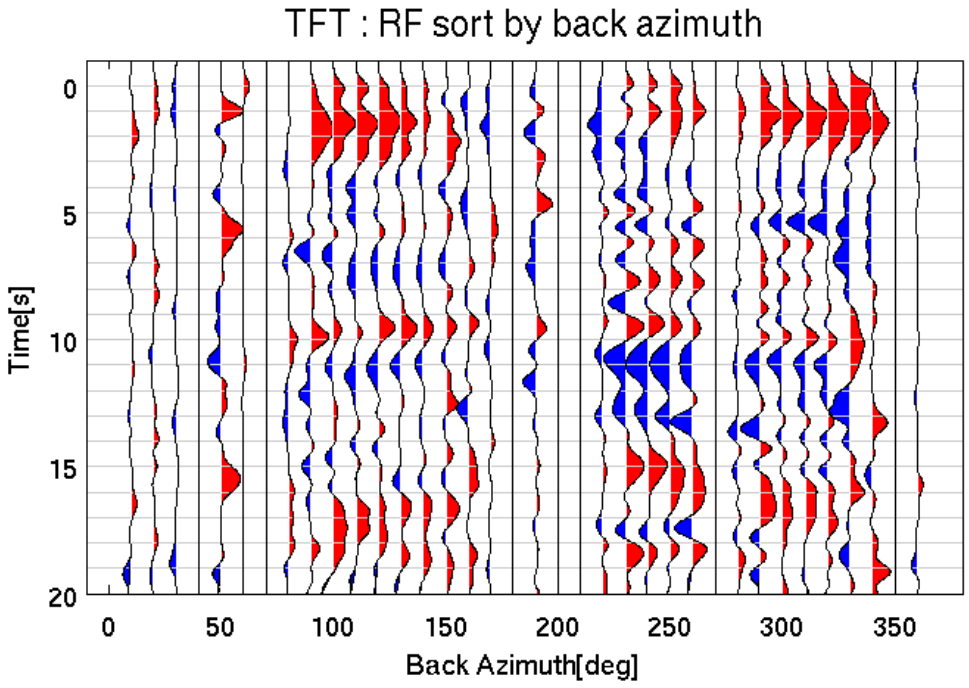
TFT : RF sort by back azimuth
Time[s]
0
5
10
15
20
0
50
100
150
200
250
300
350
Back Azimuth[deg]

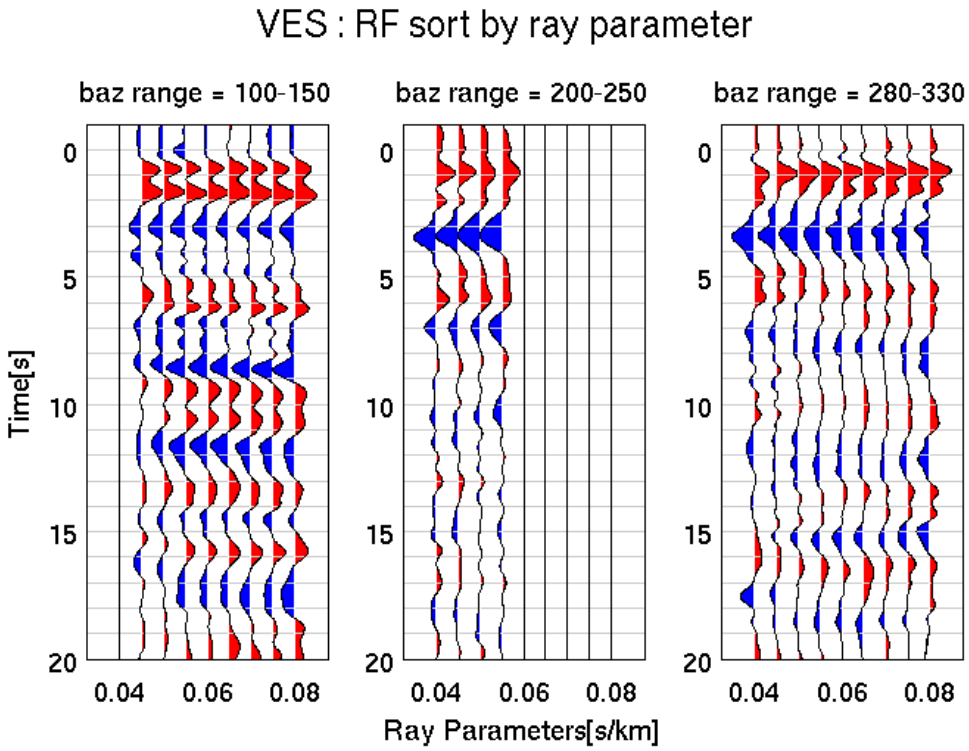
VES : RF sort by ray parameter
baz range = 100-150
baz range = 200-250
baz range = 280-330
Time[s]
0
5
10
15
20
0.04
0.06
0.08
Ray Parameters[s/km]

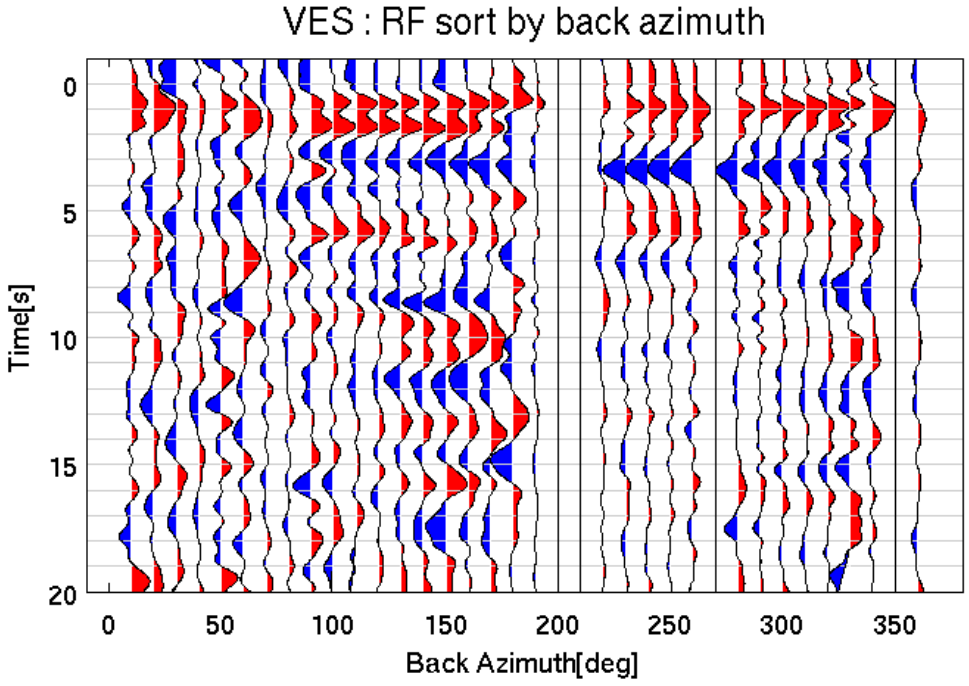
VES : RF sort by back azimuth
Time[s]
0
5
10
15
20
0
50
100
150
200
250
300
350
Back Azimuth[deg]

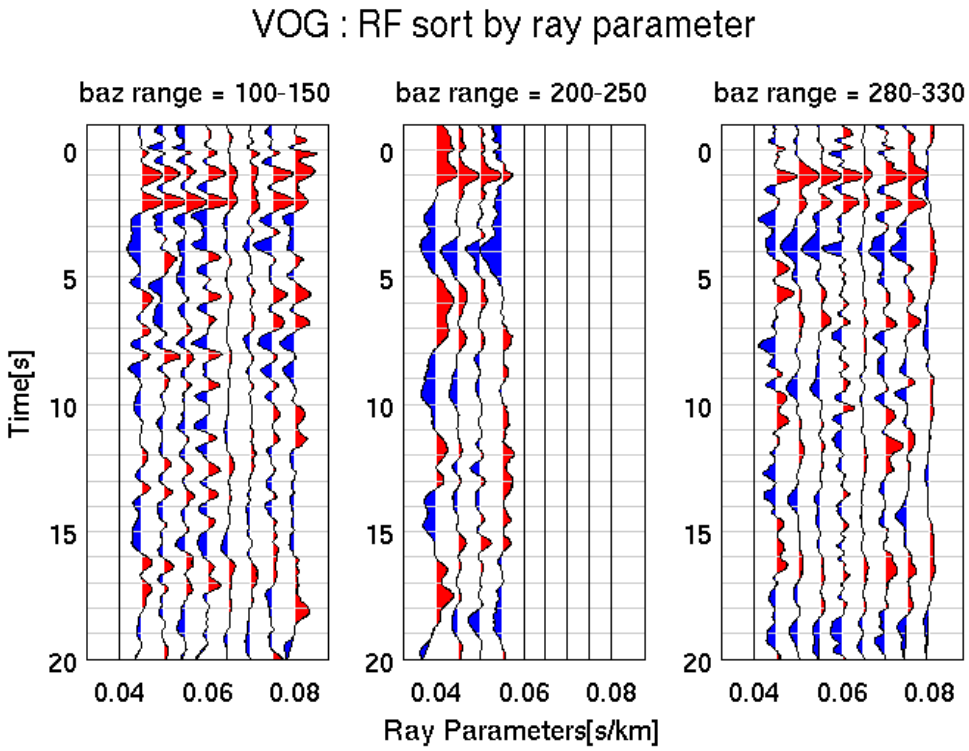
VOG : RF sort by ray parameter
baz range = 100-150
baz range = 200-250
baz range = 280-330
Time[s]
0
5
10
15
20
0.04
0.06
0.08
Ray Parameters[s/km]

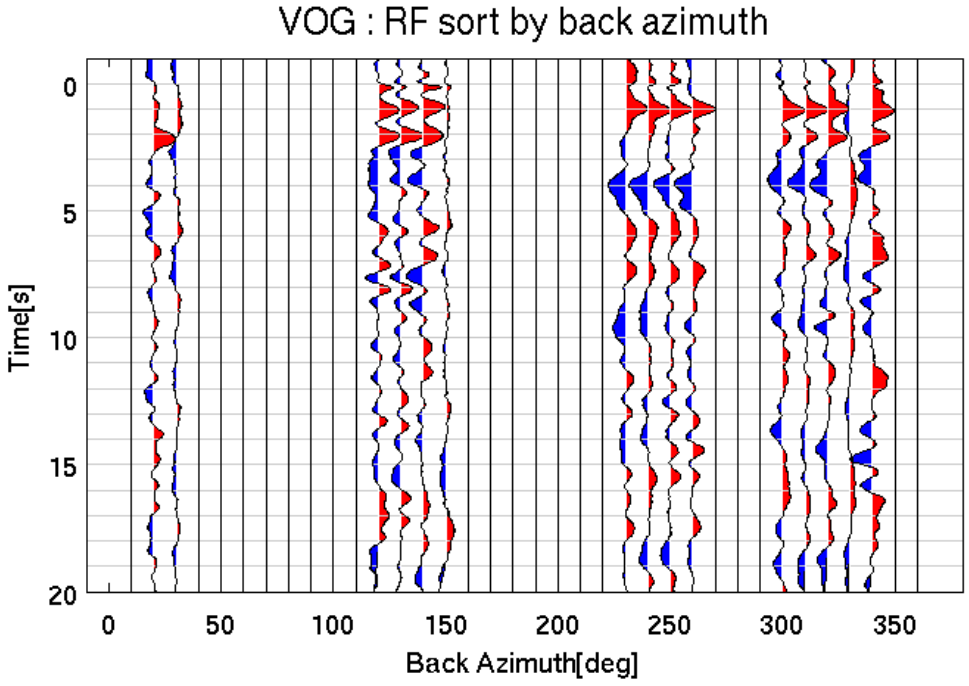
VOG : RF sort by back azimuth
Time[s]
0
5
10
15
20
0
50
100
150
200
250
300
350
Back Azimuth[deg]

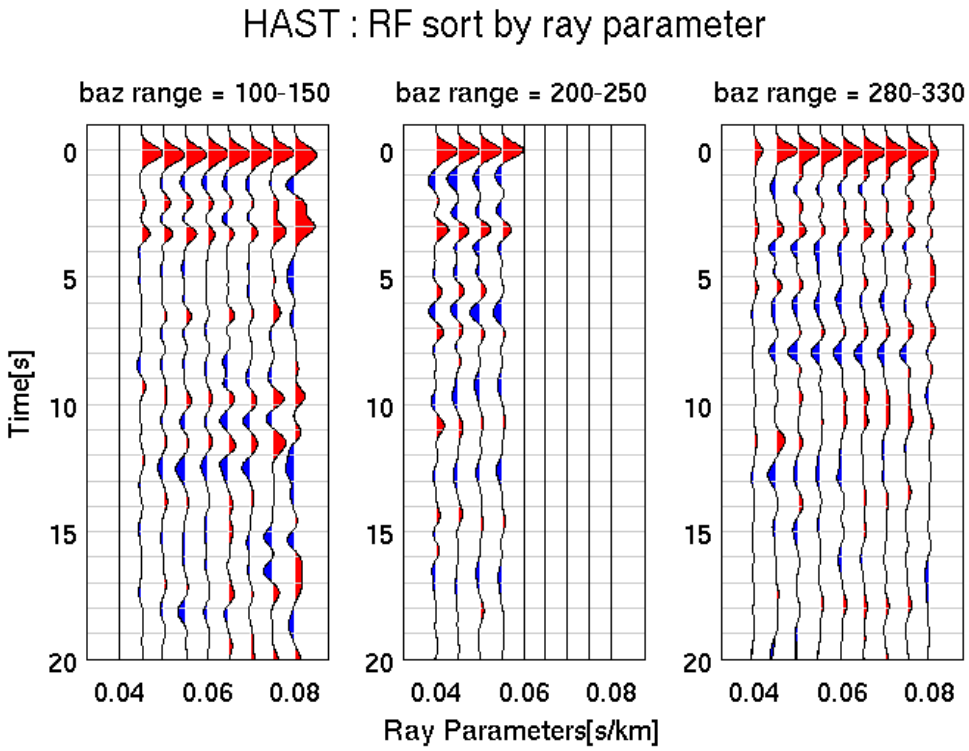
HAST : RF sort by ray parameter
baz range = 100-150
baz range = 200-250
baz range = 280-330
Time[s]
0
5
10
15
20
0.04
0.06
0.08
Ray Parameters[s/km]

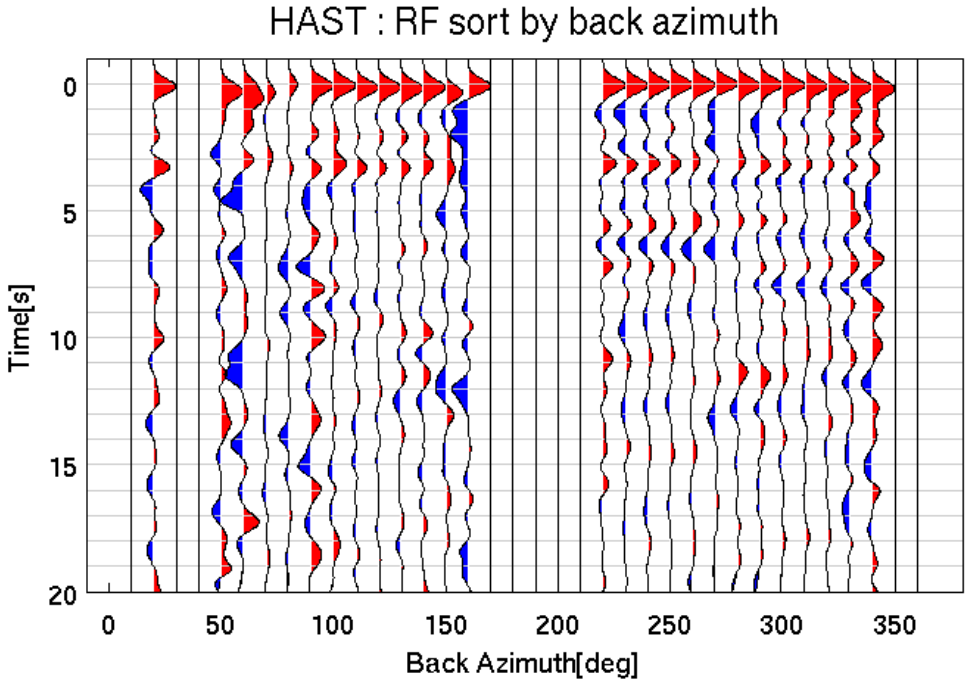
HAST : RF sort by back azimuth
Time[s]
0
5
10
15
20
0
50
100
150
200
250
300
350
Back Azimuth[deg]

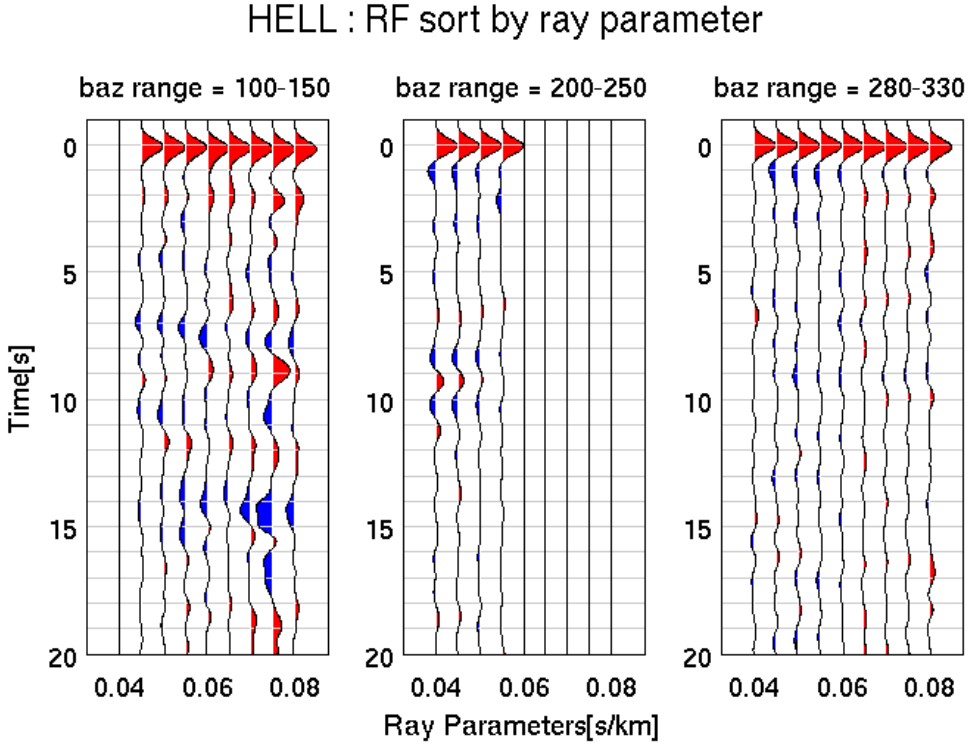
HELL : RF sort by ray parameter
baz range = 100-150
baz range = 200-250
baz range = 280-330
Time[s]
0
5
10
15
20
0.04
0.06
0.08
Ray Parameters[s/km]

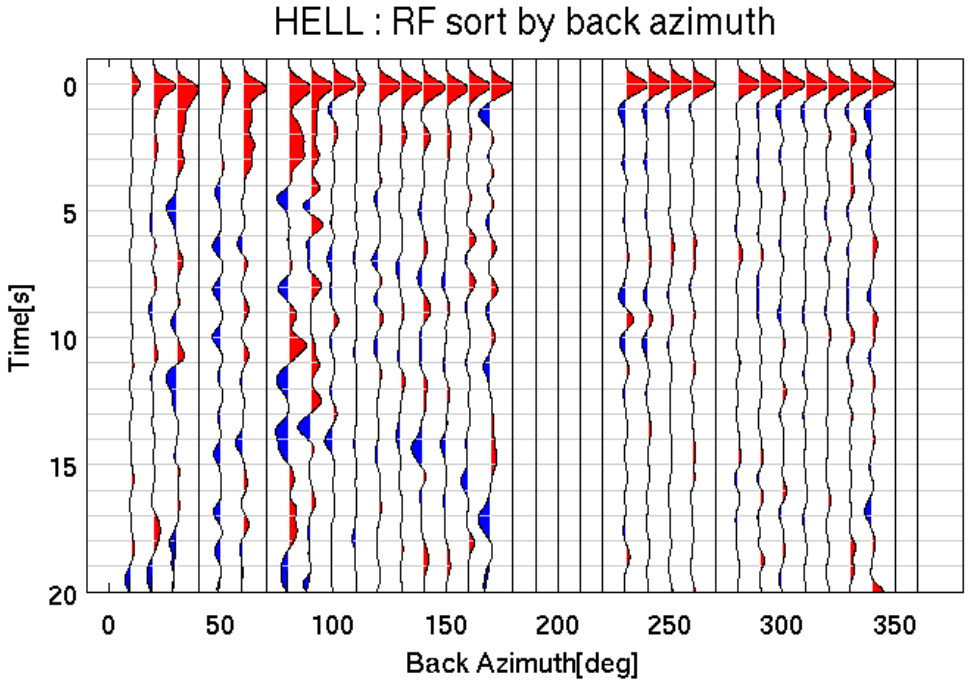
HELL : RF sort by back azimuth
Time[s]
0
5
10
15
20
0
50
100
150
200
250
300
350
Back Azimuth[deg]

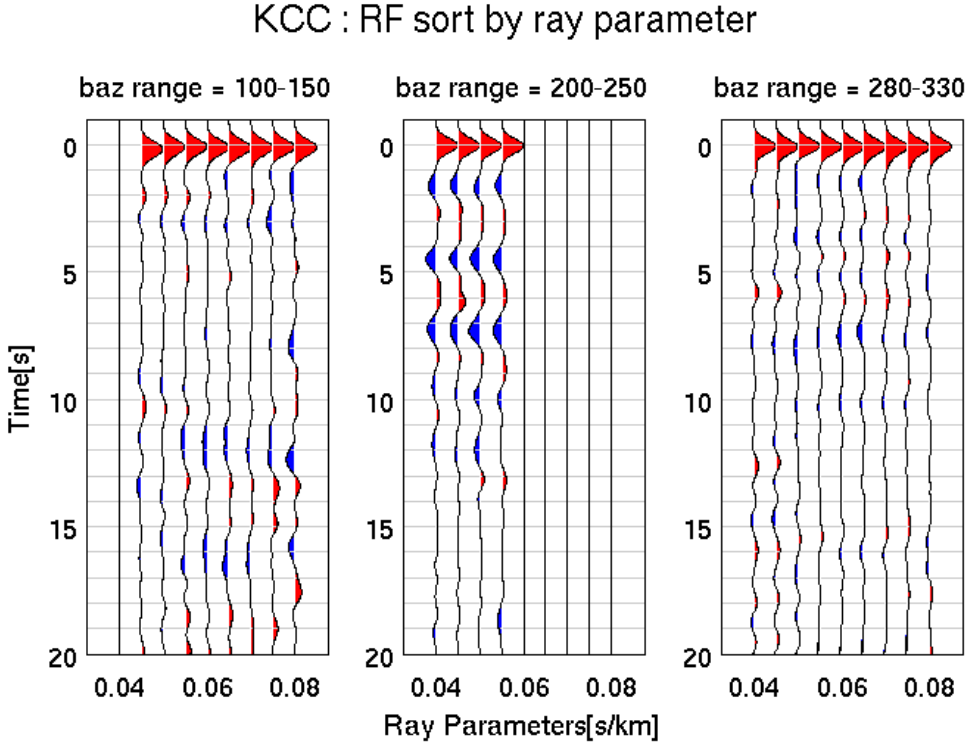
KCC : RF sort by ray parameter
baz range = 100-150
baz range = 200-250
baz range = 280-330
Time[s]
0
5
10
15
20
0.04
0.06
0.08
Ray Parameters[s/km]

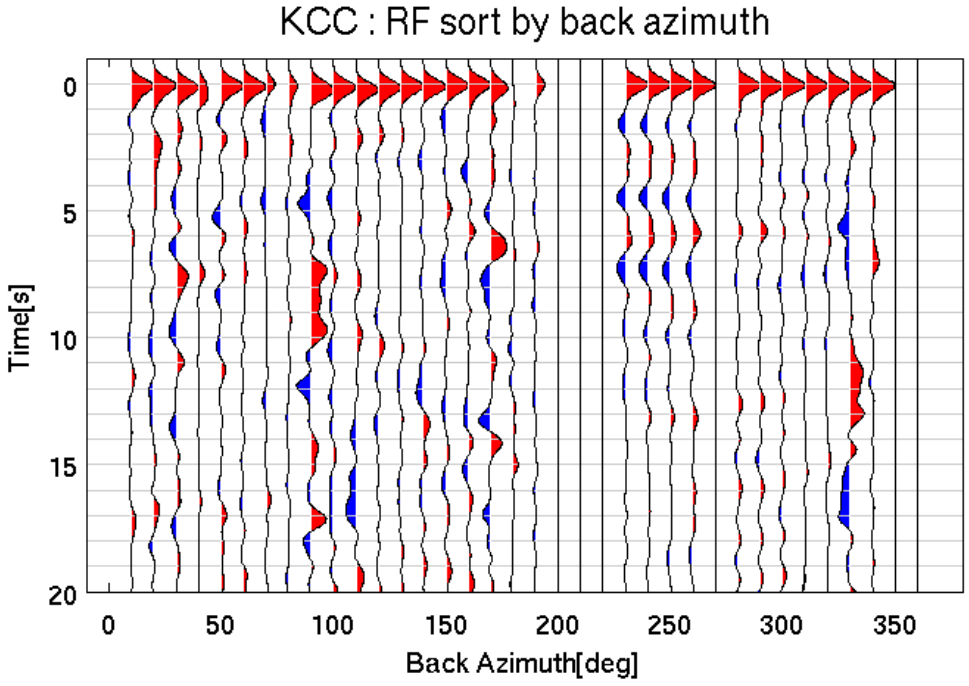
KCC : RF sort by back azimuth
Time[s]
0
5
10
15
20
0
50
100
150
200
250
300
350
Back Azimuth[deg]

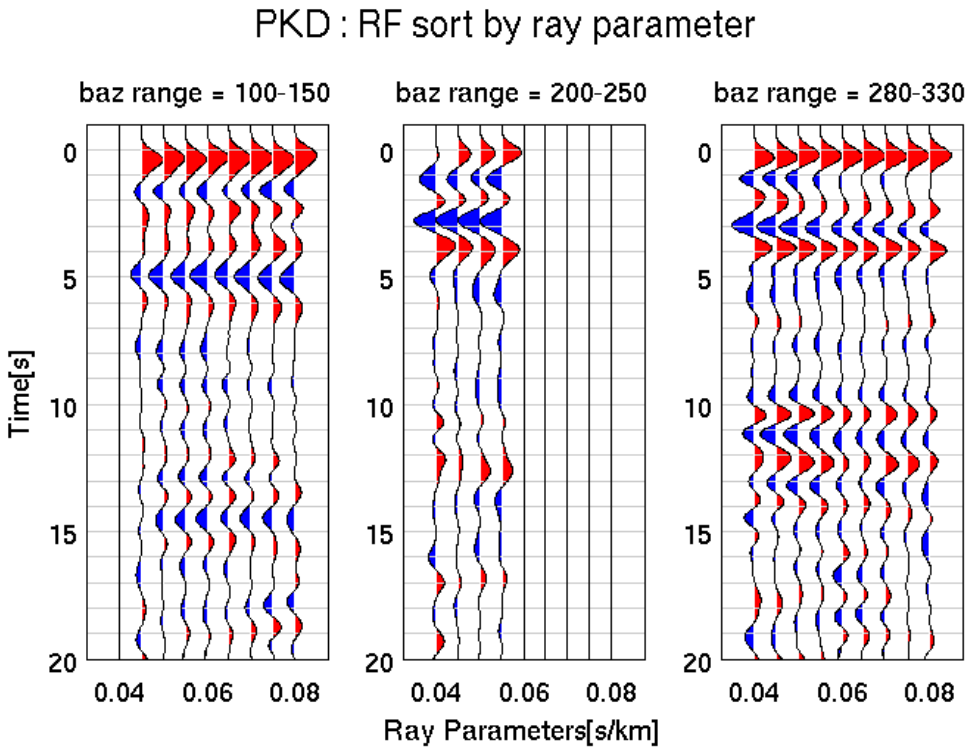
PKD : RF sort by ray parameter
baz range = 100-150
baz range = 200-250
baz range = 280-330
Time[s]
0
5
10
15
20
0.04
0.06
0.08
Ray Parameters[s/km]

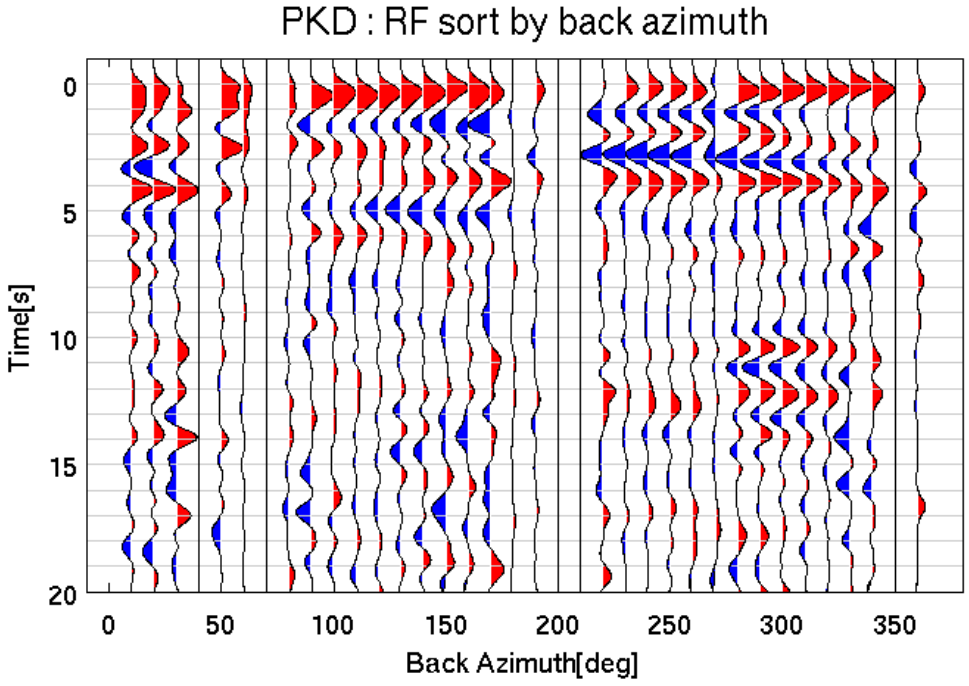
PKD : RF sort by back azimuth
Time[s]
0
5
10
15
20
0
50
100
150
200
250
300
350
Back Azimuth[deg]

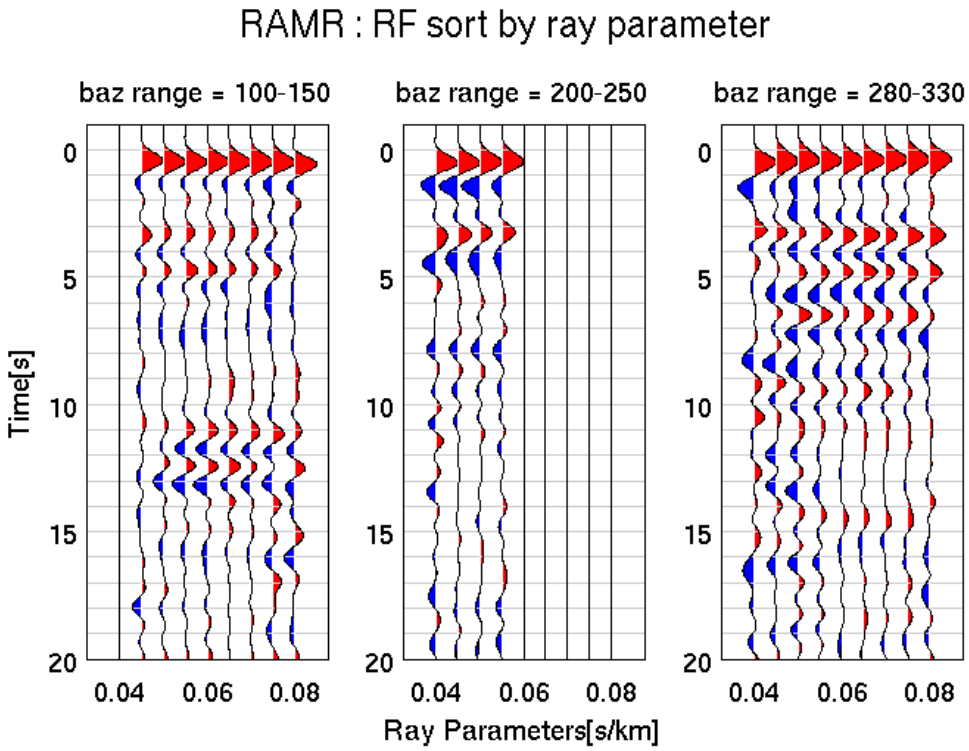
RAMR : RF sort by ray parameter
baz range = 100-150
baz range = 200-250
baz range = 280-330
Time[s]
0
5
10
15
20
0.04
0.06
0.08
Ray Parameters[s/km]

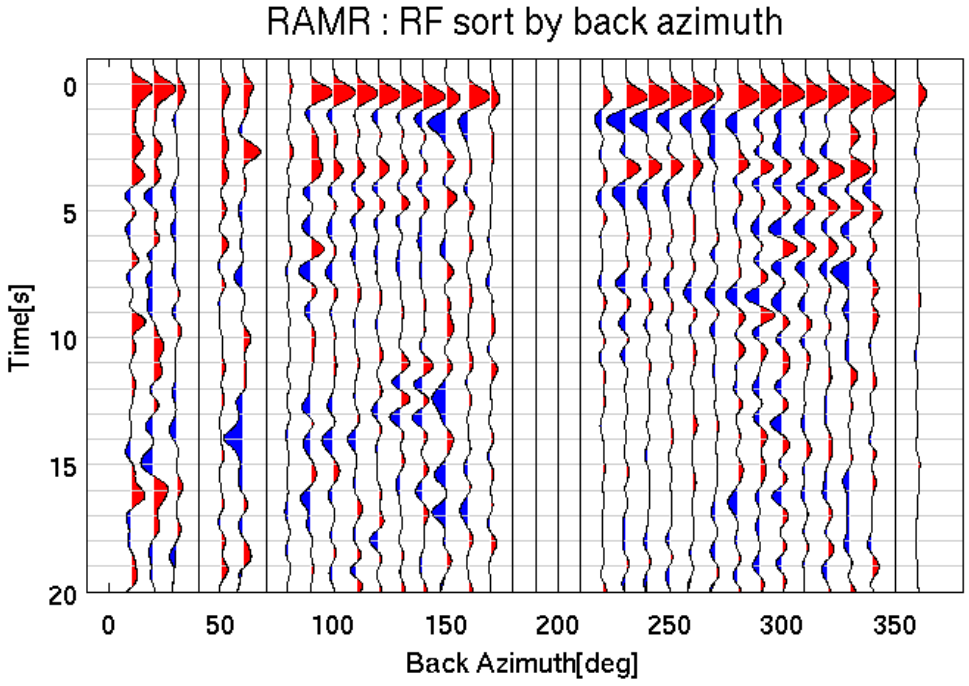
RAMR : RF sort by back azimuth
Time[s]
0
5
10
15
20
0
50
100
150
200
250
300
350
Back Azimuth[deg]

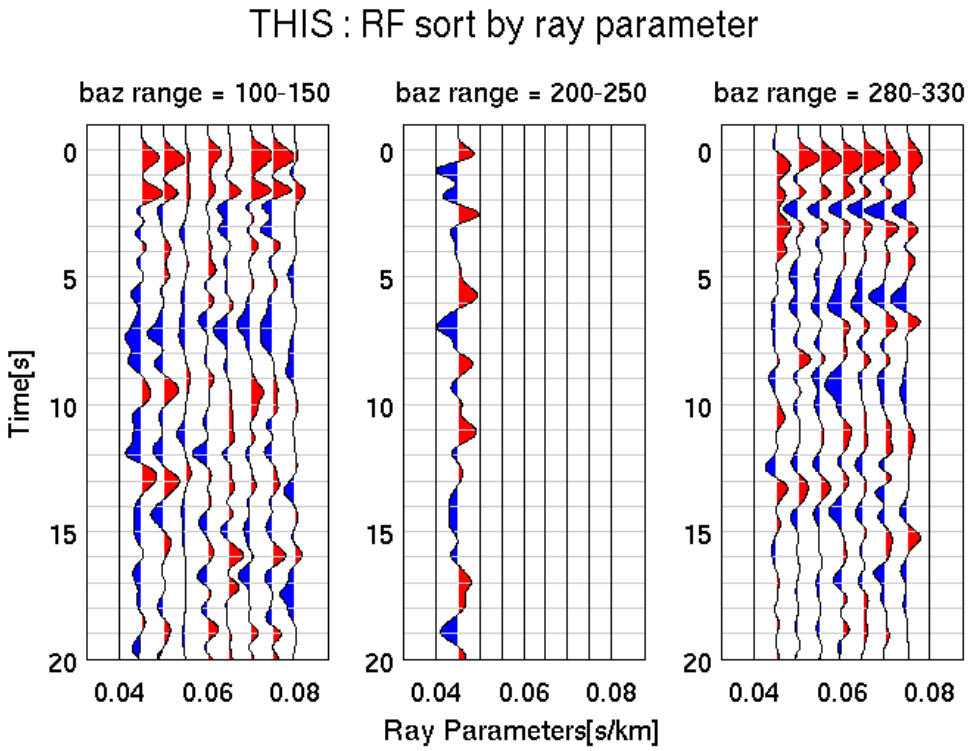
THIS : RF sort by ray parameter
baz range = 100-150
baz range = 200-250
baz range = 280-330
Time[s]
0
5
10
15
20
0.04
0.06
0.08
Ray Parameters[s/km]

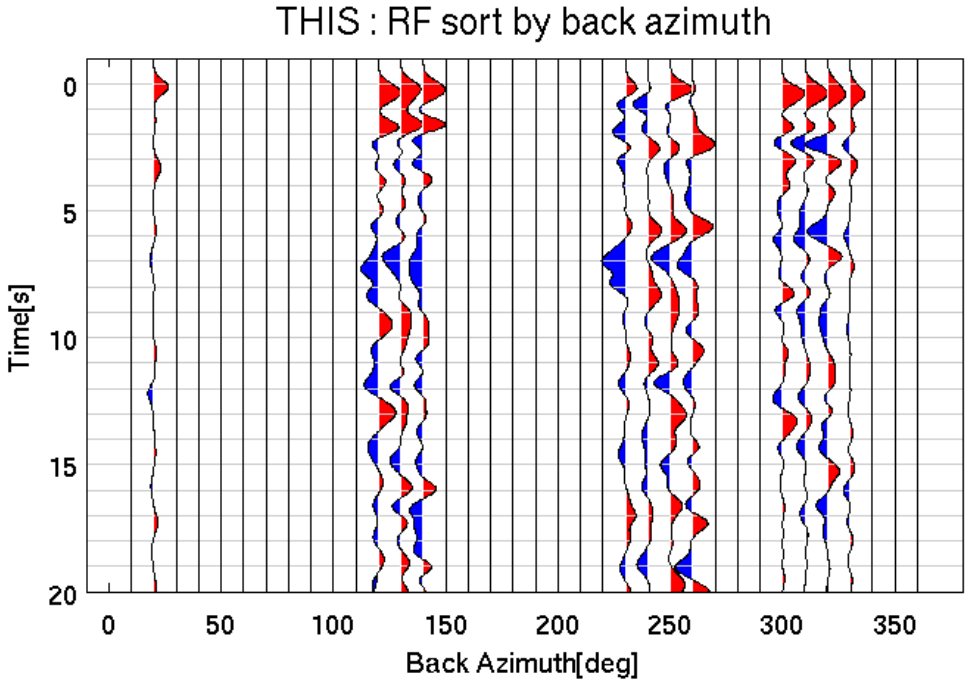
THIS : RF sort by back azimuth
Time[s]
0
5
10
15
20
0
50
100
150
200
250
300
350
Back Azimuth[deg]

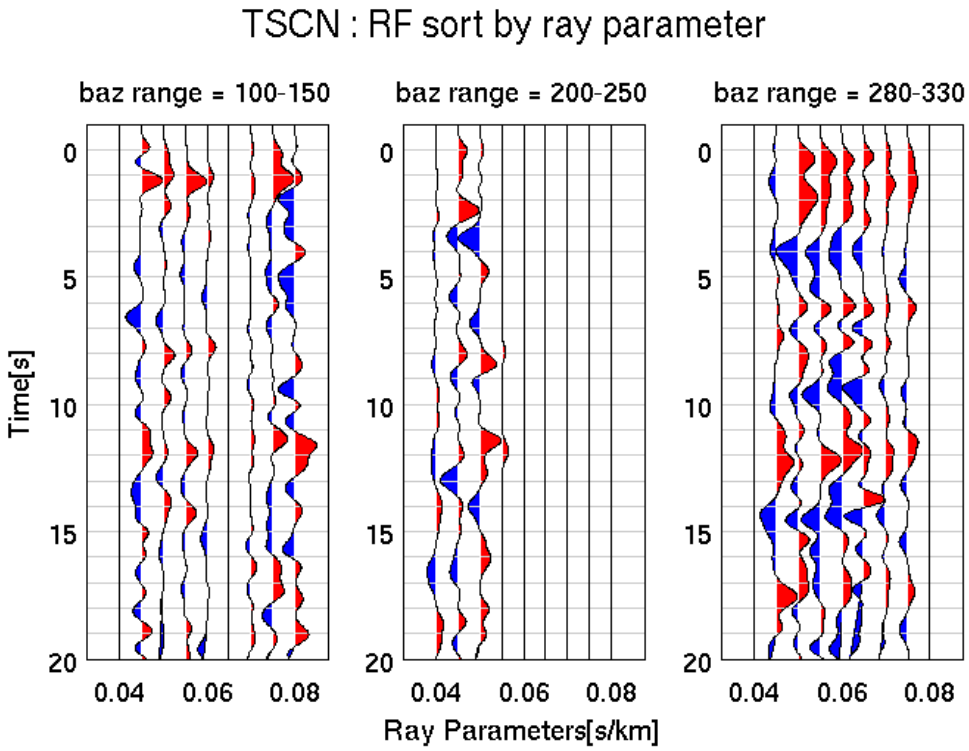
TSCN : RF sort by ray parameter
baz range = 100-150
baz range = 200-250
baz range = 280-330
Time[s]
0
5
10
15
20
0.04
0.06
0.08
Ray Parameters[s/km]

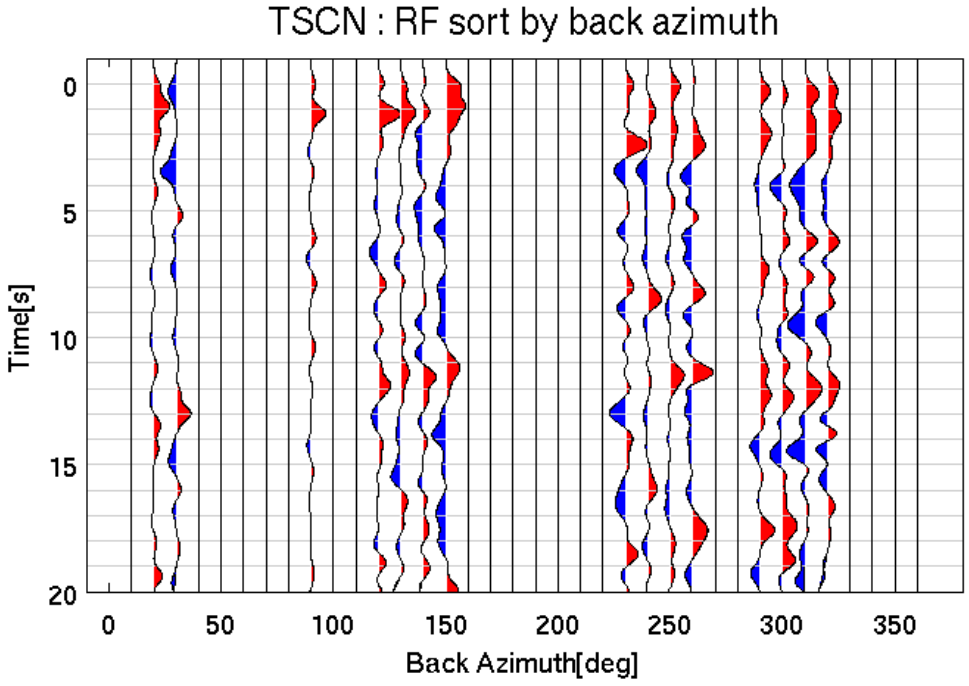
TSCN : RF sort by back azimuth
Time[s]
0
5
10
15
20
0
50
100
150
200
250
300
350
Back Azimuth[deg]

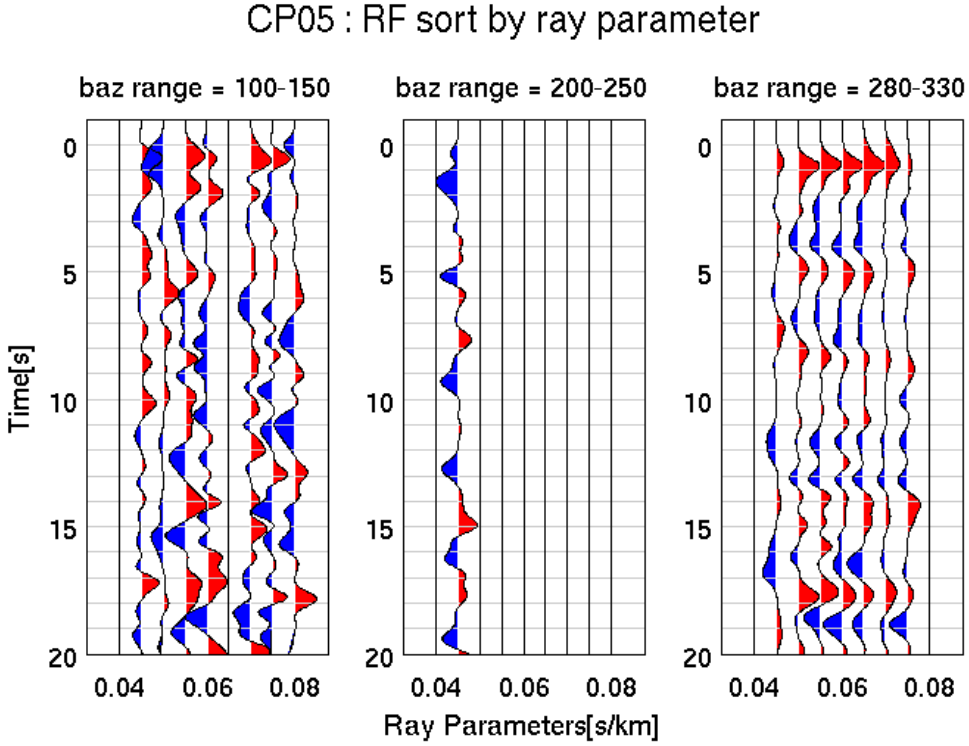
CP05 : RF sort by ray parameter
baz range = 100-150
baz range = 200-250
baz range = 280-330
Time[s]
0
5
10
15
20
0.04
0.06
0.08
Ray Parameters[s/km]

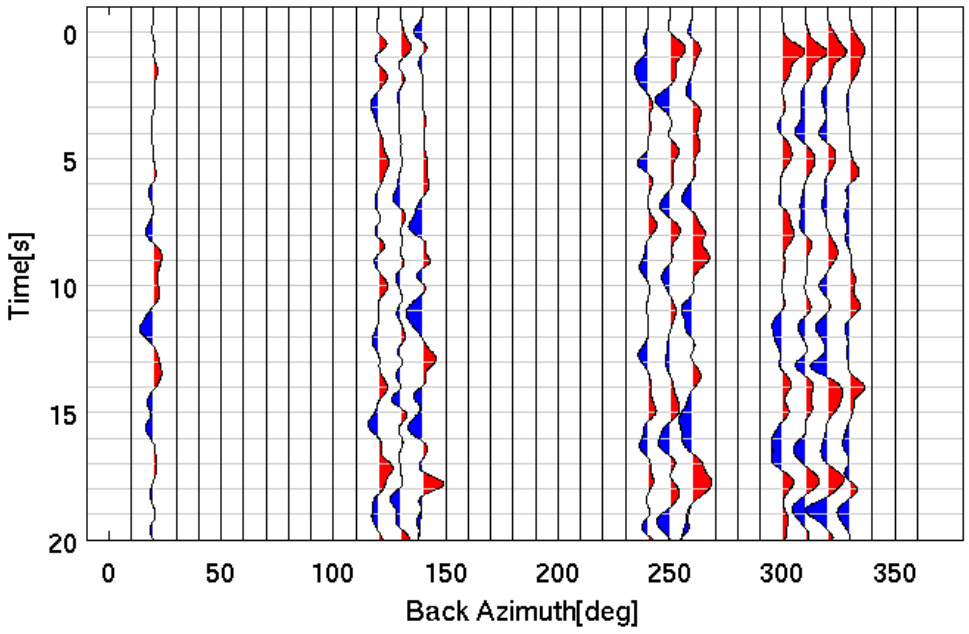
CP05 : RF sort by back azimuth
Time[s]
0
5
10
15
20
0
50
100
150
200
250
300
350
Back Azimuth[deg]

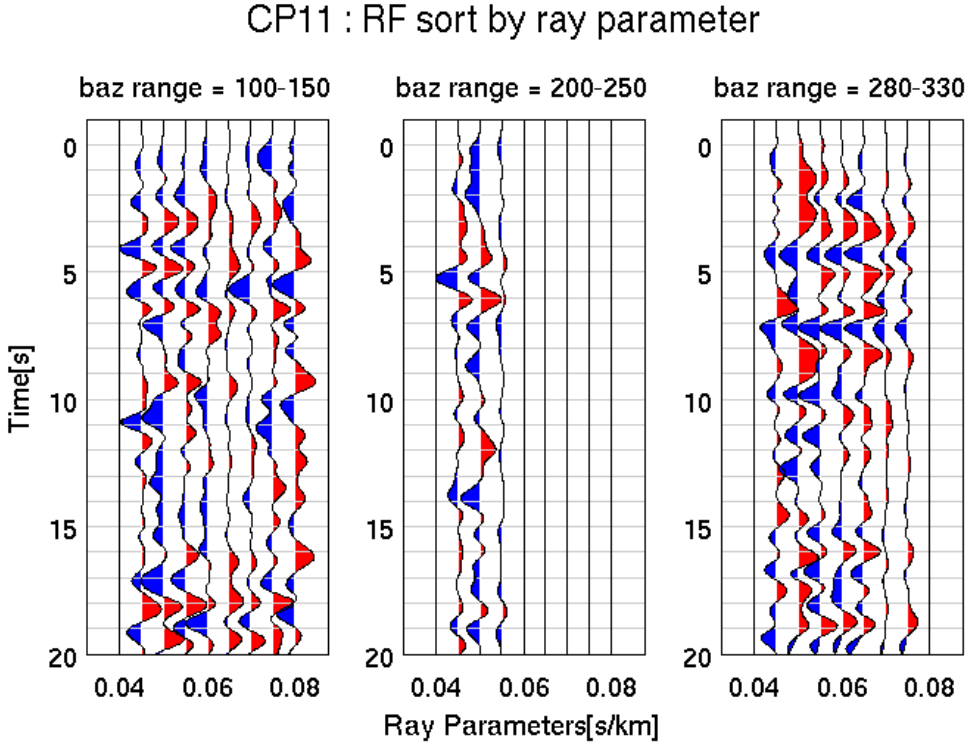
CP11 : RF sort by ray parameter
baz range = 100-150
baz range = 200-250
baz range = 280-330
Time[s]
0
5
10
15
20
0.04
0.06
0.08
Ray Parameters[s/km]

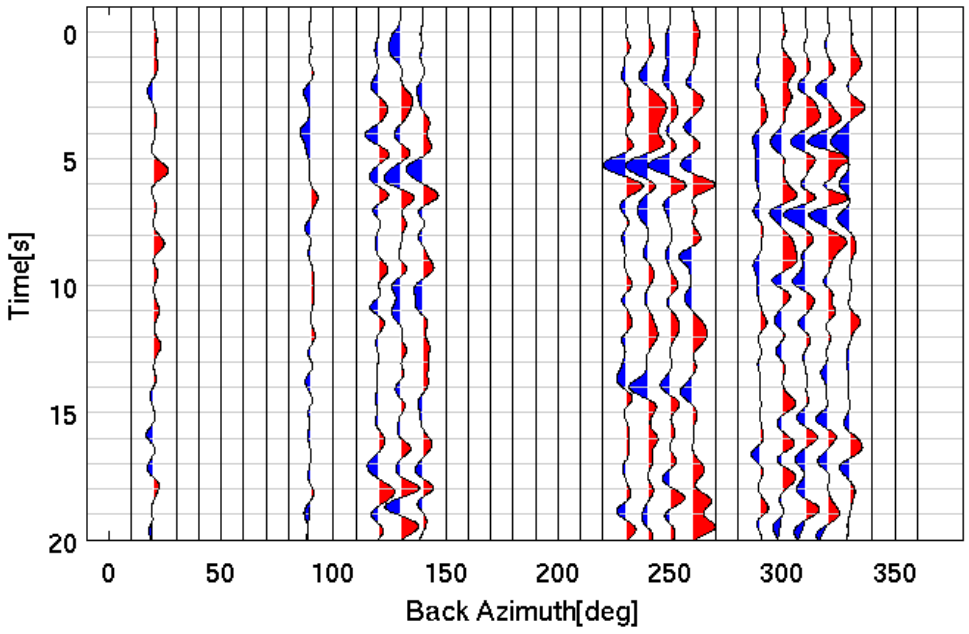
CP11 : RF sort by back azimuth
Time[s]
0
5
10
15
20
0
50
100
150
200
250
300
350
Back Azimuth[deg]

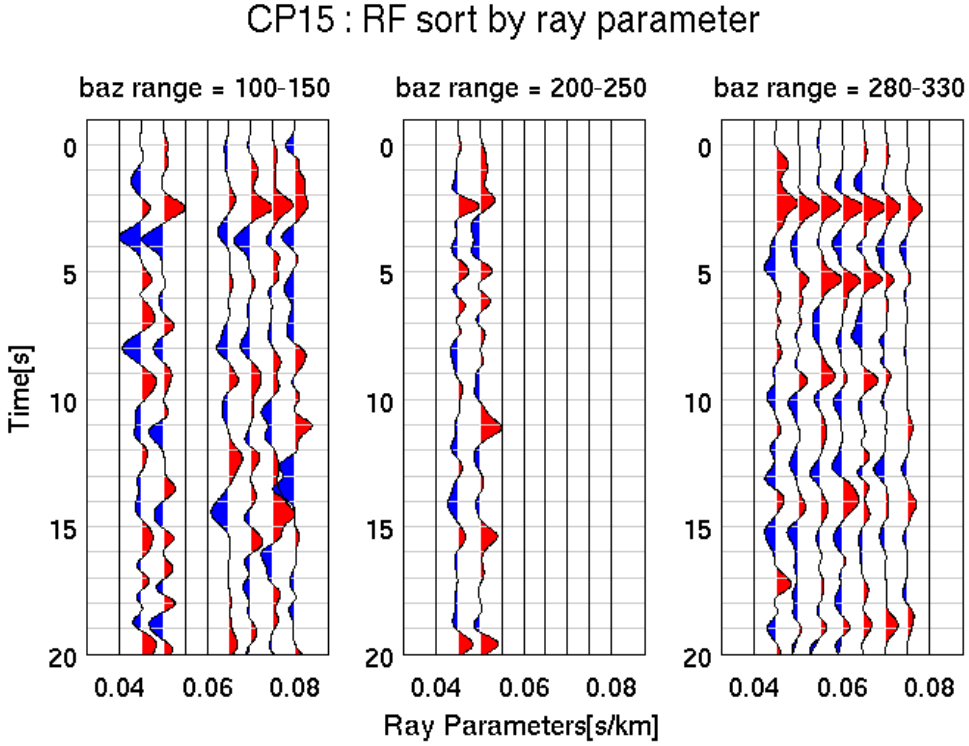
CP15 : RF sort by ray parameter
baz range = 100-150
baz range = 200-250
baz range = 280-330
Time[s]
0
5
10
15
20
0.04
0.06
0.08
Ray Parameters[s/km]

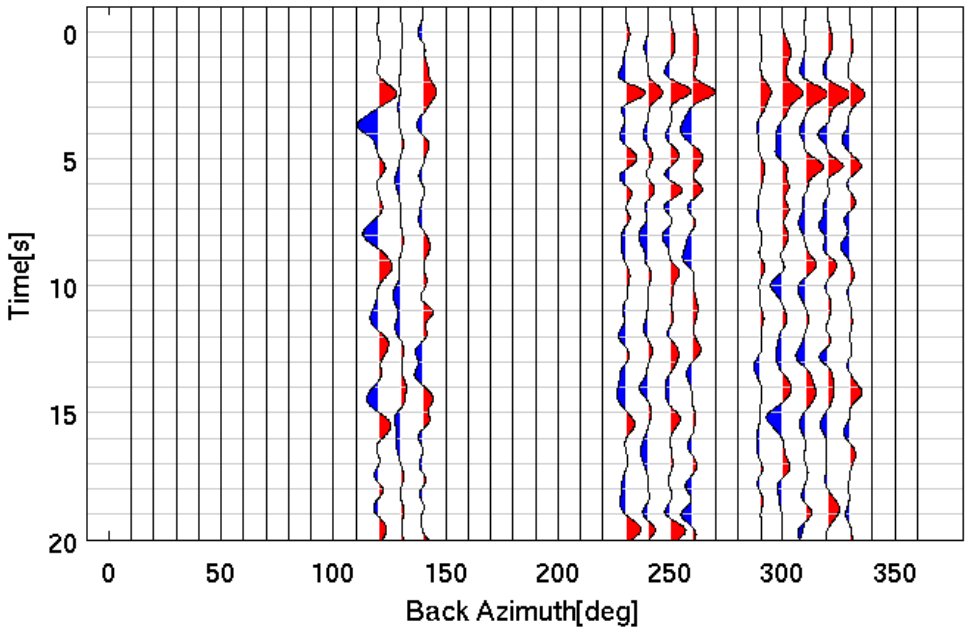
CP15 : RF sort by back azimuth
Time[s]
0
5
10
15
20
0
50
100
150
200
250
300
350
Back Azimuth[deg]

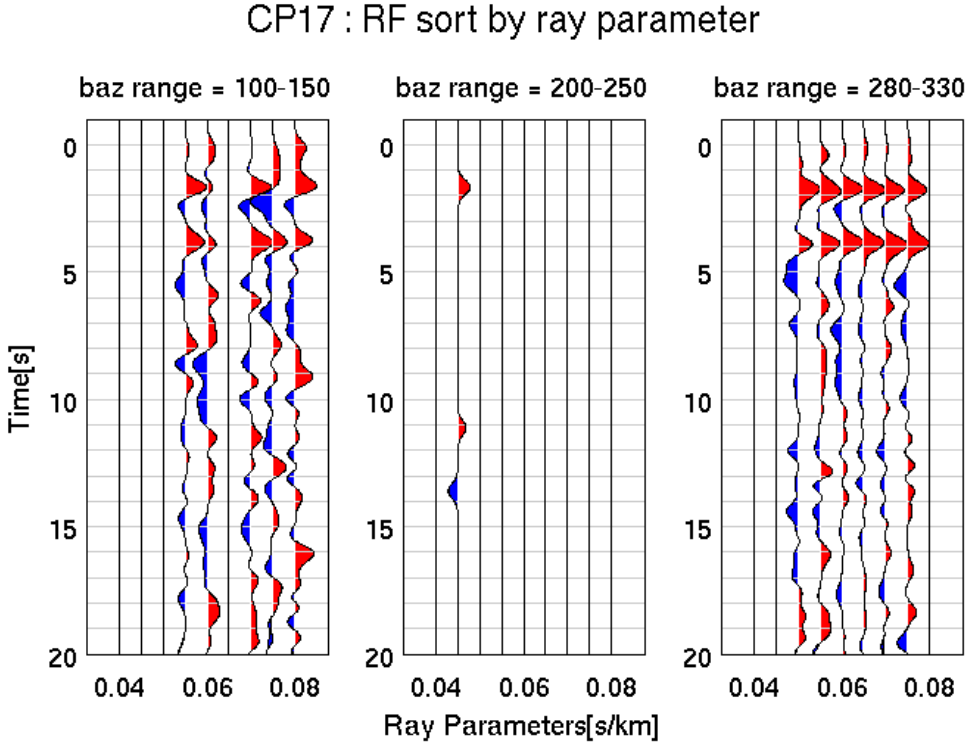
CP17 : RF sort by ray parameter
baz range = 100-150
baz range = 200-250
baz range = 280-330
Time[s]
0
5
10
15
20
0.04
0.06
0.08
Ray Parameters[s/km]

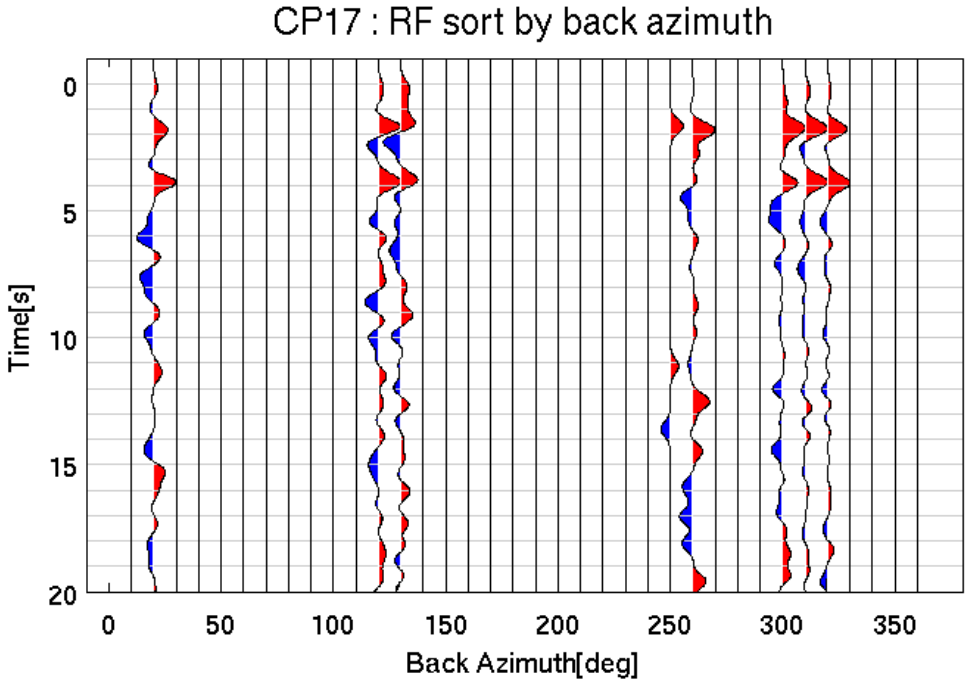
CP17 : RF sort by back azimuth
Time[s]
0
5
10
15
20
0
50
100
150
200
250
300
350
Back Azimuth[deg]

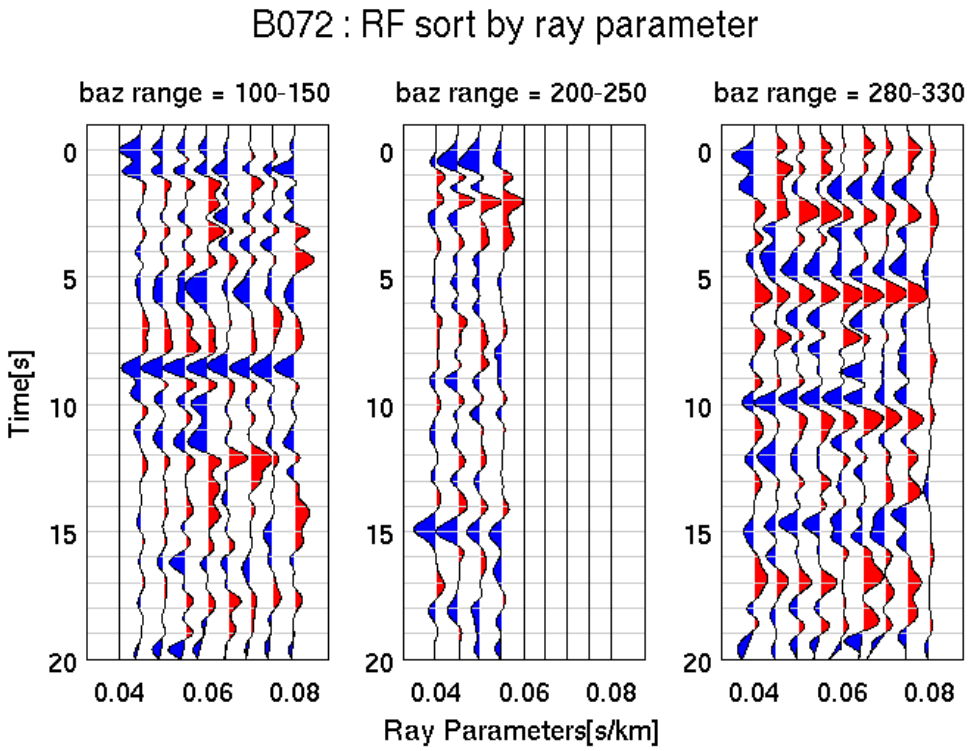
B072 : RF sort by ray parameter
baz range = 100-150
baz range = 200-250
baz range = 280-330
Time[s]
0
5
10
15
20
0.04
0.06
0.08
Ray Parameters[s/km]

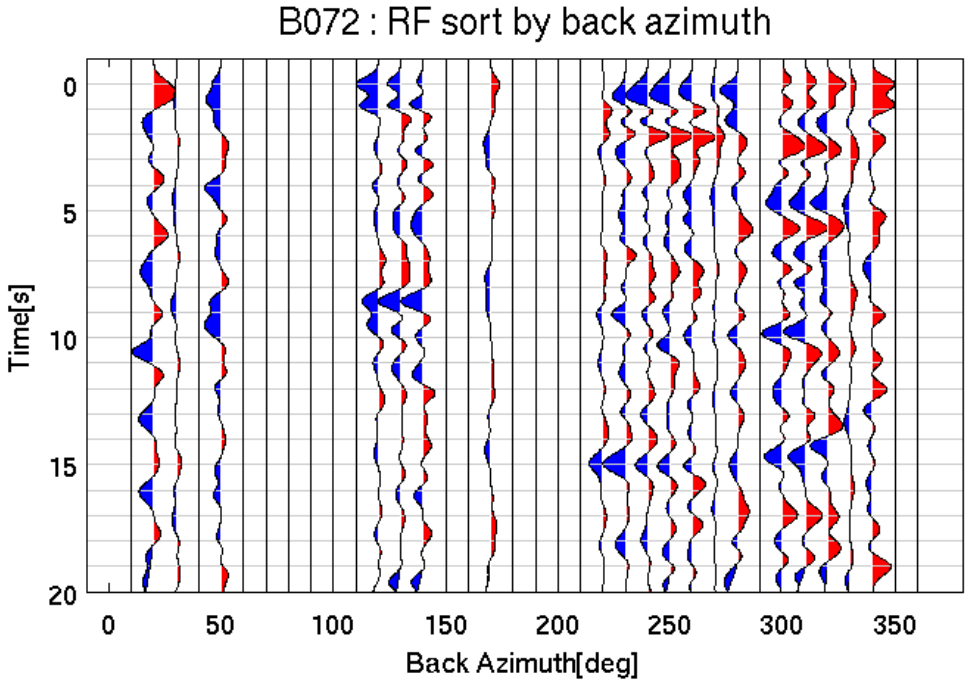
B072 : RF sort by back azimuth
Time[s]
0
5
10
15
20
0
50
100
150
200
250
300
350
Back Azimuth[deg]

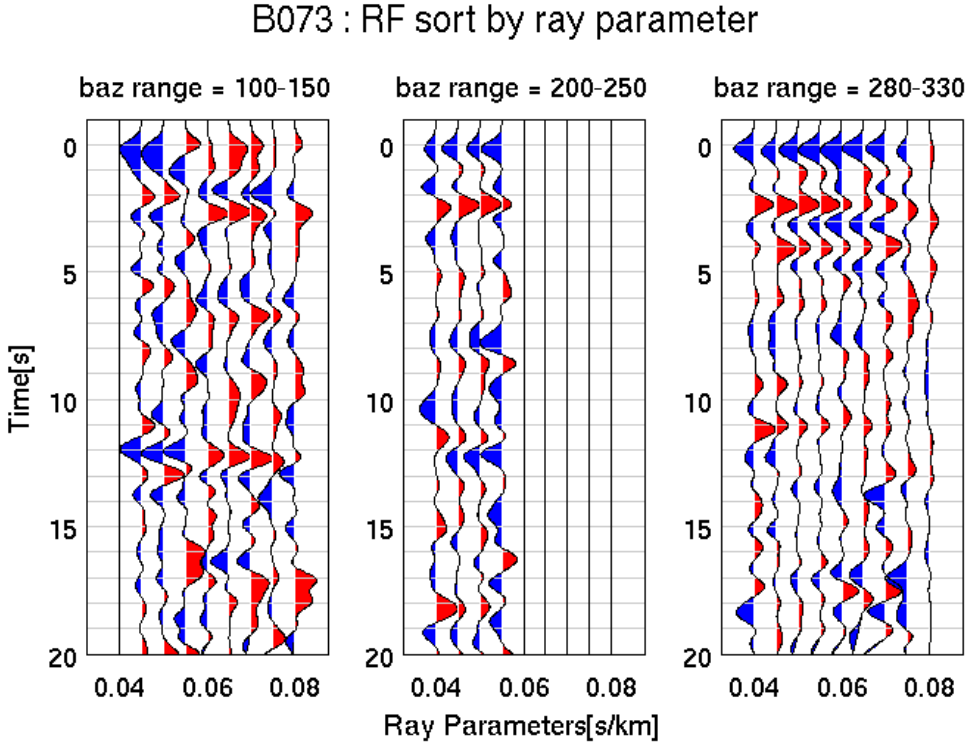
B073 : RF sort by ray parameter
baz range = 100-150
baz range = 200-250
baz range = 280-330
Time[s]
0
5
10
15
20
0.04
0.06
0.08
Ray Parameters[s/km]

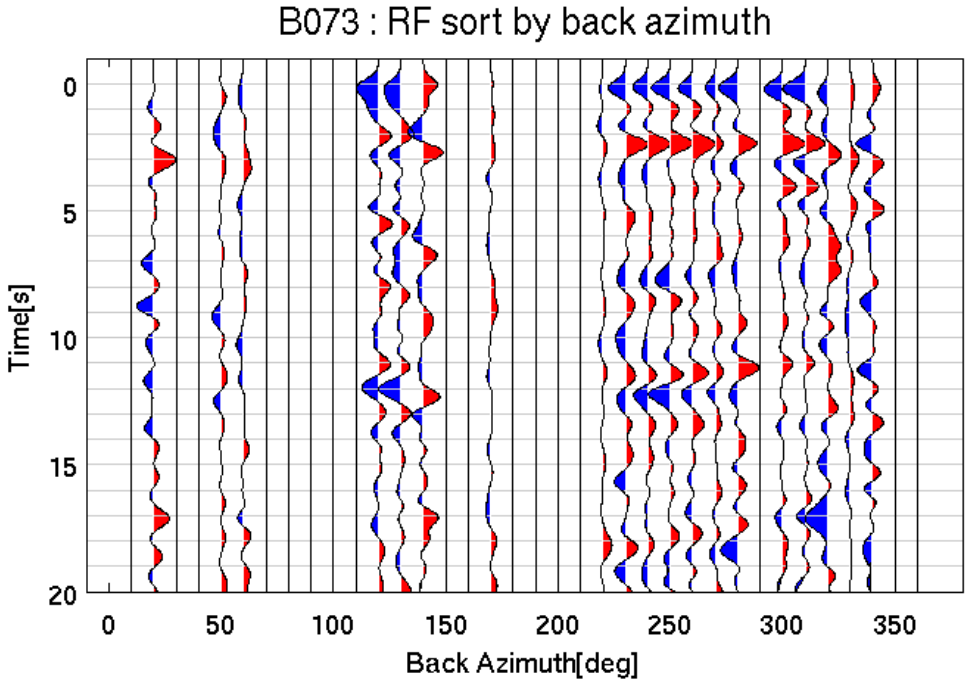
B073 : RF sort by back azimuth
Time[s]
0
5
10
15
20
0
50
100
150
200
250
300
350
Back Azimuth[deg]

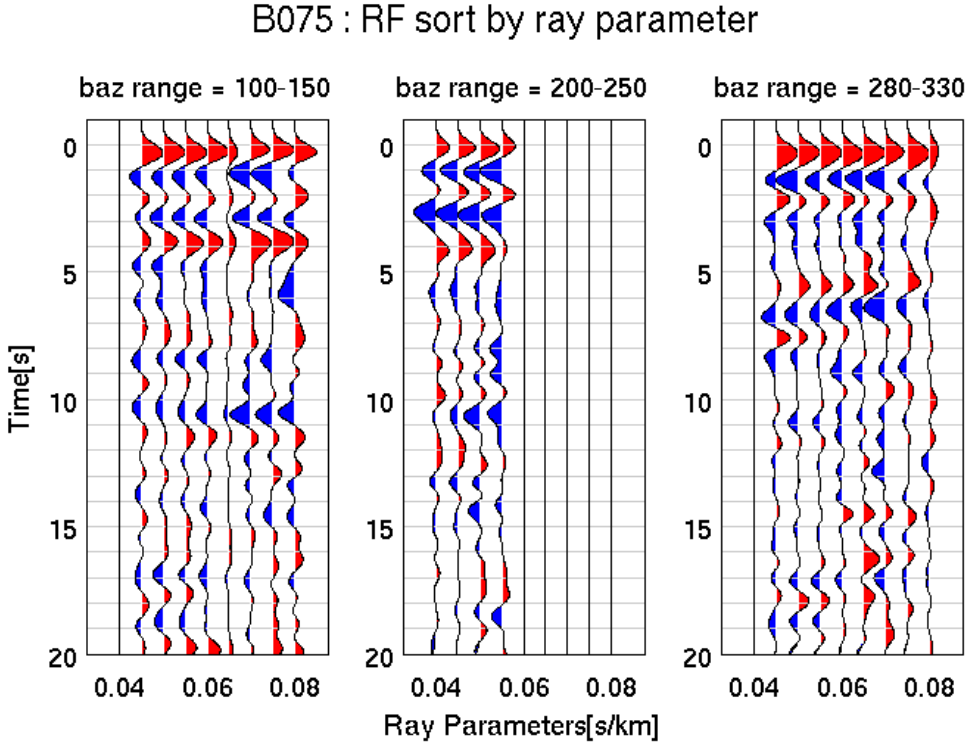
B075 : RF sort by ray parameter
baz range = 100-150
baz range = 200-250
baz range = 280-330
Time[s]
0
5
10
15
20
0.04
0.06
0.08
Ray Parameters[s/km]

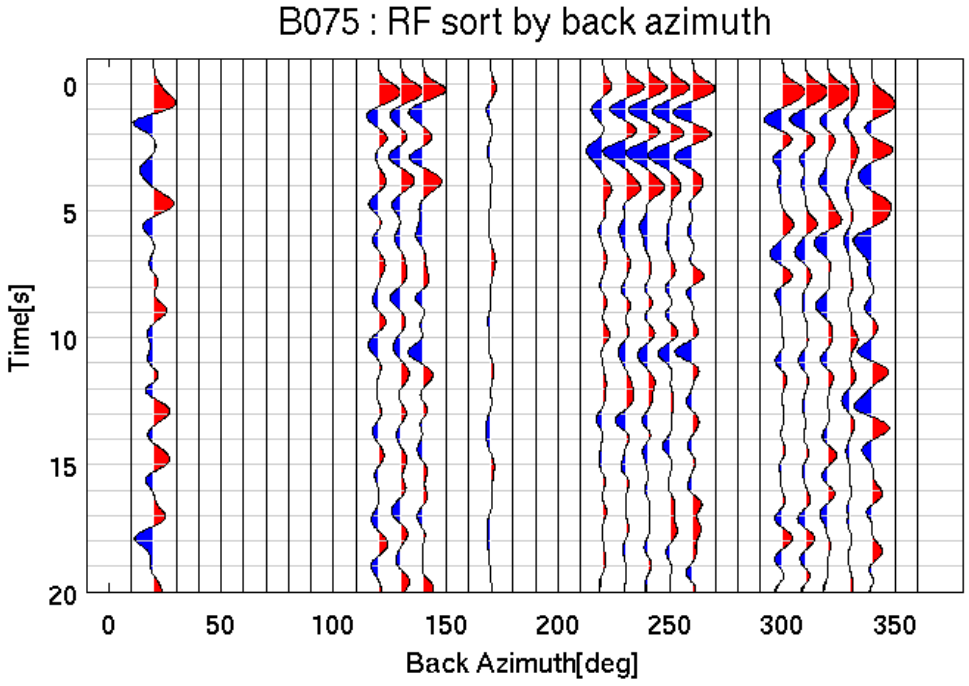
B075 : RF sort by back azimuth
Time[s]
0
5
10
15
20
0
50
100
150
200
250
300
350
Back Azimuth[deg]

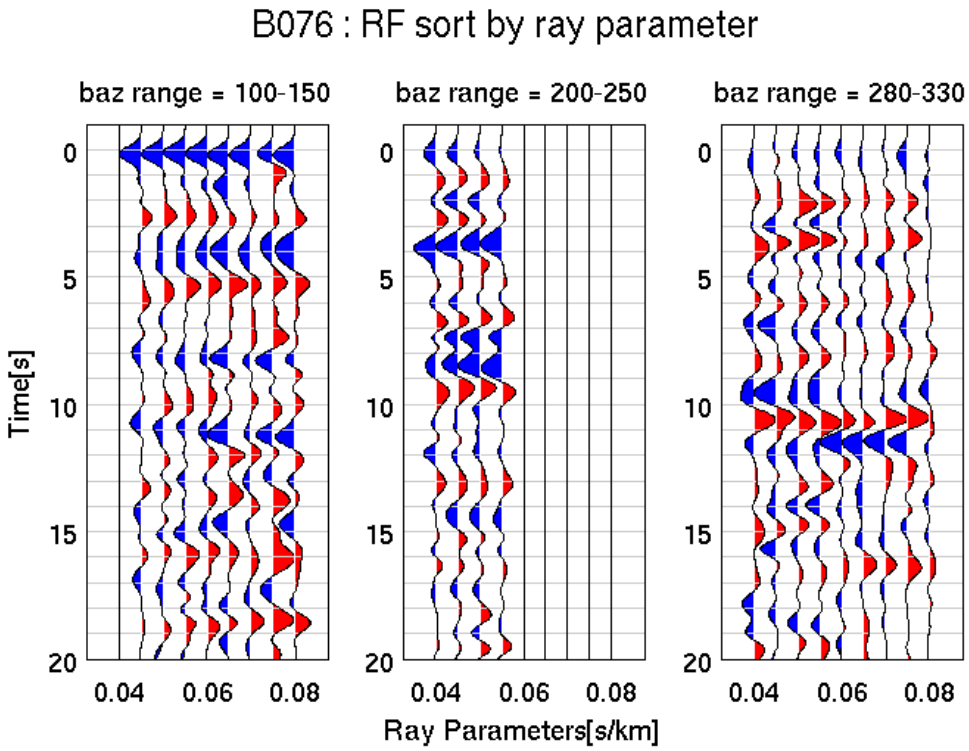
B076 : RF sort by ray parameter
baz range = 100-150
baz range = 200-250
baz range = 280-330
Time[s]
0
5
10
15
20
0.04
0.06
0.08
Ray Parameters[s/km]

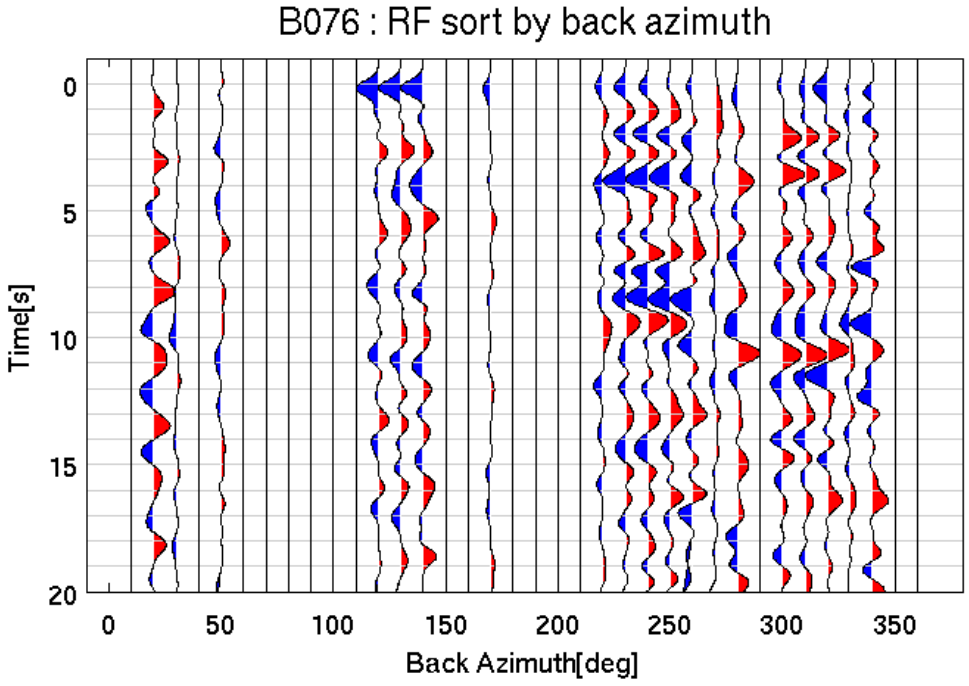
B076 : RF sort by back azimuth
Time[s]
0
5
10
15
20
0
50
100
150
200
250
300
350
Back Azimuth[deg]

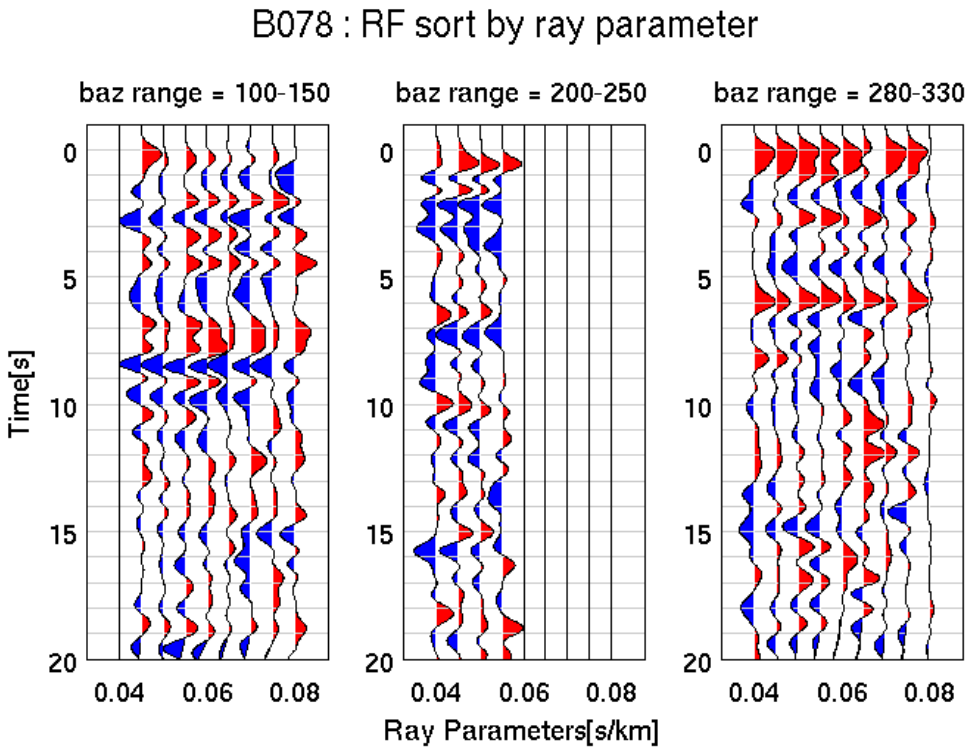
B078 : RF sort by ray parameter
baz range = 100-150
baz range = 200-250
baz range = 280-330
Time[s]
0
5
10
15
20
0.04
0.06
0.08
Ray Parameters[s/km]

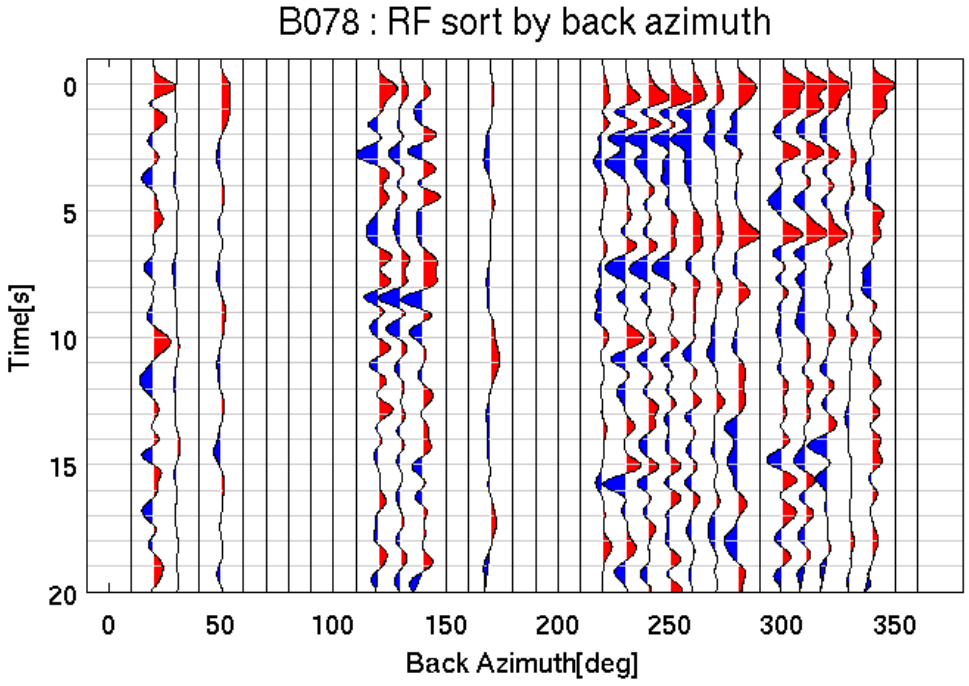
B078 : RF sort by back azimuth
Time[s]
0
5
10
15
20
0
50
100
150
200
250
300
350
Back Azimuth[deg]

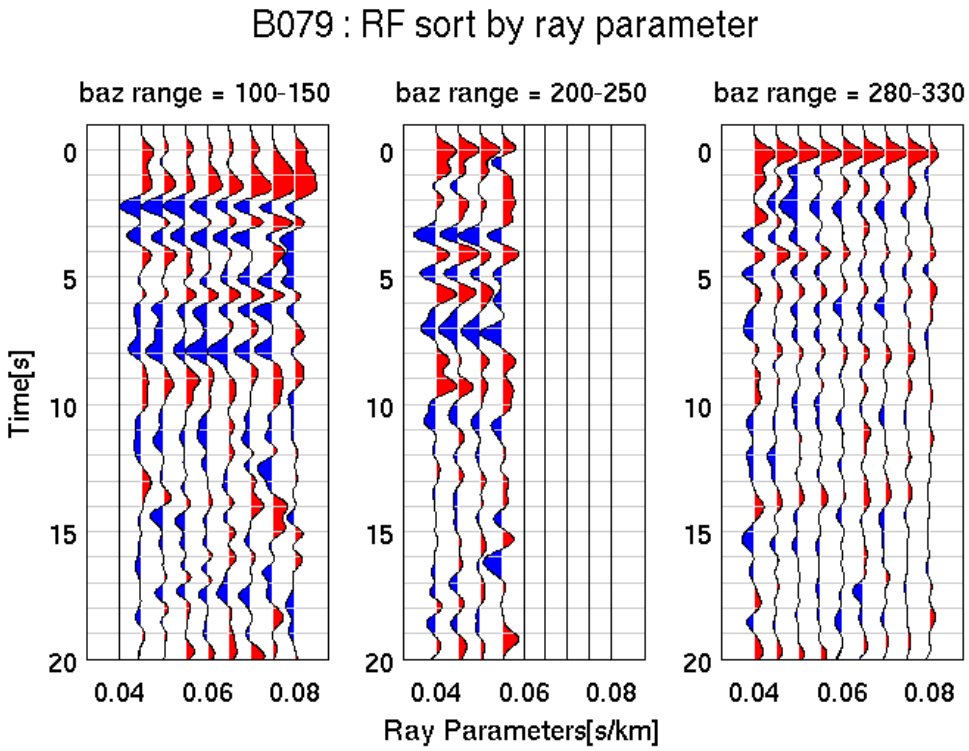
B079 : RF sort by ray parameter
baz range = 100-150
baz range = 200-250
baz range = 280-330
Time[s]
0
5
10
15
20
0.04
0.06
0.08
Ray Parameters[s/km]

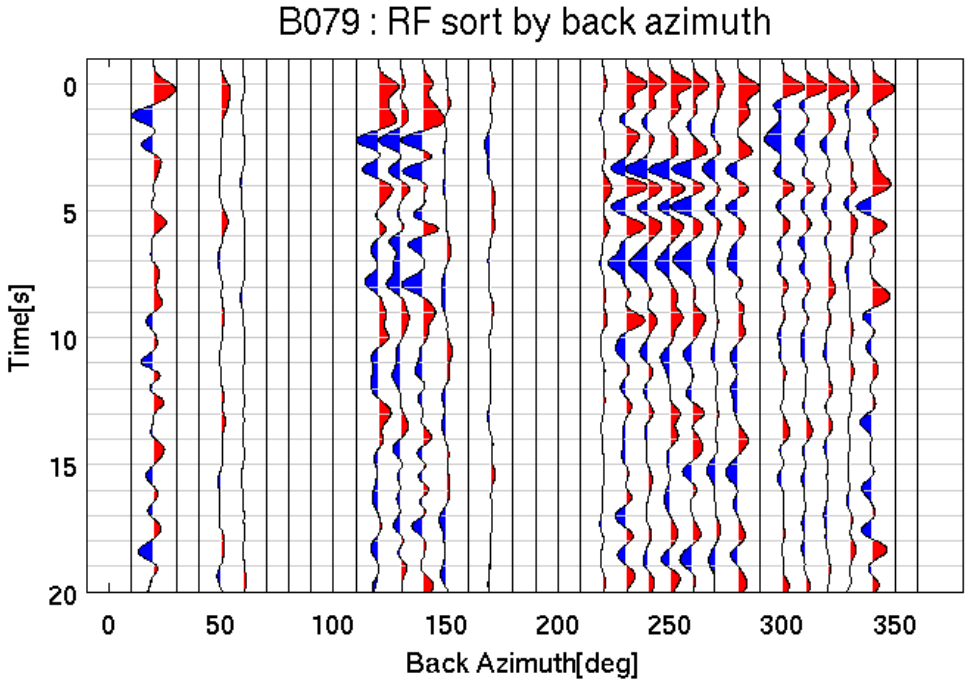
B079 : RF sort by back azimuth
Time[s]
0
5
10
15
20
0
50
100
150
200
250
300
350
Back Azimuth[deg]

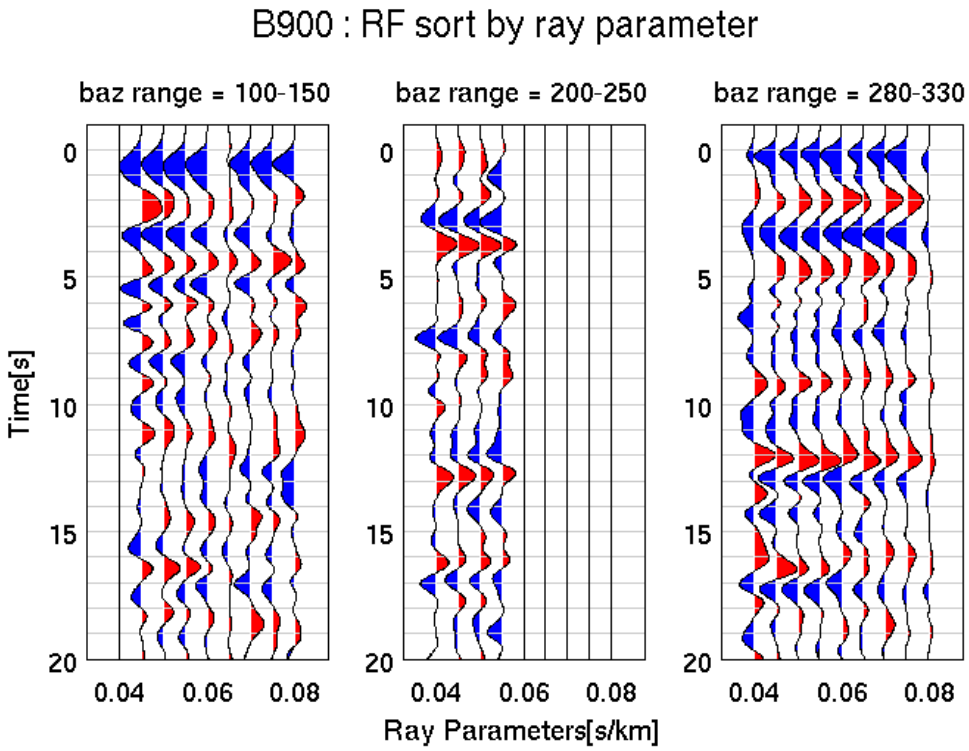
B900 : RF sort by ray parameter
baz range = 100-150
baz range = 200-250
baz range = 280-330
Time[s]
0
5
10
15
20
0.04
0.06
0.08
Ray Parameters[s/km]

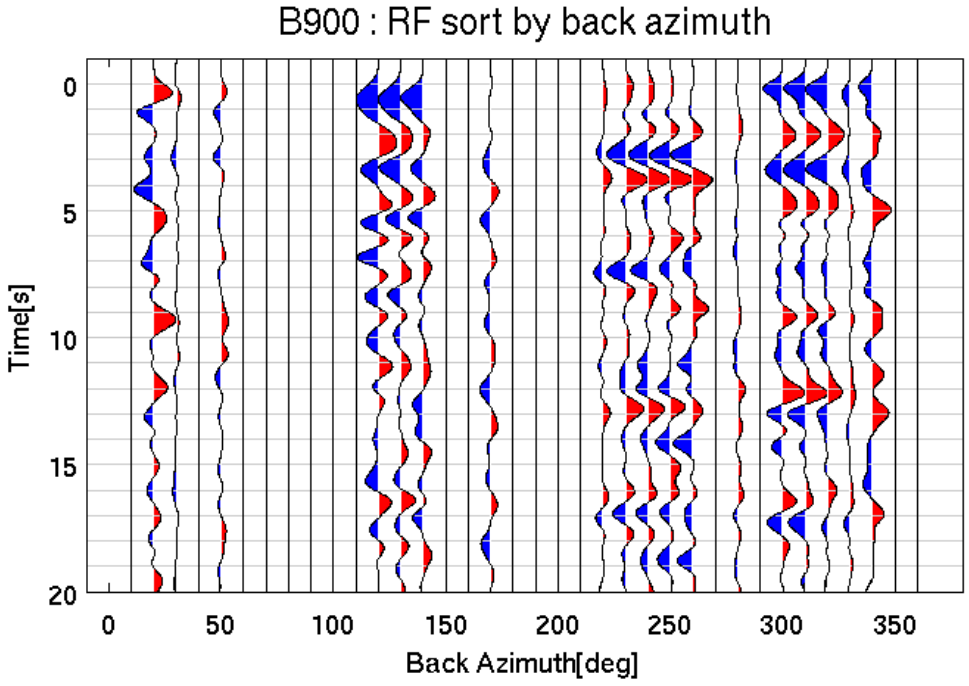
B900 : RF sort by back azimuth
Time[s]
0
5
10
15
20
0
50
100
150
200
250
300
350
Back Azimuth[deg]

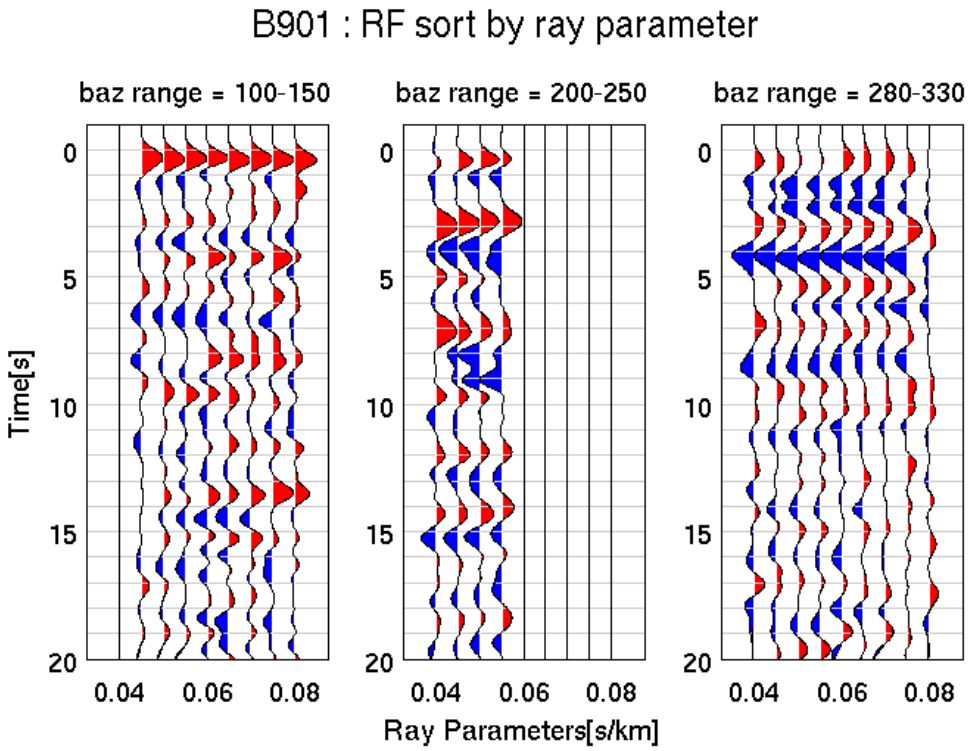
B901 : RF sort by ray parameter
baz range = 100-150
baz range = 200-250
baz range = 280-330
Time[s]
0
5
10
15
20
0.04
0.06
0.08
Ray Parameters[s/km]

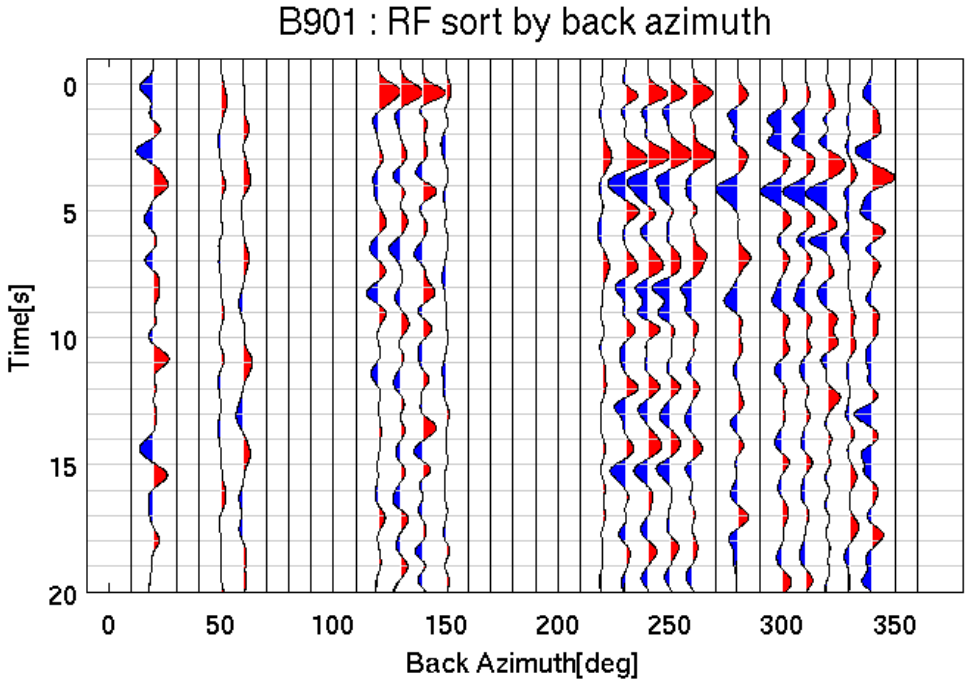
B901 : RF sort by back azimuth
Time[s]
0
5
10
15
20
0
50
100
150
200
250
300
350
Back Azimuth[deg]

References

Abt, D. L., Fischer, K. M., French, S. W., Ford, H. A., Yuan, H., & Romanowicz, B. (2010). North American lithospheric discontinuity structure imaged by Ps and Sp receiver functions. Journal of Geophysical Research, 115(B09301), B09301.

Aki, K. (1982). Three-dimensional seismic inhomogeneities in the lithosphere and asthenosphere: Evidence for decoupling in the lithosphere and flow in the asthenosphere. Reviews of Geophysics, 20(2), 161-170.

Ammon, C. J. (1991). The isolation of receiver effects from teleseismic P waveforms. *Bulletin of the Seismological Society of America*, *81*(6), 2504-2510.

Atwater, T. (1970). Implications of plate tectonics for the Cenozoic tectonic evolution of western North America. *Geological Society of America Bulletin*, *81*(12), 3513-3536.

Atwater, T., & Molnar, P. (1973). Relative motion of the Pacific and North American plates deduced from sea-floor spreading in the Atlantic, Indian, and South Pacific Oceans. Stanford Univ. Publications in Geological Sciences, 13, 136-148.

Beard, J. S., & Day, H. W. (1987). The Smartville intrusive complex, Sierra Nevada, California: The core of a rifted volcanic arc. Geological Society of America Bulletin, 99(6), 779-791.

Biasi, G. P., & Humphreys, E. D. (1992). P - wave image of the upper mantle structure of central California and southern Nevada. Geophysical Research Letters, 19(11), 1161-1164.

Boyd, O. S., Jones, C. H., & Sheehan, A. F. (2004). Foundering lithosphere imaged beneath the southern Sierra Nevada, California, USA. Science, 305(5684), 660-662.

Brocher, T. M., Brink, U. S. T., & Abramovitz, T. (1999). Synthesis of crustal seismic structure and implications for the concept of a slab gap beneath coastal California. International Geology Review, 41(3), 263-274.

Buland, R., & Chapman, C. H. (1983). The computation of seismic travel times. Bulletin of the Seismological Society of America, 73(5), 1271-1302.

Burdick, L. J., & Langston, C. A. (1977). Modeling crustal structure through the use of converted phases in teleseismic body-wave forms. Bulletin of the Seismological Society of America, 67(3), 677-691.

Clayton, R. W., & Wiggins, R. A. (1976). Source shape estimation and deconvolution of teleseismic bodywaves. Geophysical Journal of the Royal Astronomical Society, 47(1), 151-177.

Crawford, F. D., 1971, Petroleum potential of Santa Maria province, California,in Cram, I. H., ed., Future petroleum provinces of the United States—Their geology and potential: Tulsa, American Association of Petroleum Geologists, p. 316–328.

Dickinson, W. R. (1970). Relations of andesites, granites, and derivative sandstones to arc - Trench tectonics. Reviews of Geophysics, 8(4), 813-860.

Dickinson, W. R. (1997). OVERVIEW: Tectonic implications of Cenozoic volcanism in coastal California. Geological Society of America Bulletin, 109(8), 936-954.

Dickinson, W. R. (2008). Accretionary Mesozoic–Cenozoic expansion of the Cordilleran continental margin in California and adjacent Oregon. Geosphere, 4(2), 329-353.

Dickinson, W. R., & Snyder, W. S. (1979). Geometry of subducted slabs related to San Andreas transform. The Journal of Geology, 609-627.

Dickinson, W. R., Hopson, C. A., Saleeby, J. B., Schweickert, R. A., Ingersoll, R. V., Pessagno Jr, E. A., ... & Blome, C. D. (1996). Alternate origins of the Coast Range ophiolite (California): Introduction and implications. GSA Today, 6(2), 1-10.

Ducea, M., & Saleeby, J. (1998). A case for delamination of the deep batholithic crust beneath the Sierra Nevada, California. International Geology Review, 40(1), 78-93.

Earle, P. S., & Shearer, P. M. (1994). Characterization of global seismograms using an automatic-picking algorithm. Bulletin of the Seismological Society of America, 84(2), 366-376.

Ernst, W. G., Seki, Y., Onuki, H., & Gilbert, M. C. (1970). *Comparative study of low-grade metamorphism in the California Coast Ranges and the outer metamorphic belt of Japan*. Geological Society of America., 124, 276.

Frassetto, A. M., Zandt, G., Gilbert, H., Owens, T. J., & Jones, C. H. (2011). Structure of the Sierra Nevada from receiver functions and implications for lithospheric foundering. Geosphere, 7(4), 898-921.

Godfrey, N. J., Beaudoin, B. C., & Klemperer, S. L. (1997). Ophiolitic basement to the Great Valley forearc basin, California, from seismic and gravity data: Implications for crustal growth at the North American continental margin. Geological Society of America Bulletin, 109(12), 1536-1562.

Griscom, A., & Jachens, R. C. (1990). Tectonic implications of gravity and magnetic models along east-west seismic profiles across the Great Valley near Coalinga. *The Coalinga, California, Earthquake of May*, *2*(1983). J. Rymer, W. L. Ellsworth, U.S. Geological Survey Professional Paper, 1487, 69–78.

Gurrola, H., Baker, G. E., & Minster, J. B. (1995). Simultaneous time-domain deconvolution with application to the computation of receiver functions. Geophysical Journal International, 120(3), 537-543.

Gurrola, H., Minster, J. B., & Owens, T. (1994). The use of velocity spectrum for stacking receiver functions and imaging upper mantle discontinuities. Geophysical Journal International, 117(2), 427-440.

Helffrich, G., & Thompson, D. (2010). A stacking approach to estimate VP/VS from receiver functions. Geophysical Journal International, 182(2), 899-902.

Huber, N. K. (1981). Amount and timing of late Cenozoic uplift and tilt of the central Sierra Nevada, California--Evidence from the upper San Joaquin River basin., U.S. Geological Survey Professional Paper 1197, 28p.

Ingersoll, R. V. (1982). Initiation and evolution of the Great Valley forearc basin of northern and central California, USA. *Geological Society, London, Special Publications*, *10*(1), 459-467.

Isaacs, Caroline M. (1992). Petroleum geology of the Santa Maria Basin Assessment Province, California for the 1987 national assessment of undiscovered oil and gas resources. Menlo Park, *Calif*., Denver, Colo., U.S. Dept. of the Interior, U.S. Geological Survey, Open-File Reports 89, 86.

Jones, C. H., Kanamori, H., & Roecker, S. W. (1994). Missing roots and mantle "drips": Regional Pn and teleseismic arrival times in the southern Sierra Nevada and vicinity, California. Journal of Geophysical Research, 99(B3), 4567-4601.

Kikuchi, M., & Kanamori, H. (1982). Inversion of complex body waves. Bulletin of the Seismological Society of America, 72(2), 491-506.

Kind, R., Kosarev, G. L., & Petersen, N. V. (1995). Receiver functions at the stations of the German Regional Seismic Network (GRSN). Geophysical Journal International, 121(1), 191-202.

Langston, C. A. (1977), Effect of planar dipping structure on source and receiver responses for constant ray parameter, Bulletin of the Seismological Society of America, 67 (4), 1029–1050.

Langston, C. A. (1979), Structure under Mount Rainier, Washington, inferred from teleseismic body waves, Journal of Geophysical Research, 84 (NB9), 4749–4762.

Ligorría, J. P., & Ammon, C. J. (1999). Iterative deconvolution and receiver-function estimation. Bulletin of the Seismological Society of America, 89(5), 1395-1400.

Lockwood, J. P., & Moore, J. G. (1979). Regional deformation of the Sierra Nevada, California, on conjugate microfault sets. Journal of Geophysical Research: Solid Earth (1978–2012), 84(B11), 6041-6049.

Lonsdale, P. (1991). Structural patterns of the Pacific floor offshore of peninsular California. *The gulf and peninsular province of the Californias*, AAPG Memori *47*, 87-125.

MacKenzie, L. S., Abers, G. A., Rondenay, S., & Fischer, K. M. (2010). Imaging a steeply dipping subducting slab in Southern Central America. Earth and Planetary Science Letters, 296(3), 459-468.

Miller, K. C., Howie, J. M., & Ruppert, S. D. (1992). Shortening within underplated oceanic crust beneath the central California margin. Journal of Geophysical Research: Solid Earth (1978–2012), 97(B13), 19961-19980.

Nicholson, C., Sorlien, C. C., Atwater, T., Crowell, J. C., & Luyendyk, B. P. (1994). Microplate capture, rotation of the western Transverse Ranges, and initiation of the San Andreas transform as a low-angle fault system. Geology, 22(6), 491-495.

Obrebski, M., Allen, R. M., Pollitz, F., & Hung, S. H. (2011). Lithosphere-asthenosphere interaction beneath the western United States from the joint inversion of body‐wave traveltimes and surface‐wave phase velocities. Geophysical Journal International, 185(2), 1003-1021.

Ozacar, A. A., & Zandt, G. (2009). Crustal structure and seismic anisotropy near the San Andreas Fault at Parkfield, California. Geophysical Journal International, 178(2), 1098-1104.

Page, B. M. (1981). The southern Coast Ranges, The Geotectonic Development of California. Englewood Cliffs, New Jersey, Prentice-Hall, p. 329-417.

Park, J., & Levin, V. (2000). Receiver functions from multiple-taper spectral correlation estimates. Bulletin of the Seismological Society of America, 90(6), 1507-1520.

Pérez-Campos, X., Kim, Y., Husker, A., Davis, P. M., Clayton, R. W., Iglesias, A., ... & Gurnis, M. (2008). Horizontal subduction and truncation of the Cocos Plate beneath central Mexico. Geophysical Research Letters, 35(18), L18303.

Phinney, R. A. (1964), Structure of earths crust from spectral behavior of longperiod body waves, Journal of Geophysical Research, 69 (14), 2997.3017.

Pikser, J. E., Forsyth, D. W., & Hirth, G. (2012). Along-strike translation of a fossil slab. Earth and Planetary Science Letters, 331, 315-321.

Raikes, S. A. (1976). The azimuthal variation of teleseismic P-wave residuals for stations in southern California. Earth and Planetary Science Letters, 29(2), 367-372.

Romanowicz, B. A. (1980). Large scale three dimensional P velocity structure beneath the western US and the lost Farallon plate. Geophysical Research Letters, 7(5), 345-348.

Rychert, C. A., & Shearer, P. M. (2009). A global view of the lithosphere-asthenosphere boundary. Science, 324(5926), 495-498.

Schmandt, B., & Humphreys, E. (2010). Seismic heterogeneity and small -

scale convection in the southern California upper mantle. Geochemistry, Geophysics, Geosystems, 11(5).

Schulte‐Pelkum, V., & Ben‐Zion, Y. (2012). Apparent Vertical Moho Offsets under Continental Strike‐Slip Faults from Lithology Contrasts in the Seismogenic Crust. Bulletin of the Seismological Society of America, 102(6), 2757-2763.

Schweickert, R. A., & Cowan, D. S. (1975). Early Mesozoic tectonic evolution of the western Sierra Nevada, California. Geological Society of America Bulletin, 86(10), 1329-1336.

ten Brink, U. S., Shimizu, N., & Molzer, P. C. (1999). Plate deformation at depth under northern California: Slab gap or stretched slab?. Tectonics, 18(6), 1084-1098.

Thomson, D. J. (1982). Spectrum estimation and harmonic analysis. Proceedings of the IEEE, 70(9), 1055-1096.

Trehu, A. M., & Wheeler, W. H. (1987). Possible evidence for subducted sedimentary materials beneath central California. Geology, 15(3), 254-258.

Walter, A. W. (1990). Upper-crustal velocity structure near Coalinga, as determined from seismic-refraction data. United States Geological Survey, Professional Paper;(USA), 1487.

Wang, Y., Forsyth, D. W., Rau, C. J., Carriero, N., Schmandt, B., Gaherty, J. B., & Savage, B. (2013). Fossil slabs attached to unsubducted fragments of the Farallon plate. Proceedings of the National Academy of Sciences, 110(14), 5342-5346.

Wentworth, C. M., & Zoback, M. D. (1990). Structure of the Coalinga area and thrust origin of the earthquake. The Coalinga, California, Earthquake of May, 2(1983), 41-68.

Yan, Z., & Clayton, R. W. (2007a). A notch structure on the Moho beneath the Eastern San Gabriel Mountains. Earth and Planetary Science Letters, 260(3), 570-581.

Yan, Z., & Clayton, R. W. (2007b). Regional mapping of the crustal structure in southern California from receiver functions. Journal of Geophysical Research, 112(B5), B05311.

Yang, Y., & Forsyth, D. W. (2006). Rayleigh wave phase velocities, small - scale convection, and azimuthal anisotropy beneath southern California. Journal of Geophysical Research: Solid Earth (1978-2012), 111(B7).

Zandt, G. (2003). The southern Sierra Nevada drip and the mantle wind direction beneath the southwestern United States. International Geology Review, 45(3), 213-224.

Zandt, G., & Ammon, C. J. (1995). Continental crust composition constrained by measurements of crustal Poisson's ratio. Nature, 374(6518), 152-154.

Zandt, G., Gilbert, H., Owens, T. J., Ducea, M., Saleeby, J., & Jones, C. H. (2004). Active foundering of a continental arc root beneath the southern Sierra Nevada in California. Nature, 431(7004), 41-46.

Zheng, T., Chen, L., Zhao, L., Xu, W., & Zhu, R. (2006). Crust–mantle structure difference across the gravity gradient zone in North China Craton: seismic image of the thinned continental crust. Physics of the Earth and Planetary Interiors, 159(1), 43-58.

Zhu, L. P., and H. Kanamori (2000), Moho depth variation in southern California from teleseismic receiver functions, Journal of Geophysical Research-Solid Earth, 105 (B2), 2969–2980.

Zuleta Tobon, L. M. (2012). Near-surface characterization and Vp/Vs analysis of a shale gas basin. Master's Thesis, University of Calgary, Canada.